# Quantitative biophysical methods to study immune cell mechanobiology




**Liliana Barbieri**

University of Oxford

This dissertation is submitted for the degree of

*Doctor of Philosophy*

University College

April 2021

"Ciascuno cresce solo se sognato", Danilo Dolci.

To Patrizia Tumbiolo and Luigi Barbieri.

# Declaration

I hereby declare that except where specific reference is made to the work of others, the contents of this dissertation are original and have not been submitted in whole or in part for consideration for any other degree or qualification in this, or any other university. This dissertation is my own work and contains nothing which is the outcome of work done in collaboration with others, except as specified in the text and in the following:

- Rat Basophilic Leukaemia cells expressing Lifeact-citrine were produced by Dr. James Felce.
- E6.1-57 Jurkat T cells stably expressing the 1G4-TCR and the corresponding pMHC molecules were produced by Dr. Veronica Chang and Dr. Huw Colin-York.
- HeLa cells stably expressing Lifeact-citrine were produced by Prof. Marco Fritzsche.
- The 2D TIRF-SIM set-up was built by Dr. Kseniya Korobchevskaya.
- The 3D SIM-TFM experiments were carried in collaboration with Dr. Huw Colin-York.
- The 3D SIM-TFM data analysis was carried by Dr. Huw Colin-York.
- The aTFM set-up was built by Dr. Di Li.
- The aTFM experiments were carried in collaboration with Dr. Huw Colin-York and Dr. Di Li.

- The aTFM data analysis and simulations were carried by Dr. Huw Colin-York and Dr. Yousef Javanmardi.
- The spreading data were analysed in cooperation with Gabrielle Chappell, MSc student from the lab of Prof. Marco Fritzsche that I supervised, and Dr. Narain Karedla.
- The primary Human T-cells were given by Dr. Isabela Pedroza-Pacheco.
- The Graphical User Interface for the CalQTrace software was developed by Dr. Aurelien Barbotin.
- The large Field of View light-sheet microscope was designed and built by Dr. Kseniya Korobchevskaya, Dr. Azeem Ahmad and Veronika Pfannenstill.
- The PDMS chamber was designed and realised in collaboration with Dr. Kseniya Korobchevskaya, Veronika Pfannenstill and John Prentice at the Department of Oncology Workshop (Oxford, UK).

Liliana Barbieri

April 2021

# Acknowledgements

A PhD thesis is the culmination of years of work aimed to improve our understanding of Life and our society, as well as a journey of personal growth.

For that, all my gratitude goes to my main supervisor Prof. Marco Fritzsche, for giving me the opportunity to contribute towards an international, collaborative, and highly impactful research. I would like to thank him for being my mentor and for always believing in me with the same intensity, from the first day I timidly approached him until today. Finally, I want to thank Marco for his restless passion towards science, for always pushing me to think bigger, and for the amazing travelling opportunities, including conferences, advanced courses, and research collaborations, before the Covid-19 pandemic happen.

I would also like to thank my co-supervisor Dr. Huw Colin-York, because none of the achievements in this thesis would have been possible without him. I am extremely grateful for everything he taught me all these years, for his kindness and for his unwavering patience, no matter how many times I asked the same questions. Thank you for being a model of inspiration to me.

My thanks also go to my co-supervisor Prof. Christian Eggeling, for giving me the invaluable opportunity to be here in Oxford. I would also like to acknowledge all the people involved in this work. Many thanks to Kseniya, for her knowledge and support at the SIM microscope, and for always being available day and night to receive my calls. To Veronika, for all her hard work at the light-sheet microscope and good coffee break

companion. To Gabrielle, Glikerya and Lena, for giving me the opportunity to be a mentor, confirming my love for it. Many thanks to Michael Dustin, Dong Li, Balpreet S. Ahluwalia, Emad Moeendarbary, Teng-Leong Chew, and their respective group members. To Isabela Pedroza-Pacheco for training me with the primary human cells, for all the cell supplies and her immunology knowledge. Many thanks to all the Eggeling group, for not just being a group of colleagues, but also wonderful friends. In particular my thanks and appreciation go to Dominc, for all his precious mentoring about image analysis, machine learning, and life. To Iztok and Iztok's car, for all his prompt help in the lab and outside. To Dilip with his infinite knowledge of Chemistry and Biology and his explosive energy that made me smile every day. To Silvia and Francesco, for their microscopy support and for bringing a bit of Italy in the lab. A warm thanks to Erdinc, for being a model of inspiration in the lab and for his extremely hard training at Age of Empires when a break from science was needed. To Chris and Pablo, for their prompt support at the imaging facility, and for the wonderful adventure at the Janelia Research Campus, where experiments performed at crazy hours were accompanied by tennis table matches and some friendly drinks. I am thankful for the inputs and feedbacks from my thesis committee members and transfer and confirmation of status examiners: Omer Dushek, Veronica Buckle, Michael Dustin and Ian Dobbie.

A huge thanks goes to Falk, a colleague, a friend, and a brother to me, always ready to help with an answer to any of my infinite questions, and with a good beer whenever the answer could not be found. To my dear friend Martyna, a sister always next to my side to support me during my best and worst moments with her good heart and enthusiasm. Thanks to Ivan, Ioanna, Merve, Pablo, for all our beautiful moments together, which we were so lucky to experience. To Aurelien, who made the start of this Oxford life less scary and special, for his friendship, and his invaluable contribution to the CalQTrace software. To all my ONBI DTC 2016 crew, for all the fun and unforgettable moments together. To

my College advisor and mentor Prof. Peter Jezzard goes a profound thanks for selecting me into the ONBI programme, for his support with funding and fellowship, his constant mentoring and for being an example of a successful scientist, director, advisor, and father. To my ex-housemate and friend Francesca and her partner Marco, for being a second family that was always there to support me whenever I was spending long nights performing experiments. I am extremely thankful for all our delicious dinners, concerts, political and philosophical discussions, and most importantly for being considerate with the volume when playing the violine. To Giulio, and his incredible skills in house problem solving, regularly tested during these years. To Federico, Virginia, Gunnar, Luz, Lucrezia and Lucia, a big thank you for all the great moments in Oxford, our nights singing with a guitar and a beer, for all the sushi and pizza, and movie nights. Thanks to Ali for remembering me to alternate lab work with sport and discussions about Schopenhauer and Kant. To Robyn for giving me a safe and calm place where to finish writing my thesis. Matteo and Luca, I will never thank life enough for sending you next to me during all these 4.5 years. Thank you for all the countless adventures and wonderful moments that we experienced together, for sticking with each other throughout hard times, and for enduring my endless group chats. To my Sicilian friends and the Exodos community. In particular to Giuseppe Savagnone, my spiritual mentor who always guided me towards self-awareness with perpetual faith in me. To Cristina, Gabriele, Marika, Aaron, Roberto, Flora, Francesca, Giulia, and Teresa, for their constant support and love during all these years. To Irene and her singing lessons, for helping me by raising my self-confidence and releasing my stress, and for enduring all my voice crashes.

An enormous thanks goes to Narain, for his unstoppable and contagious passion, for the stimulating (although never-ending) scientific discussions, his unwavering support, for his great ideas about image analysis and for the proofreading of this thesis. Finally,

thank you for your unbreakable patience during my worse moments and for your joyful personality.

Lastly, an infinite thanks to my family. To Giovanni and Maria, for bringing peace and happiness in my life, for being proud of me and having faith in me, and for their constant effort in demolishing the barriers created by the long distance. Most importantly to my mother Patrizia and my father Luigi because “ciascuno cresce solo se sognato” (each of us grows only if they are dreamed of), and they always had the ability during all these years to dream the next version of me even before it existed. Thank you for never letting me give up, for your immense love and support, asking only for my happiness in return.

# Abstract

Mechanobiology is increasingly thought to critically underpin health and disease. During their lifetime, cells carry out their function interacting with the external biophysical environment through mechanical and biochemical events. This is the case for T cells of the adaptive immune system during their activation via interactions with Antigen Presenting Cells (APCs). T-cell activation critically depends on the binding of the T-cell receptor (TCR) to the foreign antigen presented by the APC at the immunological synapse, leading to an orchestrated series of events including cytoskeletal rearrangement, the release of calcium from the endoplasmic reticulum and a change in the expression of surface proteins. TCR cluster migration is a consequence of actin cytoskeleton mediated forces in the range of pico-Newton and sub-second time scale. Hence, dissecting the significance of mechanobiology during T-cell activation requires quantitative biophysical methods for force and calcium readouts. However, the existing technologies do not offer the required sensitivity, robust quantification, and high statistical power. In this work, we present three new methods for planar and axial force generation on the nanometre length scale and sub-second time scale, combining Traction Force Microscopy with Structured Illumination Microscopy. Next, we establish a new machine learning based single-cell high-throughput platform, to quantify automatically and simultaneously the calcium responses of $>$ 100,000 cells. Taken together, these techniques represent a powerful quantitative biophysical platform, opening up new directions for interrogating the role of mechanobiology in health and diseases.

# Table of contents

**List of figures** **xvi**

**List of tables** **xviii**

**Acronyms** **xix**

**1 Introduction** **1**

**2 Background** **5**

2.1 The immune system . . . . . 5

2.2 Cytotoxic $CD8^+$ T-cell activation . . . . . 7

2.2.1 T-cell receptor triggering . . . . . 7

2.2.2 T-cell receptor signalling . . . . . 9

2.2.3 Immunological synapse formation . . . . . 10

2.3 Cell cytoskeleton structures and dynamics . . . . . 11

2.3.1 Actin cytoskeleton . . . . . 12

2.4 $Ca^{2+}$ signalling . . . . . 13

2.5 Expansion and effector phases: expression of surface activation markers . 14

2.6 Mechanobiology in T-cell activation . . . . . 15

2.6.1 Mechanical force during T-cell activation . . . . . 16

2.6.2 Mechanical force influences T-cell function . . . . . 17

2.6.3 Mechanoadaptation during T-cell activation . . . . . 18

2.7 Biophysical readouts of T-cell activation . . . . . 19
2.8 Methodologies for T-cell activation readouts . . . . . 20
2.8.1 Methods and techniques for measuring mechanical force on the biophysical environment during T-cell activation . . . . . 20
2.8.2 Methods and techniques for measuring $Ca^{2+}$ signalling during T-cell activation . . . . . 22
2.8.3 Methods and techniques for surface activation markers measurements 24
2.9 Aim of the thesis . . . . . 25

**3 Materials and methods** **27**
3.1 Cell culture . . . . . 27
3.1.1 HeLa cells . . . . . 27
3.1.2 RBL cells . . . . . 28
3.1.3 Primary salmon keratocytes . . . . . 28
3.1.4 1G4 Jurkat T-cells . . . . . 29
3.1.5 Isolation and activation of human $CD8^+$ T-cells . . . . . 29
3.2 Microscopy . . . . . 31
3.2.1 Atomic Force Microscopy . . . . . 31
3.2.2 Spinning disk confocal microscopy . . . . . 31
3.2.3 TIRF-SIM . . . . . 32
3.3 Super-resolution Traction Force Microscopy . . . . . 33
3.3.1 Silicone gel preparation . . . . . 33
3.3.2 Singular value decomposition analysis and best PIV selection . . . 37
3.3.3 Accuracy and precision diagrams . . . . . 38
3.3.4 Migration speed . . . . . 39
3.3.5 aTFM localisation calibration . . . . . 39
3.3.6 Lateral resolution estimation for TIRF-SIM and WF . . . . . 40

3.3.7 Statistics . . . 41
3.4 Automated single-cell high-throughput $Ca^{2+}$ platform . . . 41
3.4.1 CalQTrace software description . . . 41
3.4.2 1D CNN model . . . 44
3.4.3 pMHC protein production . . . 46
3.4.4 Protein biotinylation . . . 46
3.4.5 Coverslip functionalisation . . . 47
3.4.6 $Ca^{2+}$ assay with dead and $CD25^{+}$ cell markers . . . 48
3.4.7 $Ca^{2+}$ and contact area spreading assay . . . 49
3.4.8 $Ca^{2+}$ image pre-processing . . . 49
3.4.9 Development of a cell segmentation plug-in . . . 49
3.4.10 Implementation of cell segmentation into the CalQTrace pipeline . 51
3.4.11 Statistics . . . 51

**4 Establishing a live-cell super-resolution Traction Force Microscopy 55**
4.1 Traction Force Microscopy . . . 56
4.1.1 Reference-free TFM method . . . 57
4.1.2 Reference based TFM method . . . 57
4.2 Theory behind Traction Force Microscopy . . . 58
4.2.1 Fourier Transform Traction Cytometry . . . 58
4.2.2 Regularisation . . . 60
4.2.3 Displacement field extraction: SPT and PIV . . . 61
4.3 Overview of force quantification in cells . . . 62
4.4 TFM sensitivity . . . 63
4.5 2D TIRF-SIM-TFM . . . 66
4.5.1 Improving TFM sensitivity using 2D TIRF-SIM . . . 68
4.5.2 Singular value decomposition analysis . . . 70

4.5.3 Accuracy and precision scoring metrics . . . . . 77
4.5.4 2D TIRF-SIM-TFM: gel optimisation . . . . . 78
4.5.5 2D TIRF-SIM-TFM of adherent HeLa cell . . . . . 81
4.5.6 2D TIRF-SIM-TFM of RBL cell activation . . . . . 87
4.5.7 2D TIRF-SIM-TFM of primary salmon keratocyte cell migration . 90
4.5.8 Summary . . . . . 93
4.6 3D SIM-TFM . . . . . 99
4.6.1 3D SIM-TFM of adherent HeLa cell . . . . . 99
4.6.2 Summary . . . . . 101
4.7 aTFM . . . . . 102
4.7.1 Astigmatic TFM coupled with high resolution TIRF-SIM cellular imaging . . . . . 102
4.7.2 Calibration of aTFM sensitivity and dynamic range . . . . . 107
4.7.3 aTFM of adherent HeLa cell . . . . . 109
4.7.4 aTFM of RBL cell activation . . . . . 110
4.7.5 Summary . . . . . 114

**5 Establishing an automated single-cell high-throughput $Ca^{2+}$ platform 117**
5.1 Machine learning based technology . . . . . 118
5.1.1 Convolutional Neural Network . . . . . 120
5.1.2 Learning rate optimisation . . . . . 122
5.1.3 The overfitting problem . . . . . 123
5.2 Overview of $Ca^{2+}$ and activation markers quantification . . . . . 124
5.3 Need for methodology development . . . . . 125
5.4 Development of CalQTrace software . . . . . 128
5.4.1 Software pipeline . . . . . 128
5.4.2 $Ca^{2+}$ response might predict T-cell activation strength . . . . . 133

5.5 Development of a large-field-of-view light-sheet hardware . . . . . 140
5.6 Summary . . . . . 143

**6 Discussion** **149**

6.1 Summary of the thesis . . . . . 149
6.2 Future work . . . . . 152
6.3 DPhil Publications . . . . . 155

**References** **157**

# List of figures

2.1 Schematic of the immune response and T-cell activation . . . . . 8

3.1 Silicone gel thickness control . . . . . 36
3.2 1D CNN model structure . . . . . 44
3.3 Cell segmentation plug-in pipeline . . . . . 52
3.4 Cell segmentation outcome . . . . . 53

4.1 Schematic of the three novel SIM-TFM methodologies . . . . . 64
4.2 Experimental design of the 2D TIRF-SIM-TFM methodology . . . . . 67
4.3 2D TIRF-SIM-TFM simulation . . . . . 72
4.4 Number of beads per PIV window size . . . . . 73
4.5 SVD analysis and optimal PIV window choice for 82 beads/$\mu m^2$ . . . . . 75
4.6 SVD analysis and optimal PIV window choice for 12 beads/$\mu m^2$ . . . . . 76
4.7 Accuracy and precision of 2D TIRF-SIM-TFM . . . . . 79

4.8 Calibration of the silicone gel stiffness . . . . . 80
4.9 HeLa cell detachment with 2D TIRF-SIM-TFM . . . . . 81
4.10 Beads displacement during HeLa cell detachment with 2D TIRF-SIM . . 83
4.11 Lateral displacement and stress fields during HeLa cell detachment with 2D TIRF-SIM-TFM . . . . . 85
4.12 RBL cell activation with 2D TIRF-SIM-TFM . . . . . 88
4.13 Fast RBL cell activation with 2D TIRF-SIM-TFM . . . . . 89
4.14 Primary salmon keratocyte cell migration with 2D TIRF-SIM-TFM . . . 91
4.15 Lateral displacement of primary salmon keratocyte with 2D TIRF-SIM-TFM and different PIV window sizes . . . . . 94
4.16 Lateral displacement and stress fields of primary salmon keratocyte with 2D TIRF-SIM-TFM . . . . . 95
4.17 Lateral displacement derivative of primary salmon keratocyte with 2D TIRF-SIM-TFM . . . . . 96
4.18 Small-scale changes in lateral displacement of primary salmon keratocyte with 2D TIRF-SIM-TFM . . . . . 97
4.19 High-temporal imaging of primary salmon keratocyte with TIRF-SIM . . 98
4.20 Experimental design of the 3D SIM-TFM methodology . . . . . 100
4.21 3D SIM-TFM resolution and bead density trackability estimation . . . . 102
4.22 HeLa cell early adhesion with 3D SIM-TFM . . . . . 103
4.23 Lateral displacement during early adhesion of HeLa cell with 3D SIM-TFM 103
4.24 Lateral stress during early adhesion of HeLa cell with 3D SIM-TFM . . . 104
4.25 Experimental design of the aTFM methodology . . . . . 106
4.26 Calibration of aTFM . . . . . 108
4.27 HeLa cell early adhesion with aTFM . . . . . 110
4.28 HeLa cell with aTFM: beads localisation . . . . . 111

4.29 HeLa cell: lateral and vertical displacement investigated with aTFM . . . 112
4.30 HeLa cell: lateral and vertical stress fields investigated with aTFM . . . 113
4.31 RBL cell activation on a silicone gel with aTFM . . . . . 115
4.32 RBL cell stress fields with aTFM . . . . . 115

5.1 Schematic representation of a perceptron . . . . . 119
5.2 Representation of a non-linear transformation . . . . . 121
5.3 Example of dataset type analysed with CalQTrace software . . . . . 129
5.4 Schematic of the CalQTrace software . . . . . 130
5.5 CalQTrace software: cell detection and exclusion . . . . . 132
5.6 CalQTrace software: cell tracking and $Ca^{2+}$ signalling trace classification 134
5.7 CalQTrace: prediction accuracy . . . . . 135
5.8 1G4 Jurkat T-cells: $Ca^{2+}$ and spreading assay . . . . . 137
5.9 1G4 Jurkat T-cells: $Ca^{2+}$ and spreading analysis . . . . . 139
5.10 1G4 Jurkat T-cells: spreading speed and stability . . . . . 141
5.11 Large FOV light-sheet microscope . . . . . 144
5.12 Light-sheet microscope validation with HeLa cells and 1G4 Jurkat T-cells 145

# List of tables

3.1 Silicone gel: components ratio and stiffness . . . . . 35
3.2 $k_{off}$ rates of the peptides and antibody used . . . . . 47

4.1 Table summarising TFM methods based on fluorescence marker beads. . 65

# Acronyms

**2D TIRF-SIM-TFM** Two-dimensional TIRF-SIM Traction Force Microscopy. 32, 37, 38, 55, 56, 66, 68, 73, 77, 78, 81, 82, 86–88, 90, 92, 93, 98–102, 105, 110, 116, 149, 150, 153

**3D SIM** Three-dimensional SIM. 33, 99–101, 103, 150

**3D SIM-TFM** Three-dimensional SIM Traction Force Microscopy. 55, 56, 66, 99, 101, 102, 109, 150

**ADAM** Adaptive Moment Estimation. 45, 123

**ADP** Adenosine diphosphate. 12

**AFM** Atomic Force Microscopy. 17, 21, 31, 80

**APC** Antigen Presenting Cell. 6, 7, 9, 10, 12, 14–16, 19, 124, 154

**aTFM** Astigmatic Traction Force Microscopy. 33, 55, 56, 66, 105–107, 110, 116, 150, 151, 153

**ATP** Adenosine triphosphate. 12

**BSA** Bovine Serum Albumins. 136

**CalQTrace** Calculation and Quantification of signalling Traces. 41, 117, 118, 127, 128, 133, 135, 136, 140, 143, 146, 147, 151, 154

**CD3** Cluster of differentiation 3. 7, 9

**CNN** Convolutional Neural Network. 41, 43–45, 117, 120–123, 126, 127, 131, 151

**CSD** Confocal spinning disk. 24, 31, 48, 49, 127, 128, 135, 140

**DNN** Deep Neural Network. 118

**E** Young's Modulus. 18

**ER** Endoplasmic reticulum. 9, 10, 13, 20, 22, 124

**FC** Flow Cytometry. 23–25, 125, 127, 140, 152

**Fc$\epsilon$RI** Fc$\epsilon$ receptor-1. 114

**FE** Finite Element. 101, 110, 114

**FOV** Field-Of-View. 25, 26, 50–52, 64, 84, 87, 117, 118, 125–127, 130, 135, 140, 142, 143, 147, 152, 155

**fps** frames per second. 84, 87, 90, 92, 93, 109, 110, 114, 116, 135, 150

**FRET** Förster resonance energy transfer. 21, 24

**FTTC** Fourier Transform Traction Cytometry. 55, 59, 70

**FWHM** Full Width at Half Maximum. 40, 41, 70

**GT** Ground Truth. 37–39, 69–71, 73, 77, 78

**GUI** Graphical User Interface. 41, 42, 44, 51, 118, 127, 128, 130, 151

**IS** Immunological synapse. 10–13, 16, 17, 26, 124, 127, 133, 146, 152, 153

**ITAM** Immuno-receptor tyrosine-based activation motif. 9

**Lck** Lymphocyte-specific protein tyrosine kinase. 9

**MHC** Major Histocompatibility Complex. 7, 46

**MLE** Maximum Likelihood Estimation. 107

**NA** Numerical Aperture. 21, 31, 33, 66, 107, 142, 154

**OTs** Optical tweezers. 21

**PAA** Polyacrylamide. 18, 22, 29, 56

**PBMC** Peripheral blood mononuclear cell. 29, 30, 44, 46, 131, 151

**PDMS** Polydimethylsiloxane. 18, 22, 56, 118, 142, 143, 147, 152, 154

**PI** Propidium iodide. 31, 42, 48, 128

**PIV** Particle Image Velocimetry. 38, 39, 41, 55, 61, 62, 68–71, 73, 74, 77, 78, 81, 84, 86, 87, 92, 93, 99, 100, 149, 150

**pMHC** Peptide bound Major Histocompatibility Complex. 7, 10, 14, 16, 17, 21, 22, 46, 47, 124, 136, 153

**PSF** Point Spread Function. 39–41, 68, 69, 71, 74, 80, 100, 105–107, 114, 116, 151

**RBL** Rat Basophilic Leukemia. 26, 28, 37, 41, 82, 87, 93, 108, 110, 114, 116, 150, 151, 153

**SIM** Structured Illumination Microscopy. 25, 34, 55, 99, 100, 114, 151

**SLM** Spatial Light Modulator. 32, 99

**SNR** Signal-to-Noise-Ratio. 123

**SPT** Single Particle Tracking. 55, 61, 62, 68, 99–101

**SRL** Spatial Resolution Limit. 74

**STED** Stimulated Emission Depletion. 64, 150

**STED-TFM** STED Traction Force Microscopy. 64, 66

**SVD** Singular Value Decomposition. 37, 38, 71, 73, 74, 77, 78

**TCR** T-cell receptor. 6, 7, 9–14, 16–18, 21, 22, 29, 46, 124, 127, 133, 146, 153, 154

**TFM** Traction Force Microscopy. 22, 25, 28, 29, 35, 37, 38, 41, 55–58, 61, 63–66, 68–71, 73, 74, 78, 80, 82, 84, 87, 90, 93, 99, 101, 105, 107, 114, 149–151, 153, 155

**TIRF** Total Internal Reflection Fluorescence. 14, 32, 33, 56, 64, 66–68, 99, 100, 105, 109, 151

**TIRF-SIM** Total Internal Reflection Fluorescence SIM. 32–34, 36, 37, 39–41, 66, 68–71, 73, 74, 77, 78, 80, 82, 84, 90, 93, 99, 105, 107, 109, 114, 149

**WASp** Wiskott-Aldrich Syndrome protein. 10

**WAVE2** Wiskott-Aldrich syndrome protein family member 2. 10

**WF** Wide Field. 32, 37, 39–41, 69, 70, 73, 74, 77, 84, 90, 100, 101, 105, 107, 109, 114, 150

**WF-TFM** WF Traction Force Microscopy. 37, 38, 82, 86–88, 92, 93, 98, 150

# Chapter 1

# Introduction

Mechanobiology plays a crucial role in the adaptive immune system [1, 2]. During their lifetime, T cells constantly migrate from site to site, changing shape and interacting with the external biophysical environment from single cells to tissues. This interaction is carried through mechanical and biochemical processes which influence the stability of the T-cell activation and the consequent immune response to a virus or cancer. In particular, T-cell activation involves nano-length and sub-second time scales actin-mediated force production, in the regime of pico-Newtons (pN) and sub-second time scale, and dynamic calcium ($Ca^{2+}$) signalling responses. Therefore, sensitive quantitative methods for biophysical (force) and biochemical (signalling) readouts are essential for understanding T-cell activation. Unfortunately, the existing methods do not provide the required spatio-temporal sensitivity for force probing, as well as robust analysis and statistical power for measuring signalling heterogeneity are currently missing.

In this thesis, I aim to answer this demand by developing new quantitative biophysical methodologies for mechanical force production, $Ca^{2+}$ signalling and surface proteins expression readouts. The thesis in divided into this introduction chapter and other 5 chapters.

Chapter 2 provides the background of the biological processes involved in this work and the current technologies available for T-cell activation readouts. Specifically, I give an overview of the immune system, with a detailed focus on cytotoxic T-cell activation, triggering and signalling events. In particular, I present the relevant concepts regarding actin cytoskeleton dynamics, $Ca^{2+}$ signalling and surface activation proteins. Next, I give an overview of mechanobiology during T-cell activation and the forces involved. Lastly, I summarise the current technologies available for measuring cell-mediated force production, $Ca^{2+}$ signalling and surface activation proteins.

In chapter 3, I present the materials and methods used in this work. This includes cell lines and primary cells, microscopy techniques, elastic gel preparation, chemicals and procedures used for sample preparation. Data processing, software development pipeline and simulations are described in details in the materials and methods, as well as in the rest of the thesis.

In chapter 4, I focus on three technologies development for measuring two-dimensional (2D) and three-dimensional (3D) mechanical forces with high spatio-temporal sensitivity. First, I introduce the theory behind Traction Force Microscopy (TFM) and previous attempts to improve its spatio-temporal sensitivity. Next, I propose three new methods to increase the sensitivity of TFM using the super-resolution Structured Illumination Microscopy (SIM), named 2D TIRF-SIM-TFM; 3D SIM-TFM and astigmatic TFM (aTFM). Each of the methods is described in a separate section within the chapter 4. For the 2D TIRF-SIM-TFM, I first validate with computer simulations the improvement in sensitivity compared to standard Wide-Field TFM (WF-TFM) technique, and then I apply the tool to measure mechanical force generation during detachment of HeLa cells, immune activation of Rat Basophilic Leukaemia (RBL) cells and migration of primary salmon keratocytes. In the 3D SIM-TFM section, I present the technique validation during early adhesion of HeLa cells. Lastly, in the aTFM section I present calibration of

the new technique as well as force validation during early adhesion of HeLa cells and immune activation of RBL cells acquired during my visit with Dr. H. Colin-York and Prof. M. Fritzsche at the laboratory of Prof. L. Dong based at the Chinese Academy of Sciences (Beijing, China).

In chapter 5, I focus on the development of a new methodology for $Ca^{2+}$ signalling and surface activation proteins readouts with robust data analysis and high statistics. First, I introduce an overview on machine learning based technology with a specific focus on the theory behind Convolutional Neural Network (CNN) algorithms. Next, I present the current technologies, and their limitations, for measuring $Ca^{2+}$ signalling and surface activation proteins. Thereafter, I propose a new methodology consisting of an automated machine learning based software, named Calculation and Quantification of signalling Traces (CalQTrace), coupled to the well established Spinning Disk microscopy. For the CalQTrace software validation, I show a preliminary experiment of $Ca^{2+}$ responses in pre-activated $CD25^{+}$ and resting $CD25^{-}$ primary human $CD8^{+}$ T-cells, with a higher percentage of single-peak and oscillatory $Ca^{2+}$ responses for the pre-activated and higher percentage of non-triggering responses for resting T-cells. Following observations of different $Ca^{2+}$ signalling responses, I present data of simultaneous $Ca^{2+}$ signalling and immunological synapse formation during 1G4 Jurkat T-cells activation, linking the different $Ca^{2+}$ responses to the T-cell activation strength and stability. Lastly, to increase the statistical power of $Ca^{2+}$ experiments, I present a preliminary version of a 4 mm $\times$ 3.5 mm large Field-of-View (FOV) light-sheet microscope, with the potential to image 100,000 cells simultaneously.

Finally, in chapter 6, I summarise the results of chapter 4 and 5, and I discuss possible future work.

# Chapter 2

# Background

In this chapter, I present a background overview to the relevant biophysical and immunological concepts required for understanding the thesis. First, I will introduce the importance of mechanobiology of the immune response during T-cell activation upon interaction with the external biophysical environment. Next, I will explain the molecular mechanism behind the initiation of T-cell activation and the signalling pathways and cytoskeleton rearrangement that lead to full activation. Finally, I will give an overview of the methodologies available to measure T-cell activation readouts, in particular mechanical force production, calcium ($Ca^{2+}$) signalling and expression of surface proteins.

## 2.1 The immune system

The immune system is a fascinating defence machinery protecting vertebrates from disease caused by pathogens and cancers [3, 4]. It can be divided into two subsets, the innate and adaptive immune response. The innate immune response is the one functioning all the time, with the role of responding immediately to a foreign pathogen in a non specific way, preventing its spreading [3]. On the other hand, the adaptive immune response is the one that adapt against a specific infection, to reinforce the immune reaction. Contrary to the

innate, the adaptive immune response provides highly specialised protection to a specific target. The cells that drive the adaptive immune response are a sub-population of white blood cells, called lymphocytes. Each lymphocyte, during its development, encodes a specific plasma membrane receptor but the overall lymphocyte population contains a large variety of such receptors ranging up to some billions of variants [3]. Each cell displays in their outer membrane molecules (such as proteins or peptides) called antigens. The antigens coming from within the body are called 'self' while the one originated from an external environment are defined as 'non-self'. During an infection, only those lymphocytes that express the receptor recognising the 'non-self' antigen from the infecting pathogen can activate, proliferate and differentiate to reinforce the immune response. Generated in the bone marrow during a process called hematopoiesis, lymphocytes derive from the pluripotent hematopoietic stem cells [4]. They can be divided into sub-lineages, such as T-cells, B-cells and Natural Killer cells. In this work, I will focus on the T cell-mediated response, and in particular on the interaction between T cells and the cells presenting antigens coming from foreign pathogens, known as Antigen Presenting Cell (APC).

The T cells begin their journey from the bone marrow and travel to the thymus through blood vessels. There, they undergo a process of maturation that involves a negative selection of all T cells with T-cell receptor (TCR) that have high affinity to self-peptides, resulting in a final population of T cells with TCRs that have high affinity for foreign (non-self) antigens. At this stage, the matured T cells are called naive T cells, because they are not yet capable of generating a response against a pathogen [5]. After the maturation process, these naive T cells travel from the thymus to secondary or peripheral lymphoid tissue (lymph nodes and spleen), where they get activated through interaction with the APCs [6], such as dendridic cells. APCs process foreign pathogenic material, such as viruses, and present the antigen peptide on their surface bound to a molecule

known as the Major Histocompatibility Complex (MHC). The interaction between T cells and APCs is crucial for the immune response, since it is only after this interaction that T cells are then capable of mediating an immune response becoming effector T cells and undergoing to a process of proliferation to rapidly fight the infection [7].

Besides the TCR, T cells also express co-receptors on their plasma membrane. These co-receptors determine the type of MHC molecule that are expressed on the plasma membrane of the APCs that the T cells bind with. T cells can be differentiated into cells that express the co-receptor CD8$^+$, called cytotoxic T cells, and those expressing CD4$^+$ co-receptor, known as helper T cells. While CD8$^+$ T-cells bind MHC-class I molecules and are specialised in killing infected cells, CD4$^+$ T-cells bind MHC-class II and, upon activation, secrete cytokines that help other cells of the immune system to become fully activated effector cells [8]. In this work, I will focus on cytotoxic CD8$^+$ T-cell activation.

## 2.2 Cytotoxic CD8$^+$ T-cell activation

As introduced above, a pivotal event promoting CD8$^+$ T-cell (hereon called T cell) activation is the binding of TCR to the peptide loaded to the Peptide bound Major Histocompatibility Complex (pMHC) presented in the plasma membrane of APC and the cell-to-cell interaction. Upon TCR-pMHC binding, naive T-cells become activated.

T-cell activation upon APC interaction can be divided into three steps: TCR triggering, TCR mediated signalling, and immunological synapse formation.

### 2.2.1 T-cell receptor triggering

It is widely accepted that the first step of T cell-APC interaction is the TCR complex triggering. Located in the plasma membrane of T cells, the TCR complex consists of the TCR and its co-receptor Cluster of differentiation 3 (CD3). Because the TCR alone does

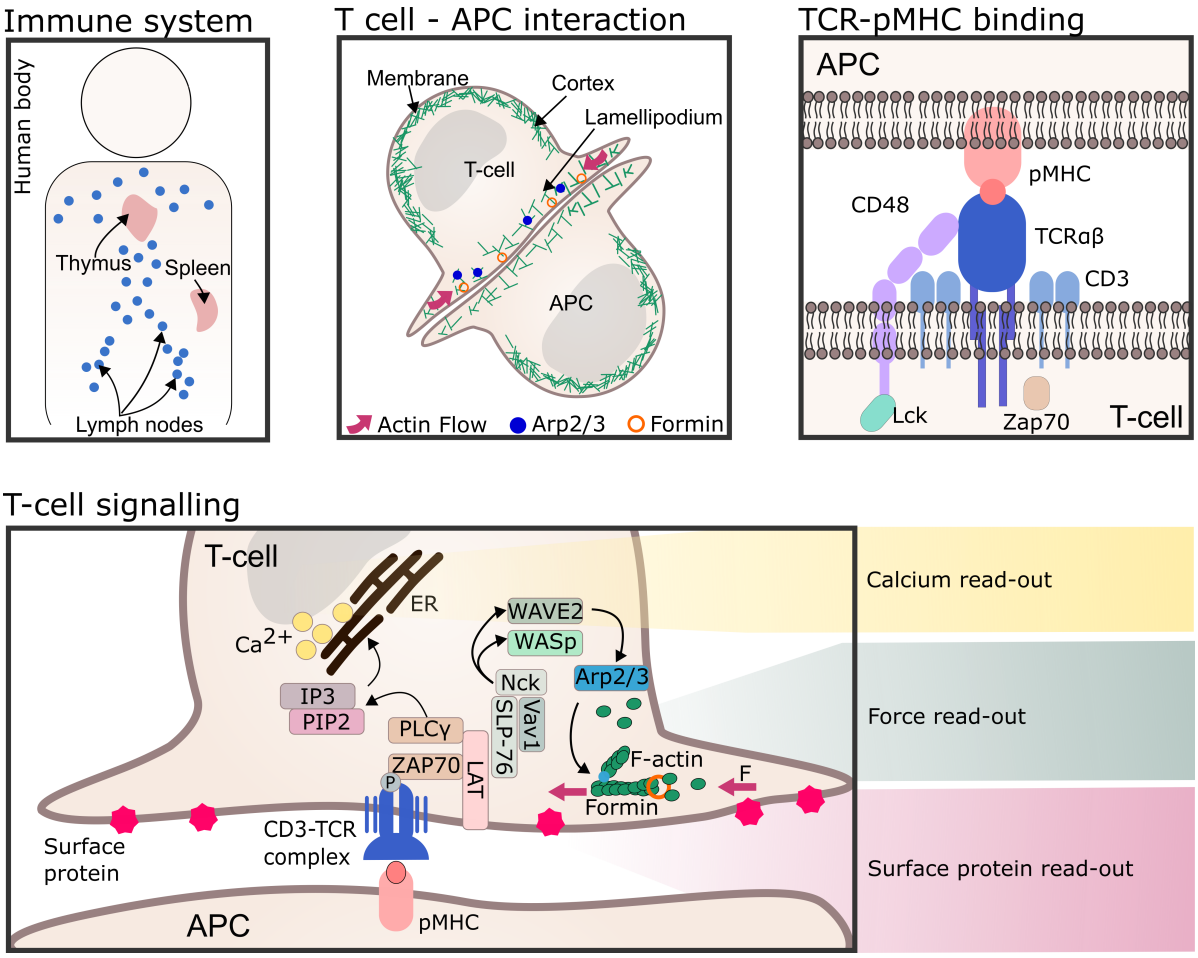



Fig. 2.1 Schematic of the immune system and T-cell activation. During their journey immune T-cells interact with the 3D biophysical environment from single cells to tissues, which involves mechanical force production. Generated from the bone marrow, T cells travel through the blood vessels to the thymus where they go into a process of maturation. In the thymus, the T cells that have high affinity to foreign antigens get selected. These then travel to secondary lymphoid organs (spleen and lymph nodes), where they get activated upon interaction with APCs. During activation, the T cell spreads on top of the APC surface, forming the IS. The lamellipodium, formed at the leading edge of the IS, consists of a dense actin network with the majority of Arp2/3 mediated branching and at the periphery formin-mediated actin filaments are branched. The later create a retrograde flow from the periphery towards the centre of the IS. T-cell activation starts with the binding event between the TCR and the pMHC complex on the surface of APC, which results in phosphorilation of CD3 ITAM domains by Lck and the recruitment of the Zap70 molecule. After TCR triggering, signalling events propagate by the recruitment of the scaffold proteins LAT. From LAT, PLC-$\gamma$ binds, which hydrolyses the membrane lipid PIP2, forming IP3, leading to the release of $Ca^{2+}$ from the ER. Also from LAT, SLP-76 binds, bringing Nck and Vav1. Vav1 activates Cdc42 and Rac1, leading to the activation and WASp and WAVE2. These activate the actin nucleator Arp2/3, leading to actin polymerisation which is involved in force production at the IS. At a later stage of T-cell activation, surface proteins are expressed on the external surface of the T cell.

not have intrinsic kinase activity, the co-receptor CD3 plays a crucial role in supporting and initiating the TCR signalling. CD3 is composed of four chains; CD3$\gamma$, $\delta$, $\epsilon$ and $\zeta$, each of them with an intracellular tail containing Immuno-receptor tyrosine-based activation motif (ITAM)s. Phoshorylation of the ITAMs by tyrosine kinase Lymphocyte-specific protein tyrosine kinase (Lck) initiates the signalling cascade [9]. In the resting state, the ITAMs of the TCR complex are dephosphorylated by the phosphatase, CD45. After T cell-APC engagement, integrin proteins, located in the plasma membrane of both cells bind together, such as ICAM-1 to LFA-1 and CD2 to LFA-3, bringing the membranes close together to a distance within the range of 10 nm to 40 nm [10]. Among several triggering models, the one named 'kinetic segregation model' predicts that this spatial proximity segregates molecules, such as CD45, inducing TCR-CD3 complex phosphorylation by Lck [11, 12].

### 2.2.2 T-cell receptor signalling

The second step is the well characterised signalling cascade [8]. Following phosphorylation of the TCR complex by ITAMs, Zap-70 (Syk-kinase zeta chain-associated protein of 70 kDa) binds the ITAMs domain and phosphorylates the transmembrane LAT (Linker of activated T cells), which binds SLP-76 (SH2 domain containing leukocyte protein of 76 kDa). LAT and SLP-76 recruit the phospholipase C-$\gamma$ (PLC-$\gamma$), which binds to LAT and gets activated by Itk (one of the Tec tyrosine kinase). PLC-$\gamma$ hydrolyses the membrane lipid PIP2 (Phosphatidylinositol 4,5-bisphosphate) into DAG (diacylglycerol) and IP3 (Inositol trisphosphate) [13, 14]. Next, IP3 diffuses to the Endoplasmic reticulum (ER), binds to the IP3 receptor (IP3R) and triggers the release of $Ca^{2+}$. Subsequent $Ca^{2+}$ fluxes result from $Ca^{2+}$ release-activation channels(CRAC) that allow extracellular influx of $Ca^{2+}$ [15]. Importantly, the signalling cascade does not promote only $Ca^{2+}$ release from ER, but also regulates actin cytoskeleton polymerisation. Several actin

regulators bind to SLP-76 protein, in particular Vav1 (Vav Guanine Nucleotide Exchange Factor 1) and Nck protein (non-catalytic region of tyrosine kinase adaptor protein 1). Vav1 activates the GTPases Cdc42 and Rac1, which then activate the actin regulators Wiskott-Aldrich Syndrome protein (WASp) and Wiskott-Aldrich syndrome protein family member 2 (WAVE2) respectively. WASp, together with WAVE2, leads to the activation of the actin nucleation factor Arp2/3 (the seven-subunit actin-related proteins-2/3) [16, 17]. By binding pre-existing actin filaments, the Arp2/3 complexes nucleate new short branched filamentous actin (F-actin), accounting for 80-90% of F-actin within the lamellipodium [18, 19]. T cells with low levels of WASp, lack in their ability to polymerise F-actin. Individuals with such cellular deficiency suffer from a severe immune deficiency disorder known as Wiskott-Aldrich syndrome (WAS) [20], highlighting the crucial role of actin cytoskeleton and its dynamics during T-cell activation.

### 2.2.3 Immunological synapse formation

Owing to the actin polymerisation, that is promoted by the TCR signalling cascade, the T cell undergoes a series of highly dynamic morphological changes, involving its spreading over the APC surface, and ultimately terminating with the formation of the Immunological synapse (IS) [12]. This process can be defined as the third step of T-cell activation. Downstream of the signalling cascade, after $Ca^{2+}$ release from the ER and actin polymerisation, the T cell starts to spread, increasing its contact area on the APC. This interface between the T cell and APC is called IS. Initial spreading followed by stabilisation and contraction of the contact area are the stages of IS evolution during T-cell activation. Once stabilised, a constant retrograde actin flow produces the mechanical forces to propel the TCRs from the periphery towards the centre of the IS [21, 22]. TCR/pMHC complexes form a cluster containing TCR and co-stimulatory and signalling molecules, such as ZAP70, SLP76, and LAT [23]. The TCRs cluster motion towards

the cell centre, with the consequent increase of the receptor density, thought to amplify TCR-mediated signalling [22, 24]. Crucially, TCRs move with the velocity of F-actin turnover, supporting the notion of coupling between F-actin and TCRs [25]. Stable IS is characterised by three concentric zones known as the central (c), peripheral (p) and distal (d), Supramolecular Activation Complex (SMAC) [26]. The cSMAC is known to contain high concentration of mobile TCRs, enriched with microvescicles for intracellular communication. It is in the cSMAC region that cytokines and cytotoxic granules are secreting to regulate other cells functions to support the immune response or to induce cell death, respectively [27]. The pSMAC is a region characterised by adhesion molecules such as LFA-1. Finally, the dSMAC contains CD45 and a dense network of dynamic actin [28].

## 2.3 Cell cytoskeleton structures and dynamics

The cytoskeleton of T cells is a crucial component for T-cell activation, from controlling cell morphology to promoting molecular motion. In general, the cytoskeleton of eukaryotic cells is composed of four structures: the actin cortex, the contractile rings, the actin-rich protrusions and the lamellipodia. The actin cortex consists of actin filaments undergoing constant turnover, conferring mechanical properties to the cell and controlling its shape changes [29]. The contractile rings and their mechanics are part of the cytoskeleton involved during cytokinesis, also known as cell division [30], while actin-rich protrusions are important during cell-to-cell interaction for scanning and sampling. Finally, the lamellipodium is a flat structure that can be formed as an extension of the actin cortex at the basal plane of the cell, for example during cell activation or migration. It is composed by 70% of Arp2/3 nucleated actin filaments that gives a highly dynamic characteristic, and 30% of formin mediated actin filaments that stabilise the structure [29].

### 2.3.1 Actin cytoskeleton

Actin is a protein with molecular weight of 42 kDa [31]. Actin is presented in two forms, as a monomer called G-actin and as filamentous polymer called F-actin [32]. The monomeric G-actin contains an Adenosine triphosphate (ATP) binding site, which energy released during the binding process helps the dimerization and trimerization of G-actin. [33]. The actin dimers and trimers can be next assembled to form a F-actin with the extremities called barbed end or (+) end, and pointed end or (-) end. Filaments are then disassembled through the hydrolysis of ATP to Adenosine diphosphate (ADP). The filament growing rate is controlled by the polymerisation and depolymerisation rate. While the polymerisation rate is more favourable at the barbed end, the depolymerisation rate is faster at the pointed end, giving the filament a growth directionality towards the barbed end. Overall, the actin filament self polymerisation is an energetically unfavourable event, therefore it is driven by two types of actin nucleators. The first is Arp2/3 complex, that binds existing filaments at an angle of 70 degrees and aids the F-actin growth along the new direction [34]. The second is formin, that works at the barbed end aiding the addition of new G-actin monomers [35].

Crucial for T-cell activation is the role of the actin cytoskeleton at the microvilli and lamellipodium. Microvilli are T-cell surface protrusions rich of F-actin. It has been proposed that their main role is to scan the external APC surface in search for antigens with high affinity to the TCRs, initiating T-cell activation [36, 37]. On the other hand, the lamellipodium, formed at the leading edge of the IS, consists of a dense actin network with the majority of Arp2/3 mediated branching. In the periphery of the lamellipodium, corresponding to the edge of the IS, formin mediated actin filaments are polymerised. The plasma membrane acts as a barrier giving an opposing force to the polymerised actin filaments creating a retrograde flow towards the centre of the IS. The actin retrograde flow is essential for T-cell activation because it is responsible for the

mechanical force generation to propel the TCRs from the periphery towards the centre of the IS [21]. Crucially, TCRs move with the velocity of F-actin turnover, supporting the notion of coupling between F-actin and TCRs [25]. In addition, experiments where actin filaments were disrupted by introducing a pharmacological perturbation using the drug Jasplakinolide showed results where the TCR motion was inhibited [38].

## 2.4 $Ca^{2+}$ signalling

An interdependent event to actin polymerisation, after TCR triggering, is the $Ca^{2+}$ release from the ER.

$Ca^{2+}$ signalling is crucial for carrying the immune cell response, without which the T-cell effector function would not take place. The release of $Ca^{2+}$ from the ER brings its $Ca^{2+}$ levels down. The decreased concentration is sensed by STIM1 (stromal interaction molecule 1), which activates the CRAC channels, such as ORAI1, at the plasma membrane, allowing external $Ca^{2+}$ to enter into the cytoplasm to sustain $Ca^{2+}$ levels for hours. The sustained concentration of $Ca^{2+}$ in the cytoplasm activates the calcineurin enzyme, which in turn is responsible for the activation of transcription factors that promote T-cell effector functions, such as metabolism, proliferation, differentiation, and cytokine secretion, that are all crucial for the immune response [39]. Among all the transcription factors, the NFAT (nuclear factor of activated T cells), that triggers IL-2 (interleukin-2) expression and promote T-cell proliferation, and NF-$\kappa$B (nuclear factor kappa-light-chain-enhancer of activated B cells), which leads to cytokine productions, are involved. Blockage of CRAC channels stops T-cell activation and proliferation and the consequent induced loss of the STIM1 and ORAI1 functionality is associated with immunodeficiency [40, 41].

$Ca^{2+}$ is maintained not only by the extracellular $Ca^{2+}$ flux, which is supported by the CRAC channels, but also from internal $Ca^{2+}$ sinks, such as the mitochondria. Using

Total Internal Reflection Fluorescence (TIRF) microscopy, it was observed that during T-cell activation mitochondria are translocated by the actin cytoskeleton towards the T cell-APC interface at around 200 nm away from CRAC channels [42]. This suggests that actin dynamics and the cytoskeletal remodelling are tightly connected to $Ca^{2+}$ signalling and T-cell activation. Interestingly, the CRAC channels cannot sustain $Ca^{2+}$ signalling alone, because the $Ca^{2+}$ ions inhibit them. For this reason, the sustained $Ca^{2+}$ flux relies on the support of the actin-mediated mitochondria translocation, which they act as a $Ca^{2+}$ buffer reducing the local level of $Ca^{2+}$ and therefore prolonging CRAC activity [41–43]. It has been observed that the inhibition of actin polymerisation by cytochalasin D, a drug that disrupts actin cytoskeleton, blocked the $Ca^{2+}$ levels from increasing and consequently T-cell activation [44]. On the other hand, experiments where the the $Ca^{2+}$ levels were altered shown a profound change in the actin cytoskeleton organisation rate [45]. In addition, prolongation of the TCR-pMHC lifetime is vital for triggering and sustaining $Ca^{2+}$ concentration, which is again actin-mediated.

Note, since $Ca^{2+}$ release is one of the earliest detectable signalling events during T-cell activation, in the time-scale of seconds, it is commonly used as an early activation marker [46–48].

## 2.5 Expansion and effector phases: expression of surface activation markers

Following T-cell activation, the expansion and effector phases take place. In the expansion phase, T cells start to proliferate in the lymph nodes, dividing rapidly and secreting cytokines, such as IL-2, the tumour necrosis factor $\alpha$ (TNF $\alpha$) and the interferon-$\gamma$ (IFN-$\gamma$), which are known to influence the function of other cells, such as proliferation, inflammation, and autoimmunity [27, 49–52]. During the effector phase, activated T cells

interact with target cells releasing cytotoxic granules, such as perforin and granzymes, causing cytotoxicity and apoptosis of the target cell [53].

The activation of T cells is accompanied by many markers expressed on their surface, known as activation markers, which naive T cells do not express [54]. Among them, there are the CD69, an early activation marker detectable within hours, and CD25 (interleukin-2 receptor), an activation marker regulated at a later stage and detectable after 24 hrs [55, 5, 54]. Finally, to identify T-cell exhaustion, the over-expression of the surface receptor PD-1 (programmed cell death protein 1) is used a marker [56, 57].

## 2.6 Mechanobiology in T-cell activation

Mechanobiology is a recent research field which focuses on how the mechanical force and the mechanical structure of single cells and tissues influence cell function. Having emerged no more than 25 years ago, mechanobiology is now considered a crucial component in health and diseases research, including the study of T-cell activation upon APC interaction [1, 2].

During their life cycles, travelling from the bone marrow to the thymus and from the thymus to the secondary lymphoid organs through the blood vessels, T cells interact with different three-dimensional biophysical environments (see Fig. 2.1). Those interactions are characterised by a diverse range of mechanical forces due to cell-cell and cell-tissue interactions and their diverse range of mechanical proprieties (i.e. stiffness), as well as hemodynamic forces within the blood vessels [58]. Among them, one fascinating event is the interaction between the T cell and APC, where mechanical forces are constantly generated during the whole process of T-cell activation. Yet, it is not known if the actin cytoskeleton plays a passive role during T-cell activation, being more a structural platform where signalling events can take place, or if it plays an active role, with its force generation being crucial for a full activation.

### 2.6.1 Mechanical force during T-cell activation

In the first phase of T-cell activation, the 'TCR triggering', the initial contact between the T cell and the APC takes place thanks to generation of actin-mediated ruffles and microvilli, which scan the APC surface for initiating the TCR-pMHC binding [59, 29, 36]. The actin-mediated ruffles induce integrins binding, such as ICAM-1 to LFA-1, bringing the membranes of the two cells together to a distance within the range of 10 nm to 40 nm [10]. The closer contact between T cell and the APC promotes TCR-pMHC binding through the extension of T-cell microvilli towards the APC surface [37]. Mechanical forces generated by microvilli are thought to be involved in the initial triggering. The work conducted by Liu *et al.* [60] shows that different force magnitude and duration applied to the TCR-pMHC bond influenced signalling events during T-cell activation. These forces, in the order of pico-Newtons (pN), had value of force (0 - 5 pN) close to the one experienced during membrane fluctuation due to thermal noise [61]. However, the relationship between the force generated during the early stage of activation and signalling events is not well understood yet.

Extensive work, instead, has been done over the past years to investigate the signalling pathways during the third stage of T-cell activation, that is the IS formation [41, 62, 63]. After the TCR-pMHC binding, the signalling cascade within the T cell activates the Arp2/3 actin nucleator promoting the polymerisation of short branched F-actin in the lamellipodium of the IS. There, actin undergoes a constant retrograde flow producing the mechanical force to propel the TCR from the periphery towards the centre of the IS. In addition, actin polymerisation is responsible for mitochondrial translocation for sustaining $Ca^{2+}$ flux and therefore T-cell activation. Blockage of actin polymerisation through different drugs such as, Jasplakinolide [64] (a peptide from the marine sponge used to destroy F-actin network) or cytochalasin D. [65] (fungal toxin that binds actin filaments at the barbed end preventing the dissociation and association of G-actin),

results in arrested TCR and mitochondrial motions, with the consequent perturbation of cellular $Ca^{2+}$ and T-cell activation, overall suggesting an active role of actin cytoskeletal force generation [38, 66, 44].

Finally, the mechanical force generated by the actin cytoskeletal is also actively involved in the binding lifetime of TCR-pMHC, tuning the length-scale and time-scale of TCR signalling and T-cell activation. Axial mechanical force with respect to the IS, defined as tension, is exerted on the TCR-pMHC bond [60]. Using Atomic Force Microscopy (AFM), it has been observed that small forces in the order of 50 pN exerted to the TCR by a cantilever functionalised with pMHCs increase $Ca^{2+}$ flux levels [67, 68]. This demonstrates that actin-mediated force generation is required for triggering T-cell activation.

### 2.6.2 Mechanical force influences T-cell function

Emerging studies indicate that the mechanical force generated during T-cell activation does not support only the cascade of events for the process itself to take place, but also influences the fate of T cells from their activation to differentiation and function [69]. One example is the cytoskeletal rearrangement, which is critical for IS formation, prolonged $Ca^{2+}$ signalling and nuclear activity, therefore linking the mechanical force generated at the synapse to T-cell function [58]. Another example is the possible influence of the mechanical force on chromatin structural change, which regulates T-cell selection and differentiation [70]. Indeed, the cytoskeletal mechanical force is not only sensed at the plasma membrane but is transmitted down to the perinuclear cytoskeleton, potentially influencing the chromatin conformation [71, 72]. Future research is also oriented in investigating whether metabolism and gene expression are regulated by the mechanobiology of the system and force production [58].

### 2.6.3 Mechanoadaptation during T-cell activation

The mechanical force involved during T-cell activation is responsible for influencing the T-cell function and fate, yet it is still not clear how it regulates the TCR signalling. Moreover, one of the main questions is whether the mechanical force generated on the external biophysical environment has a passive influence on the cell fate or there is an active feedback in which cells adapt their force generation to control their activation strength.

Studies investigating mechanoadaptation during T-cell activation are recently emerging. Among them, the one conducted by Colin-York *et al.* shows mechanoadaptation during T-cell activation when interacting with different peptide affinities. Specifically, using the 1G4 TCR Jurkat T-cells system, they demonstrate that the velocity of the actin retrograde flow changed with respect to the affinity of NY-ESO-1157-165 peptides, presented by HLA-A2 MHC molecules, normalising the peak force experienced by the TCR across all the antigens [25]. Tuning F-actin activity may thus be a mechanism allowing T cells to adjust their mechanical properties to their physiological needs. Other preliminary studies have explored the potential role of the external biophysical environment rigidity during T-cell activation. Using the Polyacrylamide (PAA) elastic gel functionalised with CD3/CD28, naive CD4 T-cells presented stronger activation response as a function of the elastic substrate rigidity (Young's Modulus (E) ranging from 10 to 200 kPa) [73]. Specifically, T cells shown larger adhesion sites on mechanically stiffer substrates ($E > 25$ kPa), whereas T cells cultured on soft substrates ($E < 25$ kPa) failed to form proper adhesion, highlighting the importance of biomechanical properties in T-cell activation [73, 74]. In another work, where the silicone based elastic gel Polydimethylsiloxane (PDMS) was used, it was observed that both $CD4^+$ and $CD8^+$ human T cells were proliferating at an higher rate when interacting with soft elastic gel ($E < 100$ kPa), compared to the stiffer substrate ($E > 2$ MPa) [75]. Even though some attempts were

done to investigate mechanoadaptation of T cells to the external biophysical environment, it remains elusive how T cells successfully sustain their activation while interacting with mechanically versatile APCs, with values ranging from 10 Pa to 2 kPa depending the inflammatory conditions [76], that present a diverse range of peptide affinities. To progress with mechanoadaptation studies, and more in general mechanobiology, the development of appropriate technologies is crucial. However, until now, there is a lack of methods for investigating mechanical force generation in T cells linked with signalling and functioning. Using mechanical force as the only read out specifically for investigating mechanoadaptation during T-cell activation can be reductive since force generation is registered also in other cellular events, such as migration and differentiation. Hence, the need of a gradual development of a toolbox for readouts that provide a basis for new discoveries during T-cell activation, linking together actin rearrangement and force production, $Ca^{2+}$ signalling and activation markers.

## 2.7 Biophysical readouts of T-cell activation

Understanding the highly complex machinery behind T-cell activation, with its myriad of mechanical, chemical and biological events to support its function, has been until now the grand challenge for health and disease studies. Unravelling its mechanisms is crucial for both basic and applied clinical research to advance the technologies for curing infectious diseases and cancer. Decisive for technology development is the identification of appropriate readouts and methodologies for quantifying the T-cell activation strength and consequently, the quality of immune response upon interaction with diverse external biophysical environments.

The readouts selected deeply depend on the stage of T-cell activation to investigate. For the early activation response, where the focus is mostly on the strength of T cell activation, actin dynamics and force production, together with $Ca^{2+}$ signalling, have

been mostly used as readouts [77–79, 25, 80, 38]. For later studies, for example the evolution from T-cell activation to its effector function, activation markers such as CD69 and CD25, cytokines such as IL-2 and the programmed cell death protein 1 (PD-1) have been used [5, 81–83]. Regarding the methodologies, progress has been made to develop technologies to quantify $Ca^{2+}$ levels released from the ER, actin cytoskeletal force generation and activation markers expression, with the aim to always meet the sensitivity readout of the physiological events, which are on the millisecond time scale and nano-length scale.

## 2.8 Methodologies for T-cell activation readouts

Building up a methodology for quantitative real-time readouts to probe mechanobiology during T-cell activation is pivotal for health and disease studies [1, 84]. As for many other biological experiments, this methodology requires the use of techniques and methods with the right spatial and temporal acquisition sensitivity, as well as statistical power to capture heterogeneous events in space and time. In this work, I will briefly discuss on the current methodologies existing for mechanical force, $Ca^{2+}$ signalling and activation markers detection.

### 2.8.1 Methods and techniques for measuring mechanical force on the biophysical environment during T-cell activation

Methodologies to measure mechanical force is of crucial importance for T-cell activation studies. A vast repertoire of methods and techniques are currently developed to either exerts an external force to the cell and measure its reaction, or to probe the force that the cell generates on the external biophysical environment. Some methods reproduce forces generated during peptide binding, while others mimic the material proprieties

of the external biophysical environment to measure the force that the cell exerts to it. I will briefly summarise some of these methods and techniques capable of measuring pico-Newton (pN) forces with nanometre (nm) displacements.

A common technique used to measure intracellular forces and traction force during cell adhesion is the Förster resonance energy transfer (FRET) force sensors-based technique [85, 86]. FRET is based on a donor-acceptor fluorophores system connected together by a flexible linker with known length. If the two fluorophores are close enough, after exciting the donor with a laser beam, the energy released is transferred to the acceptor, which emits at a different wavelength. If a given intra-molecular force is applied such that the linker is extended separating the two fluorophores, the FRET signal decreases. The FRET signal is used to measure small forces at the single-molecule level during cell adhesion and receptor-ligand interaction [87–90].

Different is the technique called AFM, that can be used to quantify mechanical proprieties in cells by applying an external force-load. AFM method consists of a cantilever whose tip can be functionalised with a rigid bead, a cell or a pMHC complex [91, 92, 67]. After exerting the cantilever against the cell surface, the nanoscale force indentations generated by the cell can be measured [92, 93, 91]. This method can be used to measure force generation during the binding interaction between TCR-pMHC or adhesion molecules [67, 94].

Along the same direction, another tool to exert force to the cell is the one using Optical tweezers (OTs) [95, 96]. Instead of a cantilever, OTs uses a light trapping mechanism to manipulate, pull, and stretch cells and measure mechanical force generation upon this external event. Implemented in a standard optical microscope, in a typical experiment with OTs a laser beam is focused with a high Numerical Aperture (NA) objective inside a medium of different refractive index compared to the external one, generating a force towards the center of the beam [96]. This technique can be used to quantify the

mechanical and contractile proprieties of T cells, strength of binding molecules with nN precision [97]. One possible application consisted in trapping a bead functionalised with pMHC complexes and exerting external forces to a T cell surface by oscillating back and forth the trapping beam [98].

Finally, there is a list of methods that by mimicking the external biophysical environment structure and rigidity, captures the mechanical force that the cells transmit to it. These methods are based on the use of elastic substrates, such as collagen, PAA and PDMS, with materials proprieties (dimensions, Young's modulus and Poisson's ration) that are know. Some examples are tissues and micropillar arrays [99–101], but the most widely used is Traction Force Microscopy (TFM), given its ease of implementation and its ability to simulate both the mechanical and biochemical external environment [102–105]. In a typical TFM experiment a cell is either let adhere on a 2D elastic substrate or is embedded inside it. In the first case, only the top surface of the elastic gel is then coated with fluorescent markers and functionalised with activation molecules. Once the cell is in contact with the gel, it activates generating mechanical force to the gel. The force deforms the gel which results in a displacement of the fluorescent markers. By tracking the markers using optical microscopy and by knowing the materials proprieties of the gel the shear and vertical forces (2D and 2.5D) generated by the cell on top of the gel can be recovered [106, 102]. Similar approach belongs to the second case, but this time since the cell is embedded in the gel, the fluorescent markers are mixed in the entire volume of the substrate and the 3D mechanical force can be extracted [107, 108].

### 2.8.2 Methods and techniques for measuring $Ca^{2+}$ signalling during T-cell activation

Being released from the ER within a few milliseconds (ms) after the TCR-pMHC binding, $Ca^{2+}$ is one of the earliest detectable signalling events during T-cell activation, commonly

used for activation quantification [109–111]. It has been observed that $Ca^{2+}$ intensity traces over time are very heterogeneous within a given cell population [47, 79, 78], demanding high statistical power to capture subsets of events and specific software for classifying the different $Ca^{2+}$ intensity traces.

One common method used in the past for $Ca^{2+}$ signalling measurements is Flow Cytometry (FC) [112]. FC is a high-throughput technique that uses multi-colour excitation lasers for multi-parameter detection. A solution containing thousands of cells is passed through the laser beams at rates of around 600 cells/s [113]. Each laser detects a variable, therefore measuring not only $Ca^{2+}$ but also the expression of activation proteins within the cell. The main advantage of FC is the high statistical power, registering ensemble $Ca^{2+}$ levels of millions (M) of cells. In addition, $Ca^{2+}$ flux within different cellular subsets can be measured by labelling the different protein markers expressed on the T cells surface after activation. However, because the signal of hundreds of T cells is measured every second, the readout represents the ensemble measurements of a population of T cells at a given time. Kinetics analysis can be performed but do not have single-cell resolution, rather one measurement will be obtained from different cells assuming that their average behaviour is constant. Hence, with FC rare events are neglected and averaged out, and the temporal information of signalling is lost.

A most recent technique considered now superior to FC is fluorescence microscopy [114, 115]. Using fluorescence microscopy, T cells can be tracked in space and time and their $Ca^{2+}$ signalling is registered with provided spatio-temporal context, essential for understanding T-cell activation and mechanoadaptation to the external biophysical environment. Used for fluorescence imaging are $Ca^{2+}$ indicators. An example are the ratiometric dyes, such as the fura dye, that show a spectral shift once they bind to the $Ca^{2+}$ ions [116, 117]. The advantage of a ratiometric dye is that the measurements are independent from the $Ca^{2+}$ indicator level within each cell, however they are mostly

activated with ultraviolet (UV) light causing phototoxicity to the cells. Other indicators are the genetically encoded FRET based sensors [118–120], such as the mCameleon reporter, that require however the establishment of a stable cell and animal lines expressing the $Ca^{2+}$ FRET sensor. Finally, another category are the Fluo dyes, such as Fluo-4, which penetrate to the cell membrane and increase of 100-fold their intensity upon binding to the $Ca^{2+}$ ions, but which $Ca^{2+}$ levels are not independent from the indicator concentration per single cell.

Despite the diverse range of technologies already available, fluorescence based $Ca^{2+}$ measurements remain still a challenge [109]. The heterogeneous nature of the $Ca^{2+}$ intensity traces, as well its fast dynamic (ms) demand statistical power, rapid acquisition time and image analysis software for classification of the different responses. Fritzsche *et al.* and Lee *et al.* [121, 78] proposed the $Ca^{2+}$ Quantification (CalQuo) software, for $Ca^{2+}$ analysis during T-cell activation, combined with fast imaging using the Confocal spinning disk (CSD) confocal microscopy. The novelty of this software is the automated detection and analysis of $Ca^{2+}$ response curves for single cells among hundreds of cells with a spatial resolution of micrometers and a temporal resolution of sub-second, using Fourier analysis. However, CalQuo is still limited in the statistical power compared to FC, it lacks of high-dimensional analysis registering only one single parameter, and its analysis pipeline necessitates expert users.

### 2.8.3 Methods and techniques for surface activation markers measurements

The most common technique used in immunological research for quantifying T-cell activation is FC [122]. As mentioned in the previous section, FC is an high-throughput technique that, equipped with multi-colour laser beams and multiple detectors, detects up to 20 parameters, from intracellular molecules to surface receptors, of $10^4$ - $10^5$

cells [123, 124, 122]. The advantage of this tools resides in the rapid acquisition of single-cell multi-parameter data with a speed of 600 cells/sec and the consequent analysis of sub-sets of cells, with high sensitivity for rare events [113]. However, FC does not offer spatio-temporal information at single-cell level. Cells suspended in a fluid are sent directly to the detection beams, and the results are averaged among the cell population at given time points. Consequently, single-cell activation with respect to the local biophysical environment and the dynamic tracing of signalling and activation molecules cannot be detected.

To overcome the lack of spatial and temporal informations, future research is oriented in moving towards fluorescence microscopy techniques where cells and the activation markers of interest can be labelled with dyes and/or fluorescent proteins for quantitative analysis during activation. The advantage would consist in tracking cells in space and time and extract over the course activation markers (e.g. cytokines released, CD25/CD69 expression) from their fluorescence emission. However so far these techniques are limited in their statistical power, restricting the number of cells analysed to $10^2$ - $10^3$, because of the limited Field-Of-View (FOV) of the acquisition camera.

## 2.9 Aim of the thesis

The aim of the thesis is to establish new quantitative biophysical methods with the right sensitivity to investigate the significance of mechanobiology in immune cell activation. To achieve the above aim, my thesis is divided in two parts. In the first part, I aim to develop new methodologies to allow 2D and 3D mechanical force generation readout in live-cells, with nano-length and sub-second time scales. My method of choice for force probing is TFM, given its ease of implementation and its ability to recapitulate both the mechanical and biochemical external environment. To increase TFM sensitivity, my objective is to combine the well-established TFM methodology with the super-resolution Structured

Illumination Microscopy (SIM) technique in 2D and 3D modalities. For the validation of the techniques, I will apply them to improve the spatio-temporal sensitivity and enable for the first time the investigation of small and rapid force production during adherence of HeLa cells, immune activation of Rat Basophilic Leukemia (RBL) cells and migration of primary salmon keratocytes, ultimately to enable sensitive force measurements in T cells. I intend to test the method across the above mentioned cell types to ensure the robustness of the right sensitivity regimes to enable T-cell force quantifications.

In the second part, I aim to develop a new methodology for $Ca^{2+}$ signalling and surface proteins readouts. To achieve this, my objective is to build an automated machine learning based software coupled with a new large FOV light-sheet microscope. For the validation of the new methodology, I will investigate $Ca^{2+}$ responses and activation marker expression in activated and resting primary Human $CD8^{+}$ T-cells. Finally, to add new insights into the different $Ca^{2+}$ responses, I will investigate simultaneously $Ca^{2+}$ signalling and IS spreading during activation of 1G4 Jurkat T-cells.

# Chapter 3

# Materials and methods

In this chapter, I present the materials and methods used throughout the thesis. I introduce the cell lines, microscopy techniques, biological and chemical techniques used for the experiments, and image analysis algorithms and software pipeline developed for their analysis.

## 3.1 Cell culture

### 3.1.1 HeLa cells

HeLa cells (Product 93021013, Sigma-Aldrich; mycoplasma tested) were cultured at 37 °C in 5% $CO_2$ with Dulbecco's Modified Eagle's Medium (DMEM, Sigma-Aldrich) supplemented with 10% FBS, 2 mM L-glutamine (Gibco, 25030081) and 1% penicillin-streptomycin (ThermoFisher, 15140122). HeLa cells were transfected accordingly to the protocol [125] and split every two days at a volume ratio of 1:5. Phenolred-free Leibovitz's L-15 medium (Gibco, 21083-027) was used for all the imaging acquisition.

### 3.1.2 RBL cells

RBL 2H3 clone cells (CRL-2256, ATCC, USA; mycoplasma tested) were cultured at 37 °C in 5% $CO_2$ with Minimum Essential Media (MEM) (Sigma Aldrich) containing 15% fetal bovine serum (FBS), 10 mM HEPES (Lonza, UK), 2 mM L-glutamine (Gibco, 25030081) and 1 % penicillin-streptomycin (ThermoFisher, 15140122). Cells were split every two days at a volume ratio of 1:5. 24 hrs prior to TFM experiments, RBL cells were treated with 0.05% Trypsin - EDTA (Lonza), facilitating their detachment from the cell culture flask and then moved to a rotating chamber at 37 °C in 5% $CO_2$ to maintain them suspended in solution. L-15 medium was used for all the imaging acquisition.

### 3.1.3 Primary salmon keratocytes

Salmon keratocytes were cultured in sterile medium consisting of Hanks' balanced salt solution (HBSS) (Mediatech, Inc. A Corning Subsidiary Manassas, VA 20109, USA), supplemented with 1 μg/mL amphotericin B, 100 μg/mL streptomycin, and 100 IU/mL penicillin [126]. For the salmon keratocytes, Atlantic salmon, *Salmo salar* L., were reared in marine water (salinity 3.5%) at 12 °C (Tromsø Aquaculture Research Station, Tromsø, Norway), and were fed with commercial salmon feed pellets (Skretting AS, Norway). Fish, each weighing 1200 - 1600 g, were sacrificed by an over-dosage of benzoak vet (ACD Pharmaceuticals AS, Norway) prior to cell harvesting, which is allowed according to Norwegian Regulations for use of animals in experimentation (https://lovdata.no/dokument/SF/forskrift/2015-06-18-761#KAPITTEL_10). This method is also in compliance with corresponding EU legislation - Directive 2010/63/EU (https://eur-lex.europa.eu/legal-content/EN/TXT/?uri=CELEX:32010L0063). Individual scales were removed from the dorsal and ventral region of the fish with forceps and placed on a petri dish with glass bottom. In order to let them attach to the silicone gel, the scales were allowed to dry for 30 sec, before adding the medium. The medium was

exchanged every 48 hrs. For the TFM experiments, salmon scales were placed on top of a gel (already placed into an imaging holder) overnight with HBSS, to let them adhere. After 24 hrs keratocytes in the form of a monolayer started to migrate from the scale onto the gel, ultimately separating into single cells. Salmon keratocyte membrane was labelled 5 minutes prior to the experiment with a 1:1000 CellMask Green (ThermoFisher, Green Plasma Membrane Stain) dilution in HBSS. The labelling solution was added directly into the sample chamber which contained the gel and the salmon scale. Cells were next washed with L-15 three times. The CellMask Green was stored at $-20\,^{\circ}\mathrm{C}$ to avoid degradation. L-15 medium was used for all the imaging acquisition.

### 3.1.4 1G4 Jurkat T-cells

Genetically modified Jurkat $CD8^+$ T-cells expressing only the 1G4 TCR were generated by Dr. Veronica Chang of the Davis Laboratory (University of Oxford, UK) and Dr. H. Colin-York. The 1G4 is a receptor that binds specifically to the New York esophageal squamous cell carcinoma-1 $(\text{NY-ESO-1})_{157-165}$ antigen [127–129], expressed by many types of tumours [130, 131].

1G4 Jurkat T-cells were cultured in sterile RPMI (Sigma Aldrich) supplemented with 10% FBS (PAA), 2 mM L-glutamine (Gibco, 25030081), 1 mM sodium pyruvate (Sigma, S8636-100ML), 10 mM HEPES (Sigma Aldrich), and 1% Penicillin Streptomycin (ThermoFisher, 15140122). Cells were maintained at $37\,^{\circ}\mathrm{C}$ and 5% $CO_2$ during culturing and, typically, kept at a density between 5-10 $\times$ $10^5$ cells/mL.

### 3.1.5 Isolation and activation of human $CD8^+$ T-cells

Peripheral blood mononuclear cell (PBMC)s were isolated from leukapheresis samples from healthy donors (obtained from the NHS Blood and Transplant Service) by Histopaque density gradient centrifugation (Sigma, 10771) and cryopreserved in liquid nitrogen.

**Day -1: isolation of CD8$^+$ T-cells** PBMC cells were thawed in 50 µl of 0.22 µm filtered-RPMI 1640 (Life Technologies, 31870-025) supplemented with 10% heat-inactivated human AB serum (Sigma, H4522), 1% Penicillin Streptomycin, 1% of 100×Glutamax (Gibco, 35050038), 1% Sodium Pyruvate (Sigma, S8636-100ML), and 0.1% 50 mM Beta-mercaptoethanol (Gibco, 31350010), referred to as RAB10. Additionally, 10 µL of 25 IU/µL Benzonase (Millipore, Cat. n. 2894174) were added to the media. Cells were centrifuged at 300 ×g for 10 min at room temperature and re-suspended at a concentration of 2 × $10^6$ cells/mL in the same media. Cells were left resting overnight in an incubator at 37 °C and 5% $CO_2$, with half lid open to allow the exchange of $CO_2$ and $O_2$.

**Day 0 - CD8$^+$ T-cells isolation** CD8$^+$ T-cells were negatively selected using the Miltenyi T-cell isolation kit (Miltenyi, 130-096-495) and the autoMACS separator. PBMC cells were re-suspended in a MACS buffer volume of (tot. number of cells/10)×40 µL. Biotin was added with a total volume of (tot. number of cells/10)×10 µL and incubated for 5 min. Next, a MACS buffer volume of (tot. number of cells/10)×30 µL was added to the cell suspension. Finally, Miltenyi beads (Miltenyi, 130-096-495) were added with a volume of (tot. number of cells/10)×20 µL, and the cell suspension was incubated for 10 min at 4 °C, after being well mixed. Cells were then separated using the autoMACS separator, and the final volume of CD8$^+$ T-cells was re-suspended in RAB10 at a concentration of 2 M/mL. After that, cells were pipetted in a 96-wells U-bottom plate, with 100 µL of cell suspension per well and left them resting for 3 hrs in an incubator at 37 °C and 5% $CO_2$. CD8$^+$ T-cells were activated using the Dynabeads human T-Activator CD3/CD28 (Gibco, 11131D). Dynabeads were vortexed for 30 sec and washed before use. Dynabeads were transferred into a 15 mL tube with 1 mL of cell medium for the washing step. The tube was then placed into a magnet for 1 min to let all beads being attracted to the tube wall. The medium was then removed gently, and beads re-suspended in 1

mL of fresh medium. Next, 50 μL of 0.2 M Dynabeads in cell medium and 50 μL of 10 IU/mL IL-2 (Proleukin, Novartis) were added into each well containing the cells to have a 1:1 cell to bead ratio.

**Day 3 - Analysis of CD8$^+$ T-cells** After 72 hrs of culture, CD8$^+$ T cells were transferred to a 15 mL tube. Next, the tube was placed into the magnet for 2 min to remove the Dynabeads from the cell solution. Cells viability was measured using an automated cell counter machine and the solution containing activated CD8$^+$ human T-cells was then used for experiments.

## 3.2 Microscopy

### 3.2.1 Atomic Force Microscopy

AFM measurements for testing the silicone gel stiffness were carried out by our collaborator Prof. E. Moeendarbary at the University College of London (UCL). AFM nanoindentation tests were performed with a JPK NanoWizard I (JPK Instruments) interfaced to an inverted optical microscope (IX81, Olympus). For the measurements, cantilevers with a 5 μm bead were used. Force indentation analysis were restricted to a depth of 100 nm.

### 3.2.2 Spinning disk confocal microscopy

A Zeiss CSD microscope operated with the Zen blue software was used for $Ca^{2+}$ and cell spreading analysis. The CSD microscope was equipped with the Hamamatsu ORCA-Flash4.0 v2 sCMOS camera and a 4× air 0.2 NA and 10× air 0.45 NA objectives. Several excitation lasers were used: a 488 nm laser was used for $Ca^{2+}$ flux measurements; a 405 nm for imaging dead cells labelled with Propidium iodide (PI); a 647 nm laser for imaging CD25$^+$ human T-cells; and lastly a 560 nm laser for cell spreading measurements.

Imaging were conducted at 37 °C and at 5% $CO_2$. For $Ca^{2+}$ imaging with dead cell and $CD25^+$ cell channels, first 1,000 frames were acquired in the $Ca^{2+}$ channel at an exposure time of 800 ms. At the end of the video, one single frame in both dead cell and $CD25^+$ cell channels was registered. For the $Ca^{2+}$ and contact area spreading assay, 1,000 frames in each of the two colour channels were acquired sequentially for a total of 2,000 frames. The exposure time in each channel was 800 ms.

### 3.2.3 TIRF-SIM

The Two-dimensional TIRF-SIM Traction Force Microscopy (2D TIRF-SIM-TFM) experiments were performed on the existing Total Internal Reflection Fluorescence SIM (TIRF-SIM) platform [132]. The microscope was controlled by a custom written LabView (NI) software [132]. For the sample excitation, a 488 nm wavelength laser (MPB Communications Inc. 2RU-VFL-P-500-488-B1R) and a 560 nm wavelength laser (MPB Communications Inc. 2RU-VFL-P-500-560-B1R) were used. TIRF-SIM is a Wide Field (WF) imaging technique in which excitation light patterns are formed by +1 and -1 diffraction orders generated by ferroelectric liquid crystal grating element, Spatial Light Modulator (SLM). These diffracted beams are focused at the back focal aperture of the objective lens. The placement of these focused diffracted beams at the back focal plane was carefully controlled in order to have TIRF of the beams at the interface between the silicone gel and sample medium above. The excitation beams coming from the lasers were collimated and passed through an acousto-optic tuneable filter (AOTF, AA Quanta Tech, AOTFnC-400.650-TN). After the beams were expanded, they were passed through a phase-only modulator, a polarising beam splitter, an achromatic half-wave plate (HWP, Bolder Vision Optik, BVO AHWP3), and then reflected on the ferroelectric SLM (SLM, Forth Dimension Displays, QXGA-3DM). The SLM was used to display a grating pattern on the sample. For each excitation light, the SLM had specific parameters to select,

in order to generate the diffraction patterns and adjust the critical angles for TIRF illumination at the interface between the silicone gel and the sample medium. The diffracted light was kept at s-polarisation using a polarisation rotator, to maximise the pattern contrast. All experiments were performed at physiological conditions using a micro-incubator (H301, Okolabs, Italy) at 37 °C and 5% $CO_2$.

In the case of Astigmatic Traction Force Microscopy (aTFM), a cylindrical lens (Optosigma, CLB-3030-1000PM) was placed in front of the camera to generate astigmatic imaging of the fluorescent beads. For each frame, the exposure time was 10-100 ms, leading to a super-resolution image (3 angles and 3 phase, 9 frames total) every 90-900 ms that was calculated using a reconstruction algorithm described previously [132, 133]. In addition, a high 1.49 NA (UAPON 100XOTIRF, Olympus) oil-immersion objective was used to achieve the TIRF modality and both the excitation lights were sent with an incident NA ranging from 1.38-1.41. Consequently, an incident angle of sin-1(1.41/1.515) = 68.5° has to be used. We calculated that the TIRF-SIM modality is maintained if cells pull or push the gel in the axial direction within 500 nm [134]. Given these settings, the excitation light passing through a gel thick 15 μm has an incident angle of 68.5° ± 1.5°, therefore allowing the use of a NA ranging between 1.395 - 1.42 values.

In the case of Three-dimensional SIM (3D SIM), the excitation light patterns are formed by +1, 0 and -1 diffraction orders and 15 raw frames (3 angles and 5 phases) are acquired to obtain a 3D super-resolution image.

## 3.3 Super-resolution Traction Force Microscopy

### 3.3.1 Silicone gel preparation

The silicone gel preparation consists of five steps: glass coverslip cleaning and drying, gel mixture formation, gel layer formation, gel coating and gel functionalisation.

**Glass coverslip cleaning and drying step** An homogeneous gel bulk is critical to maintain the desired optical properties on the top gel surface, eliminating any sort of scattering. In particular, this is of fundamental when super-resolution techniques such as SIM or TIRF-SIM modalities are adopted. Here we adopted the Piranha-acid method for glass cleaning. In a fume hood, a solution of Sulfuric Acid 95-98% (Sigma, 435589) and Hydrogen Peroxide (Sigma, H1009) was prepared in a 500 mL pyrex beaker with 3:1 ratio. In particular, using a 15 mL calibrated pyrex beaker, 15 mL of 99.00% sulfuric acid were added in the 500 mL pyrex beaker. Then, very slowly and using always the calibrated 15 mL beaker, 5 mL of 30% (wt/wt) hydrogen peroxide solution were added in the 50 mL beaker. The solution was mixed gently. Next, 18-mm #1.5 coverslips, with a nominal thickness of 175 µm, (Scientific Laboratory Supplies, UK) were added one by one ensuring that they did not overlap (around 15 coverslips), and incubated for minimum 2 hrs. Coverslips were then washed using 2 L of ddH2O water. Specifically, first 500 mL of ddH2O water were added to the acid solution. The solution diluted was then poured in a sink, making sure it was even more diluted mixing it with the water flux coming from the tap. The process was then repeated adding each time a smaller volume (around 200 mL) of ddH2O. For the final wash, ddH2O was left in the beaker with the coverslips, covered with aluminium foil and stored at RT for at most 1 month. Prior to the gel formation, the coverslips were dried with an air gun to avoid any water staining.

**High Refractive Index silicone gel mixture formation** The High Refractive Index silicone protocol was adapted from the Gutierrez's *et al.* work [135]. The silicone gel consists of two components called 920A and 920B (both by Quantum Silicones LLC, Richmond VA; refractive index of 1.49 when cured). Gel stiffness can be modified by tuning the two components ratios, see table 3.1. To prepare the silicone gel, the two components were mixed in an eppendorf pipetting first part 920A and then part 920B. The ratio was controlled using a weight scale. Because the two components are viscous,

Table 3.1 Ratio of 920A and 920B silicone gel components and relative stiffnesses quantified with the Young's modulus, E. Table adapted from Gutierrez's work [135].

| **920A** (%) | **920B** (%) | **Gutierrez *et al.* E (kPa)** | **Measured E (kPa)** |
|---|---|---|---|
| 1 | 0.95 | 0.4 | - |
| 1 | 1 | 0.7 | 15 |
| 1 | 1.1 | 3.7 | 31 |
| 1 | 2 | 18 | 105 |

the end of the pipette tip was cut before pipetting the gel. Once mixed, the silicone gel will start to polymerised within 30 min. Hence, at this stage all the next steps have to be executed quickly.

**Silicone gel layer formation** To remove the formation of bubbles inside the solution, a 50 µL tube containing the silicone gel mixture was placed in a vacuum chamber to remove as many bubbles as possible. This step was repeated for multiple rounds of 2 min each, to bring the bubbles on the gel mixture surface and then destroy them using air pressure. The same mixture was then degassed for 10 min using a sonicator bath at 14 °C and 100% of power. Silicone gels were then spin coated on top of 18-mm 1.5 # glass coverslips surfaces. The spin coater was used to obtain a flat and uniform gel layer. After placing an 18-mm coverslip on the spin coater, a drop of gel was pipetted on top of the coverslip. Gel layer thickness optimisation was performed tuning gel volume, spin coater speed and time (see Fig.3.1). For TFM experiments a thickness of 20 µm was made by spinning 50 µL of gel at 5000 RPM for 10 sec. Next, each coverslip with the gel layer on top was incubated at 100 °C for 2 hrs. After 2 hrs gels were cooled down at RT and then stored in Phosphate-buffered saline (PBS) at 4 °C.

**Coating silicone gel surface with fluorescent marker beads** To coat the top silicone gel surface with fluorescent beads, the surface was first activated with 10% of 3-aminopropyl trimethoxysilane (APTMS) (Sigma-Aldrich, UK) in dd2HO for 5 min.

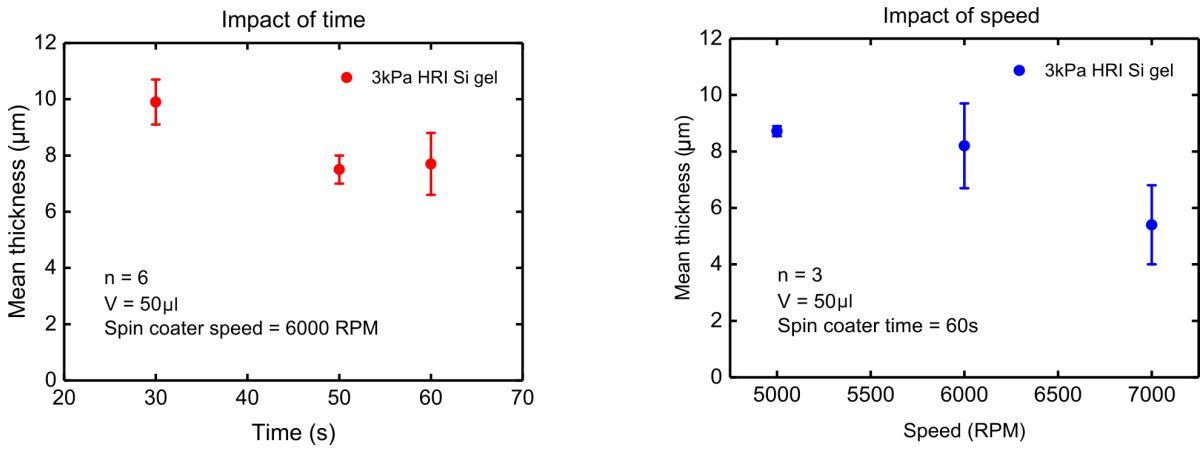



Fig. 3.1 High Refractive Index (HRI) Silicone gel thickness control. Left - Mean values of 3.7 kPa silicone gel thickness as a function of time: n. of gels = 6, speed of spin coater = 6000 RPM, volume = 50 µL. Right - Mean values of 3.7 kPa silicone gel thickness as a function of speed: n. of gels = 3, spinning time = 60 s, volume = 50 µL. Error bars are the standard deviation.

In particular, because silicone gel is hydrophobic, a volume of 200 µL was pipetted on top of each gel to cover most of the area. Using a 50 mL beaker full of ddH2O water, each coverslip with the gel layer was washed submerging the coverslip perpendicularly to the water for 10 times. Fluorescent marker beads were sonicated for 30 min using a sonicator bath at 14 °C and 100% power. Next, the gel was coated with a solution of 100 µL of 1-Ethyl-3-(3-dimethylaminopropyl) carbodiimide (EDC) at 100 µg/mL, 40 nm red fluorescent (580/605) FluoSpheres Carboxylate-Modified Microspheres (Invitrogen, UK) diluted in PBS (going up to 1:1000 for 2D TIRF-SIM technique), for 10 min at RT. Each gel was washed again 10 times. The reaction between APTMS and the silicone surface creates free amine-groups on the top surface of the gel, allowing functionalisation via EDC, a bi-functional cross-linker which binds to the free amine groups, which binds to Carboxylate-Modified Microspheres. At this stage, the gels can be stored in a 6-well plate with 2 mL of PBS per well, at 4 °C.

**Gel functionalisation with proteins** A support consisting of a Petri dish sealed with stretched out Parafilm was made to create a flat surface. Each gel was placed on

top of the Parafilm, with the gel side facing upwards. In the case of HeLa cell adhesion, the gel top surfaces were functionalised with a solution of 1 mg/mL fibronectin (FN) and 100 µg/mL of EDC diluted in PBS (Invitrogen, UK). Gels were incubated for 10 min at RT and then washed in PBS. For RBL cells activation, the gel top surfaces were first functionalised with a solution containing 1 mg/mL BSA, 100 µg/mL BSA-TNP and 100 µg/mL EDC. Gels were incubated for 1 hr at RT. Next, the gels were washed with PBS and then coated with 10 µg/mL of anti-TNP IgE (Clone IgE-3, BD Biosciences, 5541178) for 1 hr. As a final step, the gels were washed in PBS before usage.

### 3.3.2 Singular value decomposition analysis and best PIV selection

Computer-simulations were ran to understand the dynamic range of the 2D TIRF-SIM-TFM sensitivity improvement compared to WF Traction Force Microscopy (WF-TFM) (see 'Establishing a live-cell super-resolution Traction Force Microscopy' chapter). To asses the quality of the recovered displacement when using TIRF-SIM and WF imaging compared to the Ground Truth (GT), we executed quantitative Singular Value Decomposition (SVD) analysis using the well-established algorithm [136]. The aim was to build a TFM quality metric. To compare the levels of image distortion in the recovered displacement fields compared to the GT displacement fields, the respective displacements fields were diagonalised to extract the singular values. Next, The distance between the singular values extracted from the GT displacement field matrix and the recovered displacement field matrix was calculated using the SVD algorithm for both 2D TIRF-SIM and WF:

$$SVD_{qualityvalue} = \frac{\sqrt{\sum_{i=1}^{n}(S_i - \hat{S}_i)^2}}{k^2} \tag{3.1}$$

where S are the singular values of the GT, $\hat{S}$ are the singular values for the recovered displacement field, k is the image size and n is the number of singular values. The SVD quality metric values were then averaged over the 100 simulation repeats (see 2D TIRF-SIM-TFM section in TFM chapter). For better visualisation, the SVD quality metrics were converted into logarithmic scale and normalised by the global maximum SVD quality value for 2D TIRF-SIM-TFM and WF-TFM (resulting in values ranging from 0 to 1). A SVD quality metric value equals to one corresponds to the perfect match between the GT and the recovered displacement fields. The maximum SVD quality metric value as a function of Particle Image Velocimetry (PIV) window size informed the choice of the optimal PIV window size selection. The error bars were calculated by averaging the difference between the minimum SVD value and the two neighbouring values. The data analysis was done in MATLAB R2018b.

### 3.3.3 Accuracy and precision diagrams

For the interpretation of the TFM computer-simulation results (see 2D TIRF-SIM-TFM section in TFM chapter), we developed two scoring metrics defined as accuracy and precision diagrams. The accuracy diagram measures the fraction of simulation repeats that accurately recovers the total number of traction objects simulated, compared to the GT traction objects. To compute the accuracy diagram, the simulated GT and recovered displacement fields for 2D TIRF-SIM-TFM and WF-TFM were binarised according to a chosen threshold. This binary threshold was set in the case of the single- and triple-squared traction object such that all displacement values selected were larger than 80% of the average among the three displacement peaks. To find the displacement peaks value, since the objects location was a parameter known from the simulation, a line-profile centred on the objects was plotted and a peak finding algorithm was employed to find the position of the position of the displacements peaks. After binarising the

image and removing small objects using the built-in MATLAB function 'bwareaopen', the number of traction objects present in the recovered displacement field was extracted using 'bwlabel' and 'regionprops' for 2D TIRF-SIM and WF. This was run for each stress value and PIV window size over the 100 simulation repeats. To this end, the accuracy diagram score represents the fraction of the 100 simulation repeats where the correct number of traction objects were recovered. Following the same computation strategy, the precision diagram score represents the fraction of the 100 repeats where the maximum recovered displacement was within 20% of the maximum GT displacement value. The data analysis was done in MATLAB R2018b.

### 3.3.4 Migration speed

The migration speed of primary salmon keratocytes was estimated using the cell leading-edge location over time. Specifically, a cell profile along the axis orthogonal to the leading-edge was plotted over time, using the MATLAB function 'improfile'. At a given time point, the cell profile was characterised by a drop down, corresponding to the front leading-edge. This information was used to extract the leading-edge position. For each cell profile the first derivative was applied, using the MATLAB function 'diff', and the location of the maximum peak was extracted from the derivative plot within the range of 7000 to 1000 pixels, range where the cell's leading-edge was located. Lastly, all the leading-edge location values were plotted and by linearly fitting the plot the slope was extrapolated, which corresponds to the cell speed. The data analysis was done in MATLAB R2018b.

### 3.3.5 aTFM localisation calibration

To establish the shape of the astigmatic Point Spread Function (PSF) with respect to its position relative to the focal plane, an experimentally acquired astigmatic PSF

was modelled using cubic splines, as outlined in [137]. Specifically, a silicone gel with fluorescent beads sparsely distributed on top of its surface was used and a 2 μm z-stack with 10 nm step size was acquired. Using the MATLAB R2018b based software routine (https://github.com/jries/fit3Dcspline), a single 3D PSF stack was reconstructed by aligning and averaging each of the beads present in the image, followed by a cubic spline interpolation. This serves as a PSF model that can be used to extract the position of each bead by comparing it to the experimental data. To obtain the localisation in x,y, and z of each bead, the MATLAB based software routine (https://github.com/jries/fit3Dcspline) was used, together with the PSF model acquired from the calibration. The software utilises a maximum likelihood estimation (MLE). After extracting the bead positions, they were linked into trajectories using the single-particle tracking Python library known as trackpy (https://soft-matter.github.io/trackpy) [138]. Next, all trajectories were corrected for 3D sample drift using a sub-set of reference beads far away from the cell contact. Trajectories were also filtered using a median filter (width = 10 frames) to remove spurious localisations. The displacement field at each frame was produced by interpolating the individual bead displacements onto a regular grid, followed by a spatial median filter of width 10 px (604 nm).

### 3.3.6 Lateral resolution estimation for TIRF-SIM and WF

Gels with sparse beads distribution on the top surface were prepared to estimate the Full Width at Half Maximum (FWHM) of the TIRF-SIM and WF PSFs. Specifically, the median value of the FWHM along x and y was extracted using the 'feature2D' function run in MATLAB R2018b.

### 3.3.7 Statistics

The FWHM of both the TIRF-SIM PSF and WF PSF, were computed for at least 300 fluorescent beads, in at least 3 independent experiments. For the TFM computer-simulations were executed in 100 independent simulation repeats for each stress value and each PIV window size, respectively. All the biological experiments with HeLa, RBL and salmon keratocytes conditions were acquired in at least 3 independent days and data were analysed in more than 20 individual cells per cell type.

## 3.4 Automated single-cell high-throughput $Ca^{2+}$ platform

### 3.4.1 CalQTrace software description

Calculation and Quantification of signalling Traces (CalQTrace) software was built to detect and track in space and time immune cells during activation, exclude and separate sub-populations of cells, and extract and classify $Ca^{2+}$ signalling at single-cell resolution over time, using a machine learning based approach. To make it user-friendly, CalQTrace was implemented within a Graphical User Interface (GUI).

The image analysis pipeline of CalQTrace was written in Python 3.7. The GUI was created with Qt [139] and Matplotlib was used for plotting. Both the cell detection, that uses a gaussian blob detection algorithm, and cell tracking analysis were performed using the Crocker-Griger method [140] and implemented in the Python library Trackpy [138]. For the $Ca^{2+}$ intensity classification, a 1D Convolutional Neural Network (CNN) with dense layers for classification is used [141, 142].

CalQTrace contains five steps, displayed as separate tabs in the GUI, corresponding to $Ca^{2+}$ labelled cells detection, exclusion and separation of specific cell sub-populations,

cell tracking and $Ca^{2+}$ signalling intensity traces classification in the three main categories of single-peak, oscillatory and non-triggering. Below a detailed explanation of all the 5 sections together with a GUI guide.

**Cell detection** The first section of the software is 'Cell detection'. Here the user is asked to load the $Ca^{2+}$ data. The data has to be a three-dimensional (t,x,y), 8-bit image stack of $Ca^{2+}$ data. Once open, the user can explore the dataset, either by pressing the 'play' button, or manually using the slider in the GUI. Cells are detected using the 'tp.locate' function from Trackpy, in which two parameters need to be set. The first one is the cell diameter, determined by zooming on one or a couple of cells or using the ImageJ software [143]. The second one is the minimum brightness, corresponding to the minimum sum of pixels within the cell area expected for a cell. Areas with a lower brightness will be considered to be noise and will be excluded. The use can test these two parameters on a couple of frames by clicking on 'Apply to current frame', until a satisfying cell detection on several non-consecutive frames is found. Once this is done, the user can click on 'Apply to all frames'.

**Cell exclusion** The second section is the 'cell exclusion'. Here the user can exclude a specific sub-population of cells labelled with a second marker, in this work specifically dead cells labelled with PI. This is an optional section that can be run only if the user has the data. To exclude dead cells from the analysis, a single frame in the format of (x,y) 8-bit image, acquired in a separate colour channel only at the end of the $Ca^{2+}$ stack acquisition, can be loaded. To exclude the dead cells sub-population, first a mask indicating the position of dead cells was calculated. For this, the second channel was segmented with a manually defined threshold. Binary closing using the library scikit-image [144] was used to fill up gaps when necessary. Cells detected in the last frame of the $Ca^{2+}$ channel were determined to be dead when located within the mask. To limit

false positives caused by noise, only cells for which 75% of pixels were masked within a square area centred around the cell position (with a lateral size equal to the cell radius) were considered as dead.

**Cell separation** The third section is 'Cell separation'. This section separates in two sub-populations the live cells detected. To do so, similar to the 'cell exclusion' section, cells were labelled with a third marker to acquire a single frame in the format of a (x,y) 8-bit image in a separate colour channel at the end of the $Ca^{2+}$ image stack acquisition. In this work the anti-CD25-APC-R700 antibody marker was used to separate $CD25^+$ cells from $CD25^-$. Cell were detected using the same method of the 'cell exclusion' section and then separated in two categories.

**Tracking** In the fourth section, defined as 'Tracking', the positions of each cell is linked across frames (time points) using the Crocker-Grier's method [140]. In this section the user is asked to set three parameters. The first is the minimum track length that is the minimum number of frames in which a cell must be present in the entire $Ca^{2+}$ video for a track to be kept. Next is the search range, that is the maximum distance the cells can move between consecutive frames. Finally, the last parameter is the memory, that is the maximum number of consecutive frames during which the cell detection is interrupted but still considered the same object. Once the parameters are set, the user only needs to click the 'Apply' button and the tracking results will be displayed.

**Intensity extraction and classification** The fifth and final section is the 'Intensity extraction and classification'. In this section, $Ca^{2+}$ intensity traces are extracted from each of the cells and classified into non-triggering, single-peak and oscillatory responses via a 1D CNN algorithm. Intensity traces from each single cell were extracted by integrating at each time point the total intensity within a 2x2 pixels area, centred in the centroid of

each single cell. The intensity traces were then normalised to the maximum intensity value among all cell population. Finally, the $Ca^{2+}$ intensity traces were then passed trough a 1D CNN model we generated with manually trained data. The percentage of the three different activation responses is plotted in the GUI. All data containing the tracking coordinates, the parameters used in the five sections, and the classification outcome can be saved as excel format.

### 3.4.2 1D CNN model

To classify calcium intensity traces in non-triggering, single peak, and oscillatory responses, we generated a supervised 1D CNN model. For that we used two pairs of datasets with two different cell types: the 1G4 Jurkat T-cells line and the primary human PBMC T-cells. The data were acquired on different days and under different activation conditions (different peptides and negative control) using the Spinning disk microscope. The intensity curves were classified manually by a single individual with a home-built script written using MATLAB R2018b. Regarding the CNN algorithm, we chose a normal structure for classifying 1D data (see Fig. 3.2).

```
# define a CNN
def CNN(X, y, test_dt_reshape, test_cl_reshape, n_testing_data, Int_profile_len, Name_file, PARAMETERS, i, iteration):


    cnn = Sequential()
    cnn.add(Convolution2D(64, 3, 1,border_mode="same",activation="relu",input_shape=(Int_profile_len,1, 1)))
    cnn.add(Convolution2D(64, 3, 1, border_mode="same", activation="relu"))
    cnn.add(MaxPooling2D(pool_size=(2,1)))

    cnn.add(Convolution2D(128, 3, 1, border_mode="same", activation="relu"))
    cnn.add(Convolution2D(128, 3, 1, border_mode="same", activation="relu"))
    cnn.add(Convolution2D(128, 3, 1, border_mode="same", activation="relu"))
    cnn.add(MaxPooling2D(pool_size=(2,1)))

    cnn.add(Convolution2D(256, 3, 1, border_mode="same", activation="relu"))
    cnn.add(Convolution2D(256, 3, 1, border_mode="same", activation="relu"))
    cnn.add(Convolution2D(256, 3, 1, border_mode="same", activation="relu"))
    cnn.add(MaxPooling2D(pool_size=(2,1)))

    cnn.add(Flatten())
    cnn.add(Dense(1024, activation="relu"))
    cnn.add(Dropout(PARAMETERS['dropout'])) #0.5
    cnn.add(Dense(PARAMETERS['n_classes'], activation="softmax"))
```

Fig. 3.2 1D CNN model used.

The network consists of Convolution2D layers to compute a dot product between weights and inputs, with a kernel size of 3x1 and at the end the ReLU activation function to produce nonlinearities in the model; a Maxpooling2D function to reduce the spatial size of the data, in order to reduce the amount of parameters and computation in the network, controlling therefore a possible overfitting; a Flatten layer to convert all the final outputs in a 1D feature vector; a Dropout layer with rate 0.8, used to reduce overfitting in neural networks, specifies a percentage (expressed in rate) of elements that will be randomly dropped out during training; Dense layers, which perform classification on the features extracted and downsampled by the convolutional 2D and pooling layers respectively. The last dense layer of the CNN contains a single node for each class. As optimizer we used the state-of-the-art Adaptive Moment Estimation (ADAM) [145]. ADAM, in addition to the standard decay value (term used to update the weights to exponentially decay to zero), computes adaptive learning rates for various parameters from estimates of first and second moments of the gradients [145]. The optimal decay and learning rates selected were 0.0001, according to the accuracy of the prediction outcome. To exclude noise coming from single traces and to speed up the machine learning process, the intensity traces were downsample to obtain a shape that is a base of 2 ($2^x$), paying attention to not lose important details. Specifically, we downsampled from 1000 to 128 data points. Next, to increase the amount of training data, the intensity traces were duplicated four times adding each time a different intensity noise level or a frame offset. The frame offsets were randomly generated within a range of 0 and one third of the intensity curve length, while the noise added was a random noise with gaussian distribution. The 1D CNN model training was iterated 3 times, with 40 epochs, and a batch size of 10. At every iteration, new independent data were used, dividing training and testing groups in three subgroups. During each training, 0.1% of the data in the training group are only used for validation (and not actually for training). For testing the 1D CNN model, separate new datasets

were used, reporting the activation of 1G4 Jurkat T-cells and primary human PBMC T-cells. The curves in each of the datasets were manually classified by one single user.

### 3.4.3 pMHC protein production

The production of the pMHC to activate the 1G4-TCR Jurkat T-cells was carried by Dr. Veronica Chang of the Davis Laboratory (University of Oxford, UK) and Dr. H. Colin-York. The 1G4-TCR binds specifically to the NY-ESO-$1_{157-165}$ peptide. From the NY-ESO-$1_{157-165}$ peptide, two different variants were produced on a MHC class I complex. The first variant, referred in this work as 9V, had a mutation to valine at the 165 position. The second variant, referred as 4D, had a mutation to aspartate at the 160 position [78, 127].

### 3.4.4 Protein biotinylation

To specifically functionalise the glass coverslips, the anti-human-CD3 antibody, OKT3, and two experimental peptide-MHC complexes, 4D:MHC and 9V:MHC, were biotinylated to facilitate binding to the streptavidin functionalized glass coverslips.

The PD mini-trap G25 (PD MiniTrap G-25, 28922529) were used for the process. After washing the mini-trap for 3 times in PBS (see protocol $https://gels.yilimart.com/Assets/Images/doc/file/28918007_INSTRUCTION_02.PDF$), executed to remove any component containing amine that would bind to the biotin-NHS, a minimum volume of 50 µL of a given protein at a concentration of at least 1.2 mg/mL was pipetted into the mini-trap. After centrifuging for 2 min at 1000 ×g, the protein solution was collected and the concentration measured using the NanoDrop 2000/2000c spectrophotometers. Next, 2.2 mg of the Sulfo-NHS-LC-Biotin were dissolved in ddH2O, and a biotin volume accordingly to the below equation

Table 3.2 $k_{off}$ rates of the BSA protein, the OKT3 antibody, the 4D and 9V peptides.

| **Protein** | Peptide sequence | $\mathbf{k}_{off}$ $(s^{-}1)$ | Reference |
|---|---|---|---|
| BSA | - | - | - |
| OKT3 | - | 0.39 | (Kjer-Nielsen, L *et al.*, 2004) [146] |
| 4D | SLLDWITQV | 2.59 | (Aleksic, M *et al.*, 2010) [127] |
| 9V | SLLMWITQV | 0.33 | (Aleksic, M *et al.*, 2010) [127] |

$$Vol_{biotin} = 10 \times \frac{MW_{biotin}}{MW_{protein}} \times \frac{c_{protein}(mg/mL)}{c_{biotin}(mg/mL)} \times vol_{protein}(mL) \tag{3.2}$$

was added to the protein solution to have a 10:1 biotin:protein ratio, where *Vol* is volume, $c$ is the concentration and $MW$ is molecular weight. The mixed solution was then incubated for 30 min at RT. After centrifuging the solution using the mini-trap for 2 min at 1000 g, the final concentration of the biotinylated protein was measured and stored at 4 °C for at least 1 month. The biotinylation of the experimental proteins was verified comparing the $Ca^{2+}$ responses of the 1G4 Jurkat T-cells when activated with plain (biotin-BSA and streptavidin) and functionalised (biotin-BSA, streptavidin and biotin-(pMHC)) glass coverslips. The $k_{off}$ rates of the peptides and anitobody are reported in the Table 3.2.

### 3.4.5 Coverslip functionalisation

All experiments were conducted on 18 mm, #1.5 glass with a nominal thickness of 175 µm, round coverslips (Scientific Laboratory Supplies, UK). Each coverslip was first coated with 100 µL of 100 µg/mL biotin-BSA (b-BSA), at a b-BSA:BSA ratio of 10:1, in dd2HO water. After 2 hrs of incubation with the biotin-BSA at RT, the coverslips were washed three times in 2 mL of PBS. Coverslips were then coated with 100 µL of streptavidin at a concentration of 4 µg/mL and incubated at RT for 1.5 hr, followed by a three times washing steps with 2 mL of PBS. Next, coverslips were coated with 20 µL of either

biotinylated pMHCs (b-9V or b-4D), or biotinylated OKT3 (b-OKT3) at a concentration of 2 μg/mL. After a further 1.4 hrs of incubating at RT the coverslips were washed with 2 mL of PBS three times and stored at 4 °C until required for imaging. Coverslips were prepared fresh on the day of the experiment.

### 3.4.6 $Ca^{2+}$ assay with dead and $CD25^{+}$ cell markers

Prior to $Ca^{2+}$ experiments, an HEPES-buffered saline (HBS, 51558; Sigma, UK) buffer was prepared. The HBS buffer contained 500 mL of 20 mM Hepes and 150 mM of NaCl in dd2HO. The pH solution was brought from a value of 5.5 to 7.4 by adding slowly 1 mol of NaOH solution. From the HBS mother stock, a 100 μL solution of HBS with 2.5 μM of probenecid (ThermoFisher, P-36400) was made. Primary human $CD8^{+}$ T-cells at a concentration of $0.5\times10^{6}$ and a cell viability of 80%, were re-suspended in a solution containing 50 μL of HBS and probenecid, 50 μL of L-15 and 10 μL of anti-CD25-APC-R700 antibody (Biosciences, catalog n. 565106). The cells were incubated for 10 min at RT in the dark. After that, 1 μL of 1 mM Fluo-4 (ThermoFisher, F-14201) in Dimethyl sulfoxide (DMSO), and 5μL of PI per $0.5\times10^{6}$ cells were added to the solution and properly mixed. The new solution was incubated in a rotator plate for 5 min at a speed of 500 RPM and a temperature of 37 °C. Next, the cells were centrifuged for 3 min at 1200 RPM and re-suspended in 20 μL of HBS with probenecid. Cells were imaged immediately after using the CSD microscope with a 4× objective. After placing the functionalised 18-mm coverslip into the scope, and using few cells to focus at the top glass surface, the imaging started. At this step, 20 μL of the labelled cell solution were pipetted on top a functionalised 18-mm coverslip, imaging the landing event and the T-cell activation. For this experiment, a stack of 1,000 frames was recorded at an exposure time of 800 ms. After that, one single frame for each of the other two-colour channels was acquired. The experiment was conducted at 37 °C and 5% $CO_2$.

### 3.4.7 $Ca^{2+}$ and contact area spreading assay

The 1G4 Jurkat T-cells at a concentration of $0.5\times10^6$ cells/mL and a cell viability of 80% were re-suspended in a solution containing 50 µL of HBS and probenecid, 50 µL of L-15, 1 µL of 1 mM Fluo-4 (ThermoFisher, F-14201) in DMSO, and 2 µL of 1:1000 CellMask Orange (Thermofisher, A57244) solution diluted in dd2HO. After 5 min of incubation in rotator plate at a speed of 500 RPM and a temperature of 37 °C, cells were centrifuged and re-suspended in 20 µL of HBS with probenecid. Cells were imaged immediately after using the CSD microscope with a 10× objective. After placing the functionalised 18-mm coverslip into the scope, and using few cells to focus at the top glass surface, the imaging started. At this step, 20 µL of the labelled cell solution were pipetted on top a functionalised 18-mm coverslip, imaging the landing event and the T-cell activation. For each experiment, a two-colour channel stack of 1,000 frames per channel was recorded at an exposure time of 800 ms, for a total frames of 2,000. The experiments were conducted at 37 °C and 5% $CO_2$. For each activation condition,

### 3.4.8 $Ca^{2+}$ image pre-processing

Dual-colour image stack files of $Ca^{2+}$ signalling and cell spreading were first pre-processed using ImageJ [143]. Specifically, the stack file in Carl Zeiss Image (*czi*) format was transformed in a 8-bit *tiff* format file.

### 3.4.9 Development of a cell segmentation plug-in

All the images in the CellMask labelled channel were segmented using the 'watershed' algorithm. The watershed algorithm uses gradient intensity as a topography surface for segmenting objects (https://scikit-image.org/docs/dev/auto_examples/segmentation/plot_watershed.html). The gradient intensity is built in a way that the darkest pixels are in the center of the objects and used as markers for initiating the flood-filling, and the

lightest pixels at the object contour. However, the watershed algorithm can sometimes under-segments clusters of objects (in our case cells) into a single object. To overcome this limitation, a pre-cell coordinates detection step was applied. To run the watershed algorithm with high robustness, we needed the binarised image of the CellMask channel and the single-cell coordinates. The cell spreading pipeline was written in Python 3.7 and implemented in the CalQTrace software. The libraries used where Scikit-image [144] and SciPy [147].

**CellMask binarisation** We started by binarising each of the images of the CellMask image stack. Because these data had low signal-to-noise ratio, first a 'derivative-based Sobel edge detection' algorithm was applied to detect cell contour (see Fig. 3.3a). Next, a threshold value above 40% of the pixel values in the cell contour images was applied for binarisation. Finally, both 'objects removal' and a 'filling-holes' functions were applied to remove objects smaller than half of the cell area and to close all the segmented objects (see Fig. 3.3b). The libraries used where Scikit-image [144] and SciPy [147].

**Cell coordinates extraction** From the Sobel algorithm application, the bright spot inside each cells was used for identifying cell coordinates. First, a 2D convolution called 'convolve2d' with a 10×10 kernel with values equal to 1/100 was applied to blurred each cell so that only one bright peak spot could be found (see Fig. 3.3c). To separate the foreground from the background, the processed images were multiplied with the previously binarised images. Next, for each image, all connected objects (single cells and cell clusters) were labelled and the maximum brightness within each labelled region was extracted. For better image processing, each connected object was normalised, creating a uniform maximum brightness distribution across the FOV (see Fig. 3.3d). To do so, each region was multiplied by a normalisation factor. A maximum filter was applied to underlying more the local maxima by increasing their region. Finally, to find the peaks,

both a 'peak local maxima' function and a 'binary dilation' function were applied (see Fig. 3.3e). The library used was SciPy [147].

**Watershed segmentation** The local maxima found were incorporated to the binarised images, and used as markers for the watershed algorithm (see Fig. 3.3f). Specifically, the markers were set as the darkest points in the images by inverting the image (see Fig. 3.3e,f). The highest points, instead, were the cell values. From the combined markers and binarised images, the watershed cell segmentation was obtained (see Fig. 3.4). The libraries used where Scikit-image [144] and SciPy [147].

### 3.4.10 Implementation of cell segmentation into the CalQTrace pipeline

The cell segmentation pipeline was added to the CalQTrace software (but not implemented in the GUI) after the 'cell tracking' section. From the cell tracking algorithm, an unique ID is assigned to each cell. Assuming that the cell coordinates in the $Ca^{2+}$ channel, extracted using Trackpy, would correspond to the same cell coordinates in the cell spreading channel, the cell contact area spreading and the $Ca^{2+}$ signalling were associated to a specific cell ID. Because the cells in the two colour-channels might not perfectly overlapped in space, a minimum distance between the cell coordinates in both channels was implemented to the same cell ID. For each cell presented in the image FOV, a 1D $Ca^{2+}$ signalling intensity trace and a 1D contact area spreading trace were extracted, as a function of time (frame points).

### 3.4.11 Statistics

The preliminary biological experiment with primary human $CD8^+$ T-cells had only one repeat. The biological experiments with the 1G4 Jurkat T-cell model consisted of 3

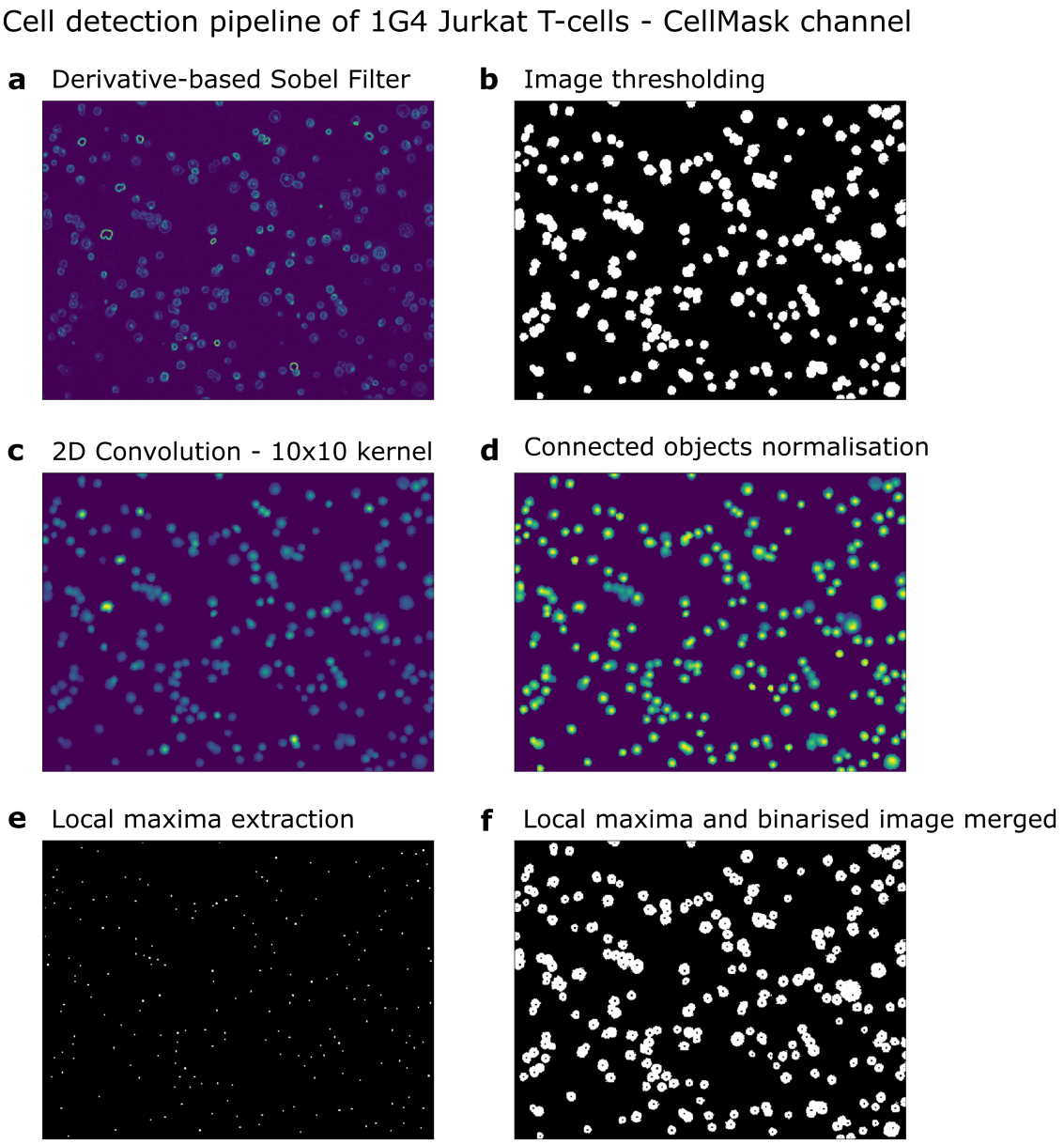



Fig. 3.3 Cell segmentation plunging pipeline in 6 steps. (**a**) Edge-detection using the derivative-based Sobel algorithm. (**b**) Binarisation of the image in (a), based on thresholding. 'objects removal' and a 'filling-holes' functions applied. (**c**) 2D convolution of the image in (b) with a 10×10 kernel. (**d**) Brightness normalisation of each connected objects across the entire FOV from image (c). (**e**) Local maxima extraction from image in (d). (**f**) Binarised image in (b) multiplied with the inverted local maxima image in (e). Scale bar is 100 µm. Data produced in collaboration with G. Chappelle.

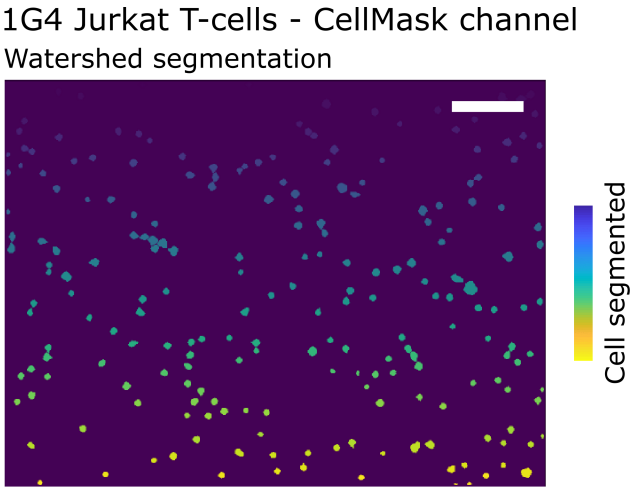



Fig. 3.4 Cell segmentation outcome. Single frame of 1G4 Jurkat T-cells from the CellMask channel, showing the cells segmented labelled accordingly to the viridis color map range. The gradient in brightness is used just as visual separation of the different cell segmented. Scale bar is 100 µm. Data produced in collaboration with the master student G. Chappelle.

repeats per activation condition, acquired in 3 independent days. T-test was used for assessing the distributions. The comparison between the different $Ca^{2+}$ responses was done using the one-way ANOVA, with a significance set for p-value $< 0.05$. When significance was registered, a pairwise posthoc analysis was conducted using the Tukey's Honestly Significant Difference (HDS) test.

# Chapter 4

# Establishing a live-cell super-resolution Traction Force Microscopy

In this chapter, I introduce the well-established TFM methodology and present three novel approaches we developed using super-resolution SIM microscopy to increase the temporal and spatial sensitivity of mechanical force measurements, crucial for immune cell mechanobiology studies of small- and fast-scale force production. First, I introduce an overview of the mathematical background of TFM and its mathematical challenge overcome by Fourier Transform Traction Cytometry (FTTC) and Regularisation. Next, I present the two most common techniques for displacement extraction, Single Particle Tracking (SPT) and PIV, showing their advantages and disadvantages. Finally, I discuss the limitations of previous TFM modalities and show how they can be improved using SIM. The novel force sensing technologies we developed combining TFM with SIM are called 2D TIRF-SIM-TFM, Three-dimensional SIM Traction Force Microscopy (3D SIM-TFM) and aTFM. These techniques can be straightforwardly implemented on a single SIM optical set-up, offering a powerful platform to provide new insights into the

physiological force generation in a wide range of biological studies. For each of the techniques, theoretical and experimental validations are shown with different cell types.

This work is the result of three published manuscripts (see Discussion, DPhil publication section 6.3):

- 2D TIRF-SIM-TFM: I carried out the simulation, experiments and data analysis.
- 3D SIM-TFM: I contributed to the biological experiments. Data analysis and simulations are from Dr. Huw Colin-York and Dr. Yousef Javanmardi. Set-up was built by Dr. Di Li and Dr. Kseniya Korobchevskaya.
- aTFM: I contributed to the biological experiments. Data analysis and simulations are from Dr. Huw Colin-York. Set-up was built by Dr. Di Li.

## 4.1 Traction Force Microscopy

TFM, pioneered by Harris, Wild, and Stopak in 1980 [148], is one of the most commonly applied force probing methodologies [149, 150, 99], primarily due to its adaptability in modelling biological and mechanical properties, ease of implementation, and reliance on widely-available materials and fluorescence microscopy [151]. In a TFM experiment, cells are plated onto the topmost layer of a homogeneous, isotropic, linearly elastic and optically transparent gel substrate, deposited on a glass coverslip [151, 152]. The molecular properties of the gel surface and its elastic properties can be tuned to mimic the rigidity and surface protein distribution of single cells and tissues [153, 154]. The most commonly used elastic substrates are hydrogels and elastomers, such as PAA and PDMS respectively, whose stiffness can be tuned and, in the case of PDMS, also their refractive index allowing total internal reflection TIRF on top of the substrate [155, 135, 156]. During cell-to-gel interaction, the cell transfers mechanical forces to the gel causing gel deformation. To

extract the mechanical force loaded by the cell, the gel deformation is imaged over time and tracked with respect to its relaxed state using tracking algorithms [155]. The information of the relaxed state is crucial to reconstruct the proper direction of gel deformation. Currently, two different approaches called reference-free and reference based methods are available in the TFM literature to image the relaxed state.

### 4.1.1 Reference-free TFM method

In a reference-free TFM method the top surface of the elastic gel is patterned with a regular grid as a reference for gel deformations. This lifts of the requirement for a reference image to extract the gel deformation over time. The gel patterning is made via a number of strategies, such as two-photon laser scanning lithography or deposition of a structured pattern of quantum dot inks on the gel surface [157, 158, 105, 159]. Once the cell is allowed to interact with the top surface of the gel, both cell dynamics and gel displacement is imaged over time using fluorescence microscopy.

### 4.1.2 Reference based TFM method

In a reference based TFM method, it is crucial to acquire one single reference image of the gel in its relaxed position, either before cell deposition or after cell detachment. To track the gel deformation, in a reference based TFM method, the top surface of the elastic gel is coated with randomly distributed fluorescent marker beads. Once placed on top of the gel, the cell interacts with the elastic substrate generating mechanical forces, which displace the gel, and consequently the fluorescent marker beads. By using optical fluorescence microscopy it is possible to record a series of images of the beads displacement underneath the cell over time. Knowing the materials properties of the elastic substrate, and using a theoretical model of the gel, both the magnitude and direction of the cellular

mechanical forces can be calculated from the spatial displacements compared to the initial or last bead image acquired [149].

Despite the practical advantages of the reference-free methods, it requires specialist equipment and their lateral spatial resolution is limited by the printing technique. On the contrary, the reference based TFM method, allows increased spatial resolution by coating the top surface of the gel with randomly distributed sub-diffraction sized fluorescent marker beads. In this work, we will use the reference based TFM method.

## 4.2 Theory behind Traction Force Microscopy

### 4.2.1 Fourier Transform Traction Cytometry

As mentioned previously, mechanical force can be extracted by tracking the deformation of fluorescent marker beads on top of the gel surface, and measuring the lateral displacement of each bead over time. The recovery of the stress field is a mathematical challenge which solution is based on a series of assumptions and general theorems [160–162]. The main assumption that has to be made to recover the stress filed is that the elastic substrate is considered a planar gel with infinite dimensions in the three (x,y,z) directions, defined as elastic isotropic half-space. Under this assumption, in the 19th Century Boussinesq *et al.* calculated the solution for the stress field recovery [162]. However, experientially, the gel has a finite thickness and dimensions, and it is placed on top of a glass coverslip. To maintain the half-space assumption, the gel must be sufficiently thick such that any force applied to the top of the gel surface is not altered by the rigidity of the glass coverslip. In practice, this restricts the gel to be no thinner than 20 μm - 30 μm and all displacements must be kept below 1 μm [160]. Another critical assumption is that the force normal to the gel surface are considered negligible [160]. Giving these two assumptions, the displacement field, $\mathbf{u}(\mathbf{x})$ can be extracted by imaging the fluorescent markers before and

after an applied force. The displacement field $\mathbf{x}$ is a two-dimensional vector along $x_1$ and $x_2$ directions and it is linked to the traction field ($\mathbf{T}$), defined as the stress e.g. the local force per unit area imposed on the gel surface by an external object such as a cell, trough the Green's function tensor [162], $\mathbb{G}$, as shown below:

$$\mathbf{u}(\mathbf{x}) = (\mathbb{G} * \mathbf{T})(\mathbf{x}) \tag{4.1}$$

$$\mathbb{G}(\mathbf{x}) = \frac{1+\nu}{\pi E}\frac{1}{|\mathbf{x}|^3}\begin{pmatrix} (1-\nu)|\mathbf{x}|^2 + \nu {x_1}^2 & \nu x_1 x_2 \\ \nu x_1 x_2 & (1-\nu)|\mathbf{x}|^2 + \nu {x_2}^2 \end{pmatrix} \tag{4.2}$$

where,

$$|\mathbf{x}| = \sqrt{{x_1}^2 + {x_2}^2} \tag{4.3}$$

By recording an image of fluorescent markers before and after an applied force, and by knowing the material properties of the elastic substrate both the displacement field and the Green's function can be obtained. Specifically, the materials properties are the Young's modulus (E), defined also as the stiffness of the material, and the Poisson ratio ($\nu$), that measures the deformation of the elastic substrate perpendicular to the direction of the force applied. To extract the traction field, the inversion theorem has to be applied to the equation 4.1. However, the Green's function is not diagonal in the $\mathbf{x}$ space, requiring the use of large matrices when inverted and consequently generating a computationally expensive solution. Butler *et al.* [161] overcame this problem suggesting to work in the Fourier Space, represented by the spatial wave vector $\mathbf{k}$. There, the Boussinesq's solution is diagonal and the inverse problem solution is less computationally expensive [161]. This method is called FTTC. In addition, according to the convolution theorem, the Fourier transform of a convolution is a product of the Fourier transforms. Applying a Fourier transform (denoted by the tilde symbol), the traction field can be

then easily extracted by multiplying the inverted Green's function with the displacement field:

$$\tilde{\mathbf{u}}(\mathbf{k}) = \widetilde{\mathbb{G}}(\mathbf{k})\widetilde{\mathbf{T}}(\mathbf{k}) \tag{4.4}$$

$$\widetilde{\mathbf{T}}(\mathbf{k}) = \widetilde{\mathbb{G}}(\mathbf{k})^{-1}\tilde{\mathbf{u}}(\mathbf{k}) \tag{4.5}$$

However, for high frequency values of the displacement field, the equation 4.5 results in a divergent stress field. Indeed, the displacement field, which is measured experimentally via optical microscopy techniques, is likely to contain high frequency noise resulting from the imaging recording step of the fluorescent markers. This is a typical ill-posed problem where the solution is sensitive to noise from the initial condition [163]. The ill-posed condition of the inverse problem can be solved with a technique called regularisation [164–166].

### 4.2.2 Regularisation

To solve the stress field equation, the inverse problem has to be applied. However, if the displacement field contains experimental noise, the traction field will result in a divergent solution. This is a classical limitation of the inverse problem and can be solved introducing a regularisation term within the minimisation condition to stabilise and smooth the solution. The most common choice is the zero-order Tikhonov regularisation [164], where the Lagrange parameter $\lambda$ is used in the trade-off curve to determine the optimal agreement between the given data (first term) and the regularisation (second term).

$$\min\{||\widetilde{\mathbb{G}}\widetilde{\mathbf{T}}_\lambda - \tilde{\mathbf{u}}||^2 + \lambda^2||\widetilde{\mathbf{T}}_\lambda||^2\} \tag{4.6}$$

The minimisation equation can be solved with respect to the stress field for a large range of $\lambda$ values. The goal is to find the optimal regularisation term, since $\lambda$ values that are too small will overestimate the noise within the stress field, while values that are too large will over-smooth the solution. To find a balance between noise and smoothing, a curve representing the solution norm, $\widetilde{\mathbf{T}}_\lambda$ as a function of the residual norm, $||\widetilde{\mathbb{G}}\widetilde{\mathbf{T}}_\lambda - \widetilde{\mathbf{u}}||$, is plotted for different $\lambda$ values. This curve is known as L-curve, given its common L-shape [167]. The optimal parametrisation value is not always straightforward to find, but usually resides where the L-curve curvature has its highest degree.

### 4.2.3 Displacement field extraction: SPT and PIV

TFM sensitivity crucially depends on analysis strategy adopted to extract the displacement information of the fluorescent marker beads [155]. Extraction of the fluorescent marker beads displacement is typically achieved through the SPT algorithm or techniques based on correlation of fluorescent images, such as PIV [155].

**Single Particle Tracking** The SPT approach relies on two steps: (i) the localisation of each individual fluorescent marker bead in space and (ii) the link of the individual localisations at different time points for a unique fluorescent marker bead, to generate single bead trajectories. The quality of the tracking thereby depends on the localisation of each of the beads in space and time, thus for any given bead the displacement information can be resolved with high confidence. In this work, the Trackpy [138] algorithm package from Python 3.7 is adopted. The main advantage of SPT is that both 2D and 3D fluorescent marker beads displacements can be tracked, while the main disadvantage is SPT relies on the spatial resolution of the applied microscopy modality because spatially under-sampled distributions of fluorescent beads lead to overlapping beads and thus erroneous localisation.

**Particle Image Velocimetry** PIV is the most commonly used correlative technique [168, 169]. In a PIV analysis, the fluorescent image is divided into sub-regions, called PIV windows [170]. Each sub-region is then compared with the corresponding one at the next time-point using spatial correlation to assess the relative spatial shift of their fluorescence content. Specifically, the relative displacement between the image pair is established by extracting the location of the minimum quadratic difference (MQD) for each PIV window,

$$\sum_{i=1}^{N}\sum_{j=1}^{N}|W_1(t_0) - W_2(t_0 + \Delta t)| \tag{4.7}$$

where i,j denote the (i,j)th pixel of the sub-region which is of size N, and $W_1$ and $W_2$ are the pixel intensities of the two PIV windows at time $t_0$ and $t_0 + \Delta t$ respectively. For each PIV window, one displacement vector is assigned, producing a displacement map across the whole FOV. Each neighbouring PIV window can be overlapped (usually by 25% or 50% of its width), ensuring robust PIV displacement analysis for both simulated fluorescent image pairs and experimental data.

The quality of PIV depends on the size of the chosen PIV window, and care must be taken that a sufficient number of beads is present within each of those windows. The main disadvantage of this technique compared to SPT is that only 2D fluorescent marker beads can be tracked, while the main advantage is that it is robust against overlapping beads, allowing a greater flexibility in the choice of experimental bead density.

## 4.3 Overview of force quantification in cells

Mechanical forces are involved in and regulate many biological phenomena, often evolving rapidly from seconds to sub-seconds time scale and generating small force magnitude

from small nanoscale to micron-scale. Some examples of small and rapid force generation are can be observed at the level of the 2D cell-surface of cancer cells during adhesion or detachment, cell migration and immune cell activation [125, 105, 102, 103, 171, 104, 172]. For these reasons, there is a continuing demand to develop a sensitive TFM modality for quantifying planar forces in cells on the sub-second time-scale and sub-micron spatial-scale. Despite its importance and proven biological significance, quantifying force production in cells via TFM remains challenging because it relies on the temporal and spatial resolution of the optical microscopy modality used to image the gel displacement. In particular, the sensitivity and biocompatibility of TFM depend on the trade-off between spatial resolution, temporal resolution, and acquisition duration [173–175]. Despite the technical limitations, there is an urgent demand from the biological context to investigate biological questions involving cellular force production with sub-micron length-scales and sub-second time-scales [125].

As mentioned in the Background chapter, force generation during immune cell response is crucial for their activation and function, playing a role in antigen recognition and $Ca^{2+}$ signalling [69, 176, 67]. In addition, rapid force generation is vital for cell migration, for example, in the case of wound-healing processes [177–179]. Consequently, there is a pressing need to improve the sensitivity and biocompatibility of TFM.

## 4.4 TFM sensitivity

The sensitivity of TFM strictly depends by the spatial and temporal resolution of the microscopy modality. Ideally, the spatial and temporal frequency for force probing should be at the exact length- and time-scale demanded by the biology. The spatial sensitivity of TFM can be defined as a combination of the precision in recovering a given force applied and the accuracy in mapping the force with respect to one or more cellular structures. For that, very high density of infinitesimally small beads on top of the gel

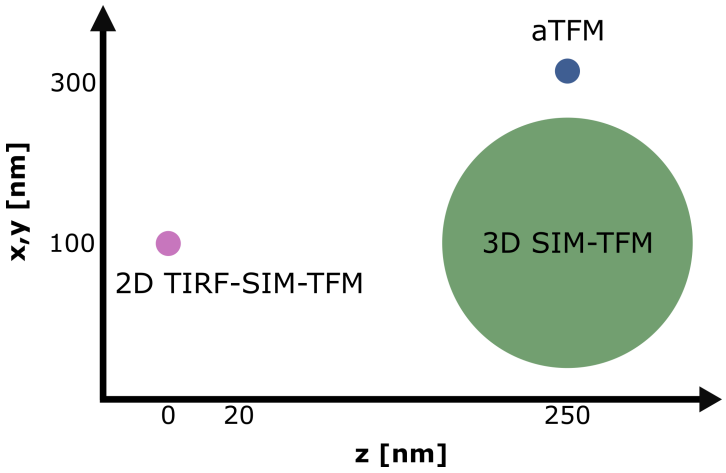



Fig. 4.1 Schematic of the three novel SIM-TFM technologies presented in this work. The schematic shows the imaging resolution in lateral (x,y) and axial (z) directions represented in nm, together with the temporal resolution represented by the different size of the circles (large 0.1-1 fps and small 1-10 fps), for the 2D TIRF-SIM-TFM (magenta), aTFM (blue), and 3D SIM-TFM (green).

would be ideal. Unfortunately, the spatial sensitivity of TFM is constrained by the diffraction limit of a fluorescence microscope and the ability of recognising two objects, in this specific case two fluorescent marker beads, as distinct. The diffraction limit of a microscope imposes an upper limit on the bead densities, beyond which it would be impossible to distinguish beads one from the other and therefore track them, profoundly constraining the spatial resolution of TFM. To partially address this constraint, Colin-York *et al.* have previously combined the super-resolution Stimulated Emission Depletion (STED) microscopy and TFM [102]. STED Traction Force Microscopy (STED-TFM) offers up to 5-fold improvement in spatial sampling, extending the sensitivity of TFM. Nonetheless, because STED is a scanning technique whereby the excitation laser is scanned over the entire FOV and it relies on the temporal averaging at each pixel, the acquisition speed is limited, restricting the temporal sensitivity of planar force probing with STED-TFM to multiple sec per single frame image (see Table 1). On top of that, in STED-TFM the biocompatibility is reduced, because the technique relies on a high laser intensity for fluorescence depletion. A different approach was introduced

Table 4.1 *Note, the primary speed limitation of TIRF, 2D TIRF-SIM-TFM and aTFM is imposed by the camera exposure time. **Note, the value represents the axial localisation uncertainty in aTFM. ***Note, the value indicates the frame rate for a FOV of about 10 $\mu m^2$. Table adapted from Barbieri *et al.* [180].

| TFM methods | Lateral Imaging Spatial Resolution (nm) | Axial Imaging Spatial Resolution (nm) | Temporal Resolution (frames per sec) | Illumination power ($kW/cm^2$) | TFM sensitivity (bead/$\mu m^2$) | 2D Force Estimation | 3D Force Estimation |
|---|---|---|---|---|---|---|---|
| 2D TIRF-SIM-TFM | < 100 | n/a | 1-10 | 0.02-0.1 | 15-20 | v | x |
| aTFM | 200-300 | 20** | 1-10 (2 μm z range) | 0.02-0.1 | 0.3 | v | v |
| 3D-SIM-TFM [125] | < 100 | 250 | 0.1-1 (2 μm z range) | 0.02-0.1 | 1 | v | v |
| 2D-STED-TFM [151] | < 100 | 300 | 0.05-0.1*** | $1\text{-}10^5$ | 2.2-5 | v | v |
| TIRF | 300 | n/a | 1 | 0.02-0.1 | 1 | v | v |
| FBSR [103] | 200 | n/a | 0.05 | Not reported | Not reported | v | x |
| High-resolution TFM [149] | 200-300 | 600-800 | 0.2*** | Not reported | Not reported | v | x |
| Confocal | 200-300 | 600-800 | 0.1-1 | 0.1-10 | 1 | v | v |

by Stubb *et al.*, where they addressed the enhancing of the spatial resolution of TFM by imaging fluorescent marker beads on standard confocal and wide-field microscopes and using fluorescence fluctuation analysis on fluorescent bead images [103]. Thanks to fluctuation-based analysis, they achieved a lateral spatial-resolution of 200 nm but at the expense of a loss in temporal resolution to multiple sec (seconds) per frame (see Table 4.1).

In this work, to address the current limitation of TFM, we established three novel live-cell super-resolution methodologies by combining SIM with TFM [125, 180, 134](See

Fig. 4.1). To enable sensitive physiological 2D force probing in cells, we first combined TFM with fast super-resolution high NA TIRF-SIM, called 2D TIRF-SIM-TFM, enhancing both the spatial and temporal resolution of force probing by increasing the lateral imaging resolution to 100 nm and the temporal resolution to 1-10 fps. Secondly, in order to measure also mechanical force in the axial direction we implemented 3D SIM-TFM, extending the imaging resolution to 100 nm lateral and 300 nm axial [125], while maintaining a temporal resolution comparable to STED-TFM. Finally, to further improve the temporal and axial resolution during 3D mechanical force acquisition, we combined TFM with astigmatic imaging, aTFM, achieving imaging resolution of 200 nm lateral and an axial localisation uncertainty of 20 nm, while maintaining a temporal resolution of 2D TIRF-SIM-TFM [134].

## 4.5 2D TIRF-SIM-TFM

Live-cell super-resolution TIRF-SIM is a technique recently developed to extend the spatial and temporal force probing sensitivity with a minimal invasiveness to the biology [29, 132]. TIRF [181, 182] illumination consists of an evanescent field to excited the specimen region up to around 200 nm depth from the surface of a substrate, and can be achieved if (i) the excitation light travels from a substrate with higher refractive index (usually 1.49 for glass) to a substrate with a lower one (1.33 for aqueous medium) and (ii) if the incident angle is greater than a critical angle. The TIRF illumination optimises the axial spatial resolution and reduces the fluorescence background. Because the TIRF technique allows imaging at the top surface of the glass coverslips, historically the TIRF approach has been excluded as a suitable one for imaging mechanical force. Recently, thanks to the work of Gutierrez *et al.* [135], by using an high refractive index silicone gel that matches the glass coverslip one, the TIRF excitation can be moved to the upper gel layer allowing TIRF-SIM illumination at the gel to media interface.

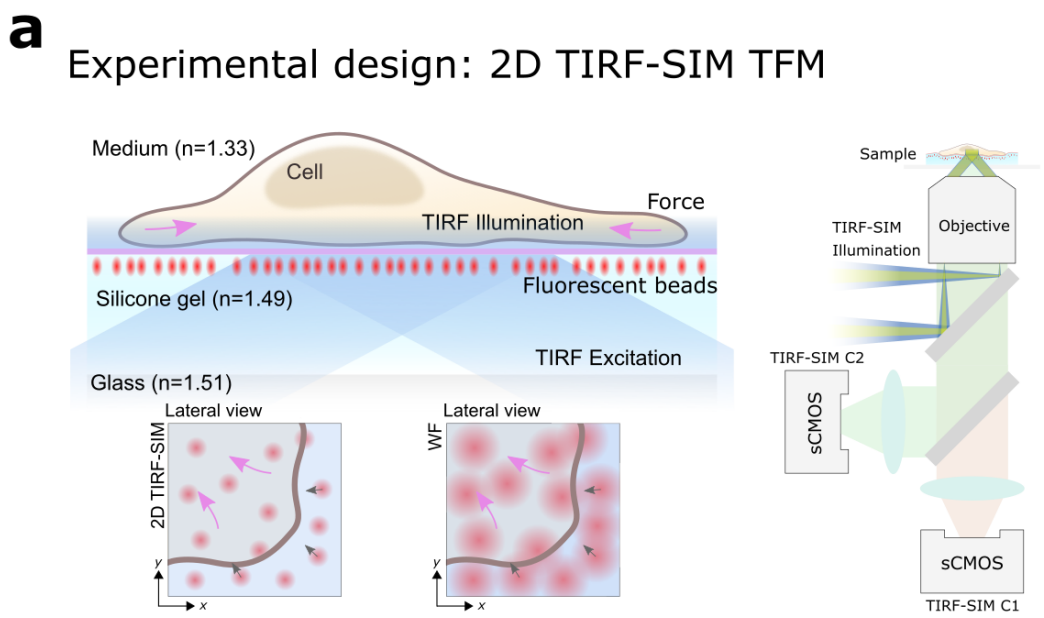



Fig. 4.2 **(a)** Experimental design of the 2D TIRF-SIM-TFM methodology. Left - TIRF excitation light (488 nm or 560 nm) at the interface between the gel and the medium excites fluorescent beads and basal plane of the cell. Right – Optical path of the TIRF-SIM platform, allowing detection of the fluorescent bead channel and the cell on two dedicated sCMOS cameras.

We started with the development of this novel 2D TIRF-SIM-TFM methodology combining TFM with an existing custom-built TIRF-SIM platform [125, 135] (see Materials and methods). By producing silicone gels with a refractive index of 1.49 [135], closely matching glass, and applying the appropriate critical angle, we could translate the TIRF field to the topmost layer of the silicone gel sample. This new set-up allows simultaneous TIRF-SIM illumination in both the fluorescent cell and bead channel 4.2 (see Materials and methods). The final achievement is an isotropic point spread function (PSF; $< 100 \pm 20$ nm laterally and axially), maximising contrast in the fluorescent cell channel and minimising background noise.

Once the technology was in place, we focused on the best analysis method for force reconstruction using the TFM methodology. Because one of our aim was to increase the spatial sensitivity of force probing, there was a need to increase the bead density on top of the gel surface. Aware of the increased bead density, we decided to take advantage of the TIRF-SIM spatial resolution using the PIV analysis approach over the SPT.

### 4.5.1 Improving TFM sensitivity using 2D TIRF-SIM

Before starting with live-cell experiments, we sought to understand through computer-simulations how the sensitivity of 2D TIRF-SIM-TFM depends on the resolution of the optical microscope, the density of the fluorescence marker beads, and the PIV analysis window size. The goal of TFM is to recover mechanical force generated by cellular structures, with high spatial and temporal sensitivity. Let's imagine to measure the force applied by an adherent cell to an elastic gel. What we want is to be able to capture the range of mechanical force generated by the cell, as well as linking that force to the different cellular structures, such as focal adhesions. If the bead distribution is sparse, we might miss either some mechanical force values, or the force underneath a focal adhesion structure or both. The same problem can be translated for the temporal resolution during

TFM acquisition. If the mechanical force is generated at a time scale faster than the TFM acquisition, the beads displacement and therefore the force will not be registered. The way to overcome to this limitation is to increase the bead density and the acquisition speed.

For that, we first conducted computer-simulations to determine the dynamic range of the sensitivity improvement of TFM comparing TIRF-SIM image acquisition and the most commonly used optical microscopy technique that is WF. Specifically, we built a computer-simulation pipeline comprising of 4 steps: (i) the simulation of the traction field, (ii) the calculation of the corresponding GT displacement field, (iii) the simulation of the respective displacement of the simulated fluorescent image pairs before and after the applied traction as observed by TIRF-SIM and WF, and lastly, (iv) the determination of the recovered displacement field for a given PIV window size (Fig. 4.3). The sensitivity of the final recovered displacement fields when using TIRF-SIM or WF were then quantified and interpreted in two additional analysis steps, by comparing them to the GT via two independent metrics outlined. We designed the computer-simulations to mimic 2D TFM measurements under a well-defined shear force (in units of stress Pascal, Pa), ranging from 250 Pa to 10 kPa. For that, we first simulated a stress field with well-defined squared shape to a square domain of size size 5 x 5 $\mu m^2$ with properties of an elastic gel. Specifically, the domain satisfies the linear elasticity model for gels, with Young's modulus of 10 kPa and a Poisson ratio 0.5 (Step 1, Fig. 4.3a). On the domain, randomly distributed fluorescent marker beads were simulated. At this stage, the bead dimension called PSF is dimensionless and equals to 1 pixel. Two sampling densities were selected: a sparse one of 12 beads per $\mu m^2$ and a dense one of 82 beads per $\mu m^2$ (see Materials and methods). The simulated domain size was chosen to minimise both the computational cost for displacement recovery and to avoid boundary effects due to the stress field applied to a finite domain size. The stress field simulated was a linear and

constant distribution with either a single square-shaped stress zone of fixed size 0.2 x 0.2 $\mu m^2$ or three co-linear square-shaped stress zones of fixed size 0.2 x 0.2 $\mu m^2$ equally separated by a distance L = 0.2 $\mu m^2$ along the x-axis. The reason behind the single and triple square-shaped stress zones was to test the sensitivity of TFM in recovering and distinguishing the displacement generated by one or multiple cellular structures (such as focal adhesions), over the different force and bead density conditions. Note, I will use both terms 'traction' and 'stress' while referring to the 2D force exerted by the cell over the gel interface.

Next, we calculated the corresponding GT displacement fields (Step 2, Fig. 4.3a). To do so, the FTTC was applied to the simulated stress field, and the GT displacement field calculated was subsampled according to the random position of the fluorescent marker beads within a pixel grid, where each pixel equals 30 nm. This was done for both the sparse and dense density case. Subsequently, using the displacement values at the location of each one pixel-size bead, the fluorescent pairs of images with the beads distribution before and after the applied stress were generated. At this stage, a FWHM of 110 nm for TIRF-SIM and 270 nm for WF was associated to each of the fluorescent marker beads simulated, accordingly to the lateral resolution of experimental data (see Materials and methods, Step 3, Fig. 4.3a).

Finally, to recover the displacement from the fluorescent image pairs, the PIV analysis algorithm was then applied, testing for a range of PIV window sizes for the single and triple square-shaped simulation stress conditions, for both TIRF-SIM and WF case (Step 4, Fig. 4.3a).

### 4.5.2 Singular value decomposition analysis

Once obtained the recovered displacement fields for TIRF-SIM and WF we quantitatively compared their quality to the GT displacement fields. For that, we used a method for

measuring image quality based on SVD analysis [136]. The SVD quality metric computes the distance between the singular values of the GT displacement field and the singular values of the recovered displacement field (Step 5, Fig. 4.3a) (see Materials and methods). The SVD quality metric, after normalisation, has a range of values going form 0 to 1, where 0 indicates bad estimation of recovered displacement compared to the GT and the maximum value of 1 indicates a good estimation.

As mentioned before, we wanted to investigate the TFM sensitivity, by exploring the relationship between the image spatial resolution, the density of fiducial marker beads, and the PIV window size. Regarding the bead density, we selected a sparse 12 beads per $\mu m^2$ (comparable to experimental fluorescence bead data) and a dense 82 beads per $\mu m^2$ (Fig. 4.3). The 82 beads per $\mu m^2$ density comes from a mathematical estimation to have, within an area of 1 $\mu$m size, all the beads next to each others not overlapping, given a bead PSF of 110 nm size obtained using TIRF-SIM modality.

This result comes from a simple calculation:

$$\frac{Area_{region}}{Area_{PSF}} = 82 \tag{4.8}$$

where the $\text{Area}_{region} = 10^6$ nm$^2$ and the $\text{Area}_{PSF} = 1{,}21 \times 10^4$ nm$^2$ . The computer-simulations were run for a range of PIV window sizes scaling from a minimum of 120 nm to a maximum of 960 nm (corresponding to 4 px and 32 px respectively), exploring the influence of the PIV window size in resolving a given displacement field. Importantly, given a bead density the number of beads within a PIV window decreases with the size of that window. However, for the PIV image correlation analysis to robustly work, there mush be at least two beads within a PIV window. Therefore, given a bead density, we decided to assign a cut-off value for all the cases where the number of beads within the PIV window was equals to or less than one, bringing to a failure in the PIV analysis (see plot in Fig. 4.4).

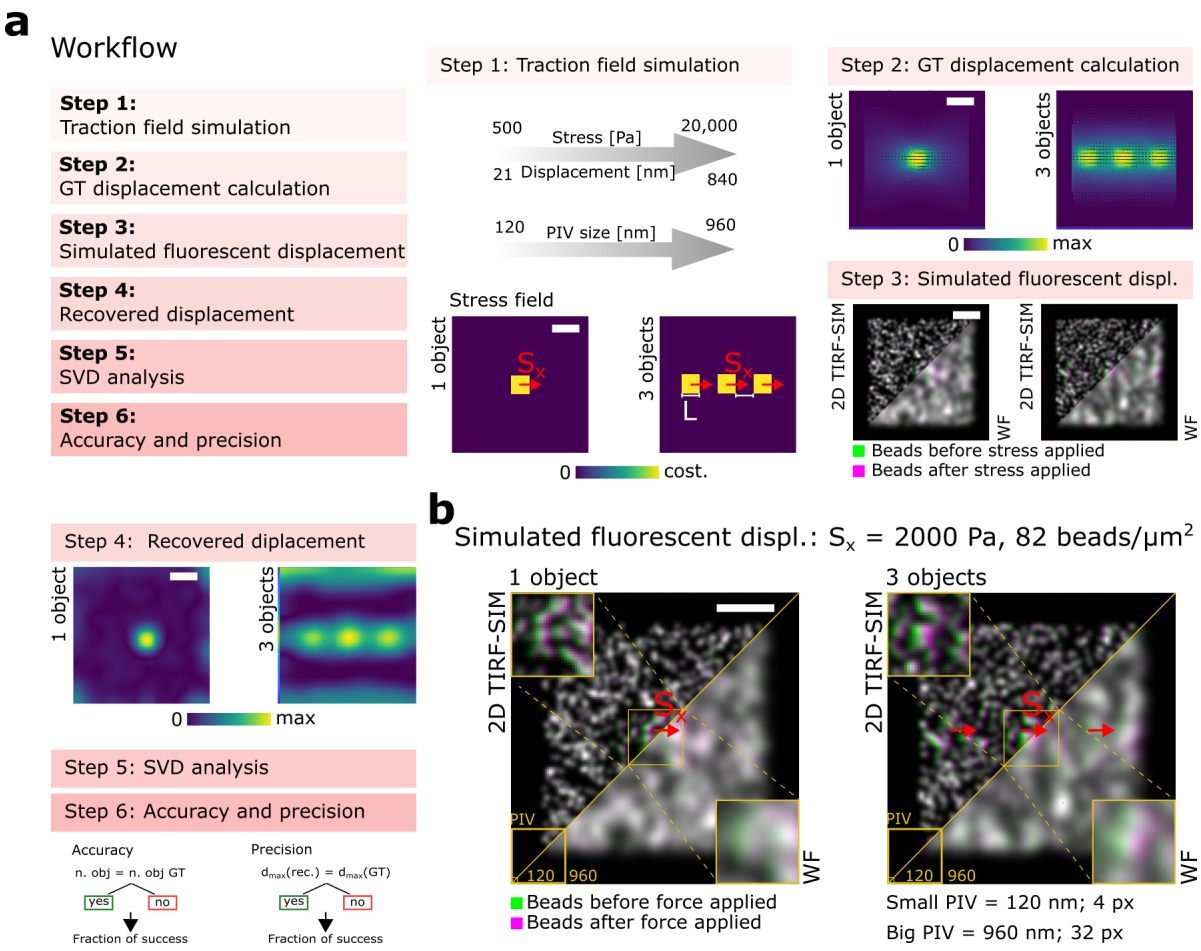



Fig. 4.3 **(a)** Graphical diagram outlining the 6 steps simulation pipeline quantifying the effect of image resolution, bead density, and PIV window size on the quality of displacement estimation compared to the GT. Scale bar is 1 µm. **(b)** Example of simulated fluorescent displacement image pairs for both the single- and triple square-shaped stress zones with high bead density of 82 beads/µm$^2$. The simulated fluorescent images before (green) and after (magenta) a 1 kPa lateral stress in the x direction are superimposed. Image pairs are shown in 2D TIRF-SIM and WF. A zoom-in of the central part of the image highlights the beads shift. The smaller (120 nm or 4 px) and larger (960 nm or 32 px) PIV window sizes selected are displayed on the bottom left of each image pairs. Scale bar is 1 µm.

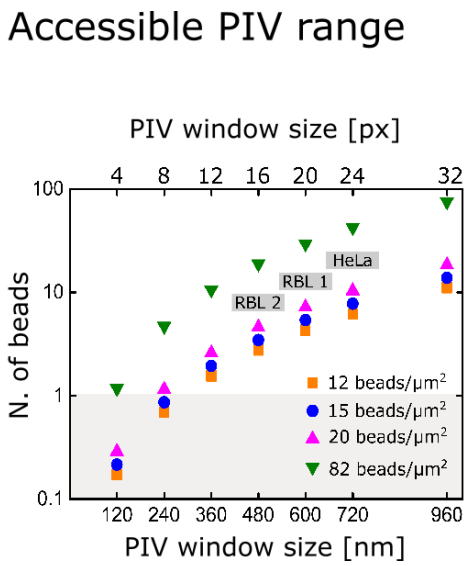



Fig. 4.4 Plot outlining the relationship between the PIV windows size and the expected number of beads within a given PIV window at different beads densities. The grey boxes indicate the different relationships for the cells analysed in Section4.5.5 and 4.5.6.

From the SVD quality metric we could immediately appreciate how the PIV approach has a strikingly better performance for the high 82 beads per $\mu m^2$ density coated gels imaged via 2D TIRF-SIM-TFM compared to WF for triple square-shaped stress zones (see Fig. 4.6). To facilitate the analysis, we normalised both the SVD quality metrics to the maximum SVD value obtain using the TIRF-SIM method (see numbers printed on top of the heat-maps Fig.4.5a), and we colour-scaled each column so that the minimum and maximum values within that column are highlighted (see colour bar in Fig.4.5a). Observing the SVD quality metric presented as heat-maps (see Fig. 4.5a), it is evident that the combination of a dense bead density with extended spatial resolution leads to an higher TFM sensitivity in recovering small displacement using small PIV window sizes. Specifically, small displacements acquired with the TIRF-SIM method and recovered using small PIV window sizes have a better agreement to the GT displacements (yellow regions), compared those recovered with WF method (see red arrow on the left, Fig. 4.5a), in agreement with previous work [102, 183]. As predicted, the computer-simulations in the TIRF-SIM modality showed better agreement with the GT with a maximum SVD

value of 1, while for the WF modality the maximum SVD value is 0.8. This can be appreciated from the plot showing the difference between the TIRF-SIM SVD quality metrics and WF SVD quality metric (Fig. 4.5b). Notably, the SVD quality metric for the computer-simulations with the sparse 12 beads per $\mu m^2$ in the case of TIRF-SIM and WF were comparable (Fig. 4.6). dashed line representing the cut-off limit of one bead per PIV window is shown in the SVD quality metric heat-maps, defined as Spatial Resolution Limit (SRL). For the high density beads case, this limit is dictated by the PSF size corresponding to the modality used. In particular, for the case of TIRF-SIM the limit corresponds to a PIV window of 120 nm size, given a bead PSF of 110 nm, while for the WF case the PIV window size limit is 240 nm, given a PSF of 270 nm (dashed line, Fig. 4.5a and Fig. 4.6a). The SVD quality metric revealed the PIV analysis fails in three cases. The first is for displacements recovered when there was less than a bead per PIV window, as already mentioned. The second is when the displacements are larger than the PIV window size selected (see the oblique solid line in Fig. 4.5a and Fig. 4.6a). Lastly, for a triple square-shaped stress zones, the SVD quality metric fails when the length-scale of the maximum displacement is equal to or bigger than the separation distance between the respective squared-shape stress fields ($d > L$) (dotted line, Fig. 4.5a and Fig. 4.6a). This reveals a fundamental limitation of TFM, where co-linear stresses can be only solved if their separation is larger than the underlying displacements. Crucially, by extracting the maximum of the SVD quality metric for each simulated stress field condition in both TIRF-SIM and WF, we could extract an optimal PIV window size and create a guide for the subsequent analysis of experimental data (Fig. 4.5c and Fig. 4.6c). Note, the SVD quality metrics for the single square-shaped stress field are not shown separately due to reasons of limited added information value.

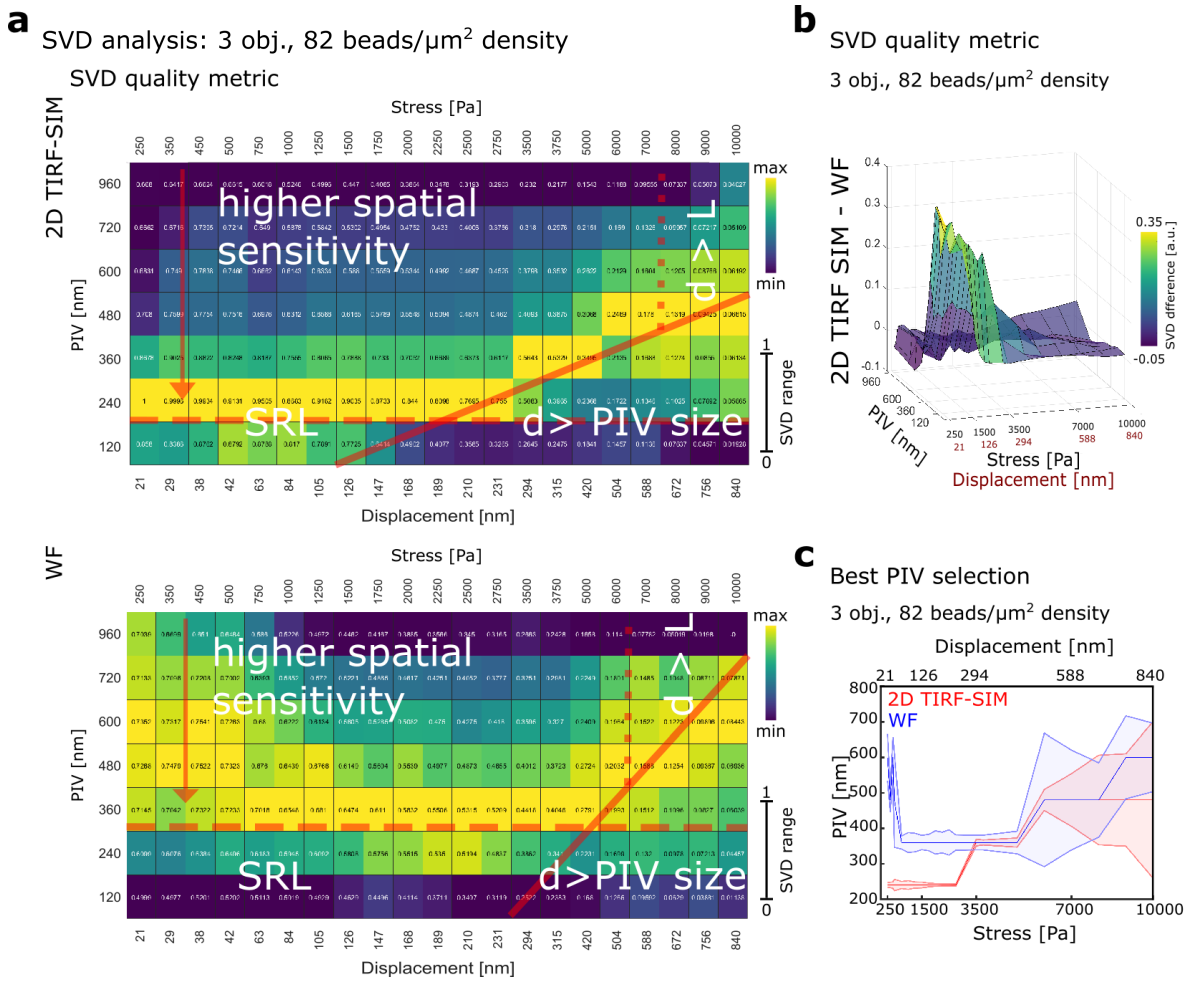



Fig. 4.5 **(a)** Heat-maps showing the quality of the displacement estimation compared to the GT for a range of PIV windows size and displacement magnitudes using the SVD quality metric for both TIRF-SIM (upper) and WF (lower). Bead density equals to 82 beads/$\mu m^2$. The range of the SVD quality metric goes from 0 to 1 (TIRF-SIM) and 0 to 0.8 (WF), with the value 1 representing the best estimation quality of the displacement field. Columns are colour-scaled such that the maximum and minimum SVD values are underlined in each of them. SRL indicates the spatial resolution limit. **b** - SVD quality metric difference between TIRF-SIM and WF. Each condition is normalised to the maximum TIRF-SIM SVD quality metric, with a value close to 1 indicating improved displacement estimation.**(c)** Plot guiding the optimal PIV window size choice for a given displacement, based on the maximum SVD quality metric value for TIRF-SIM and WF. The error bars represent the average difference between the maximum SVD value and the two neighbouring values.

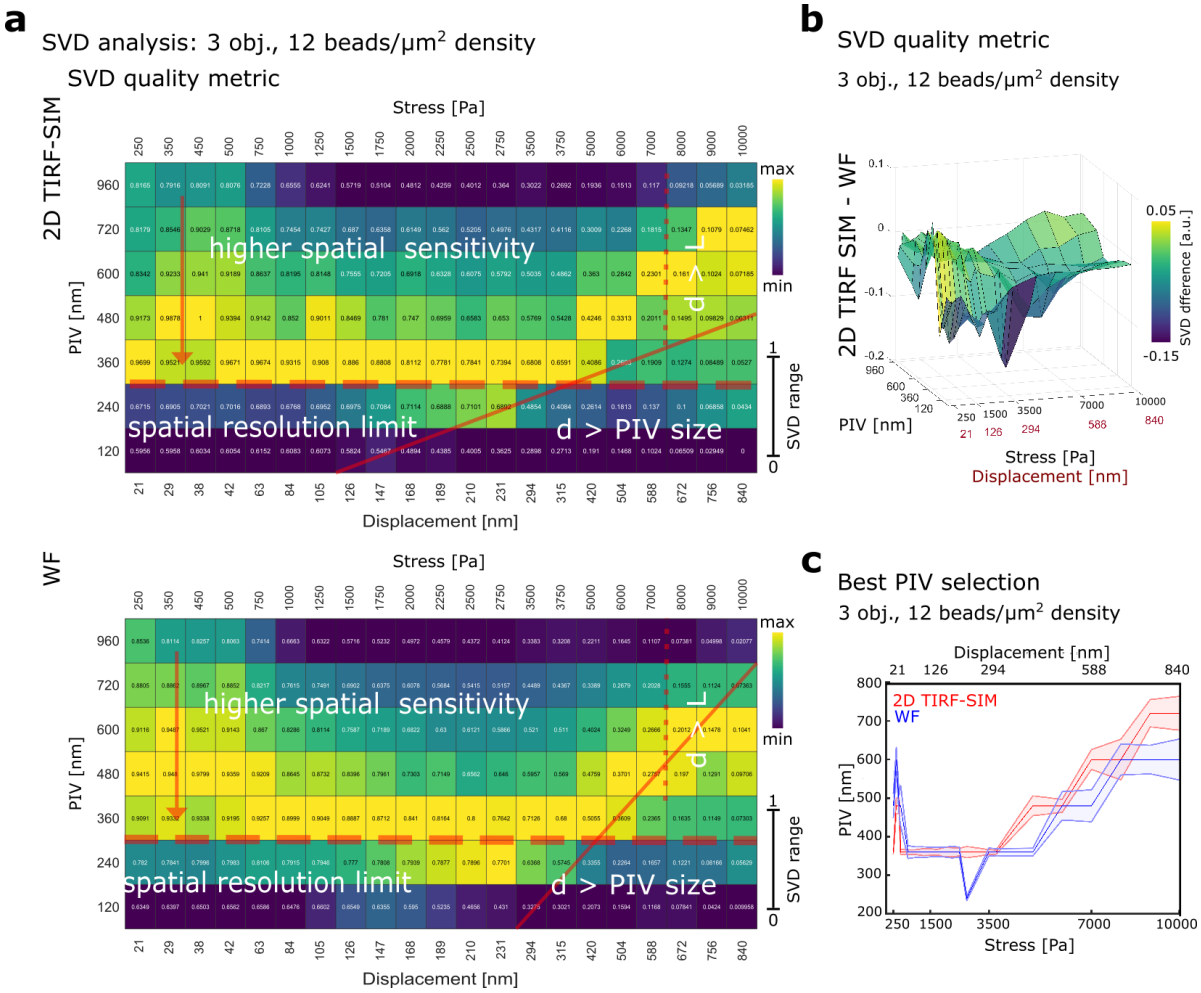



Fig. 4.6 **(a)** Heat-maps showing the quality of the displacement estimation compared to the GT for a range of PIV windows size and displacement magnitudes using the SVD quality metric for both TIRF-SIM (upper) and WF (lower). Bead density equals to 12 beads/$\mu m^2$. The range of the SVD quality metric goes from 0 to 1 (TIRF-SIM) and 0 to 0.8 (WF), with the value 1 representing the best estimation quality of the displacement field. Columns are colour-scaled such that the maximum and minimum SVD values are underlined in each of them. SRL indicates the spatial resolution limit. **b** - SVD quality metric difference between TIRF-SIM and WF. Each condition is normalised to the maximum TIRF-SIM SVD quality metric, with a value close to 1 indicating improved displacement estimation.**(c)** Plot guiding the optimal PIV window size choice for a given displacement, based on the maximum SVD quality metric value for TIRF-SIM and WF. The error bars represent the average difference between the maximum SVD value and the two neighbouring values.

### 4.5.3 Accuracy and precision scoring metrics

We further developed the analysis of the recovered displacement introducing two scoring metrics defined as accuracy and precision (Fig.4.7a-f). The SVD metric gives an overall quality estimation of the recovered displacement compared to GT. However, it does not show quantitatively why one condition is better than the other. Specifically, we were interested in matching the recovered displacement values with the GT ones and in being able to recover the underlying structure of the displacement. For that we defined a precision diagram that compares the maximum recovered displacement value with the maximum GT displacement (Fig.4.3) and an accuracy diagram, that measures and compares the number of recovered traction objects compared to the GT case (Fig.4.3). The accuracy diagram (see Fig. 4.7) shows the fraction among 100 computer-simulations repeats successfully recovering the number of traction objects in the GT. The precision diagram, instead, displays the fraction among 100 computer-simulations correctly recovering the maximum displacement compared to the GT maximum displacement value (see Materials and methods). These two new quantitative scoring metrics revealed that while both 2D TIRF-SIM-TFM and WF-TFM could robustly recover the maximum displacement values (see precision diagram, Fig.4.7b), the triple square-shaped stress zone in the case of small displacements was only well recovered using 2D TIRF-SIM-TFM and small PIV window size (see accuracy diagram, Fig.4.7c). The failure in the accuracy diagram for the TIRF-SIM condition in the stress range of 450 - 1000 Pa was due to the particular nature of the simulation designed. For stress fields in the range of 450 - 1000 Pa with the vector direction along the x-axis, the displacement of the three squared-shape objects appeared as an uniform displacement coming from one single squared object (Fig.4.7b,c). To verify this, we simulated the same stress field but with a vector pointing along the y axis (Fig. 4.7d), highlighting the influence of both the stress magnitude and

direction. Interestingly, the precision and accuracy diagrams for the sparse 12 beads/$\mu m^2$ density revealed a less accurate recovery of the GT (Fig. 4.7e,f).

Owing to the computer-simulations and the three metrics adopted for qualitative and quantitative analysis we could demonstrate the significance of increasing the fluorescent marker bead densities, spatial resolution, and an optimal PIV window choice in 2D TIRF-SIM-TFM measurements. Our SVD quality metrics provide a guide for finding the optimal parameters for image acquisition and analysis using the PIV method in TFM for a given stress field, bead density and spatial resolution.

### 4.5.4 2D TIRF-SIM-TFM: gel optimisation

Before investigating mechanical force generation in live-cells using 2D TIRF-SIM-TFM, it was necessary to optimise the silicone gel bulk structure, as well as its bead density.

As we discussed in the Theory section of TFM, the gel thickness cannot be less than 20 - 30 μm in order to satisfy the half-space assumption and to avoid any alteration in the mechanical force generated by the cell due to the rigid glass underneath the gel. Hence care must be taken in the experimental protocol for gel formation. The silicone gel layer is formed by spin-coating the gel on top of a glass coverslip [135]. The gel volume, the spin-coating speed and time are the three parameters that together define the gel thickness. In this study, the gel thickness was calibrated by fixing the gel volume, and tuning the speed and the time of the spin-coater (see Materials and methods). The optimal parameters selected to obtain a 20 μm thick gel layer were: 50 μl volume, 5000 RPM speed and 10 sec. These parameters are adopted in all the rest of this work.

Another crucial step during gel production is to produce an homogeneous gel bulk to allow TIRF-SIM illumination at the top surface of the silicone gel. The presence of any type of structures and obstacles, such as dust or bubbles, represent a problem for TIRF-SIM illumination, since they are all a source for light scattering. This problem

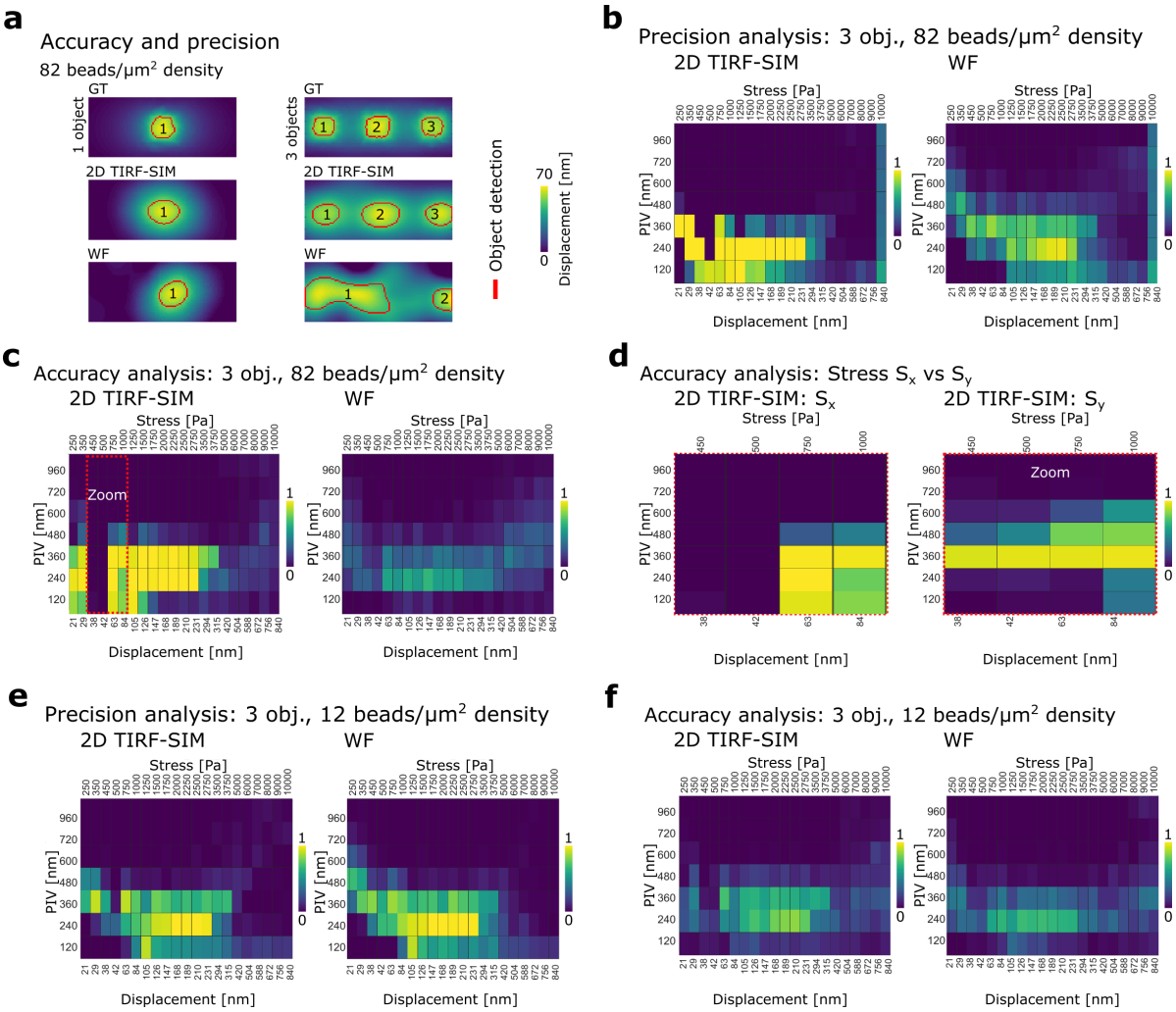



Fig. 4.7 **(a)** Example of the displacement field binarisation for extracting the accuracy and precision of 2D TIRF-SIM-TFM. Both the single and three co-linear positioned square-shaped stress zones are shown for the GT, 2D TIRF-SIM and WF modalities when a stress of 1 kPa is applied, and a PIV windows of 360 nm is used at a bead density of 82 beads/μm$^2$. The red line represents the contour of the binary image after being binarised. Scale bar is 1 μm. **(b)** Precision maps for 2D TIRF-SIM and WF for the case of three co-linear positioned square-shaped stress zones at a bead density of 82 beads/μm$^2$. The values show the fraction of success among 100 repeats. **(c)** Accuracy maps for 2D TIRF-SIM and WF for the case of three co-linear positioned square-shaped stress zones with 82 beads/μm$^2$ density. **(d)** Comparison of accuracy maps for the 2D TIRF-SIM case, when either an horizontal or vertical stress in the range between 450 to 1000 Pa is simulated for the case of three co-linear positioned square-shaped stress zones at a bead density of 82 beads/μm$^2$. **(e)** Heatmap of the precision diagram for the case of three co-linear positioned square-shaped stress zones at a bead density of 12 beads/μm$^2$ for both TIRF-SIM (left) and WF (right). The values show the fraction of success among 100 repeats. **(f)** Heatmap of corresponding accuracy diagrams for the case of three co-linear positioned square-shaped stress zones at a bead density of 12 beads/μm$^2$ for both TIRF-SIM (left) and WF (right).

was solved after finding the two sources of bubble formation: the mixing step of the silicone gel components, that creates bubbles, and the the glass coverslip surface, with its dusty surface. To eliminate these bubble sources, a degassing and vacuum steps for the gel, as well as the standard Piranha cleaning method for glass coverslips were added into the protocol (see Materials and methods). The silicone gel stiffness is defined by the ratio of the two 920A and 920B components mixed together [135] (see Materials and methods). To re-produce these values, the silicone gel samples were made following the ratios reported from Gutierrez *et al.* [135] and their stiffness was measured using AFM (see Materials and methods). We noticed that our gels had an actual stiffness value higher than the one reported in the Gutierrez *et al.* paper (See Fig. 4.8). Consequently, we decided to report next to the gels ratio used, also the stiffness values we measured (see Materials and methods).

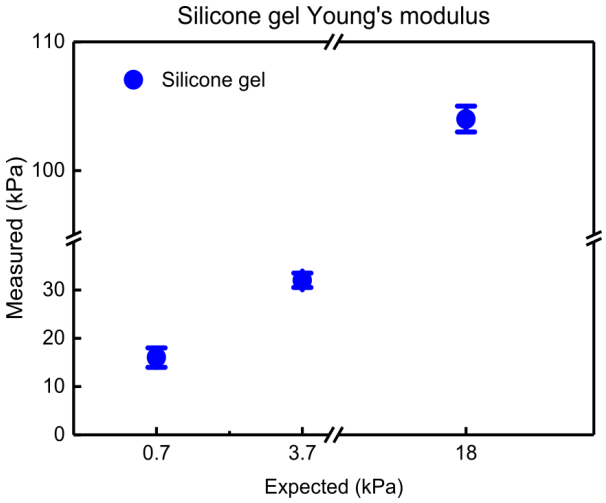



Fig. 4.8 Silicone gel stiffness values measured (gels produced in our BPI lab) versus the expected values (accordingly to the Gutierrez *et al.* paper [135]). N. of repeats 3.

.

Finally, different bead densities were tested to increase the spatial sensitivity of TFM, taking advantage of the PSF improvement using TIRF-SIM. While theoretically the maximum bead density can be 82 beads/$\mu m^2$ (see, Subsection 4.5.2), experimentally we

noticed that by increasing the bead density above 20 beads/$\mu m^2$, the protein density was affected and consequently the cell interaction with the gel surface.

### 4.5.5 2D TIRF-SIM-TFM of adherent HeLa cell

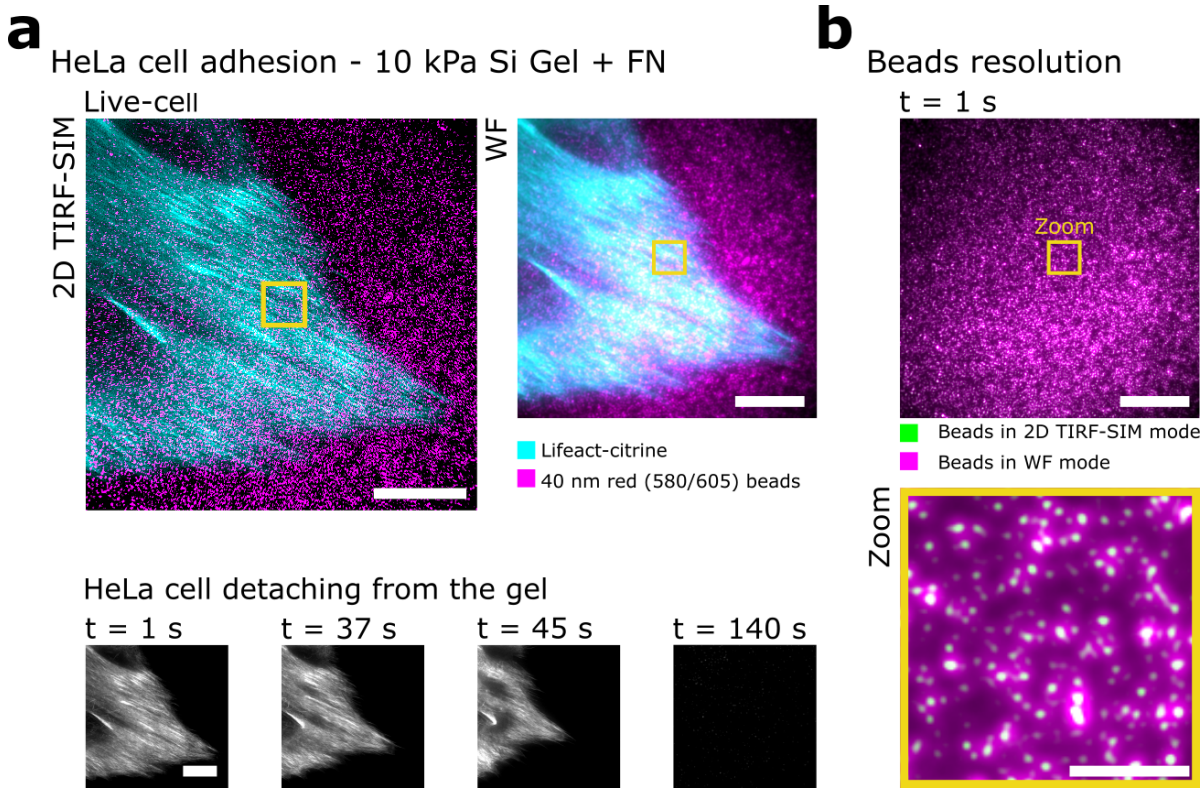



Fig. 4.9 **a** Upper – Representative 2D TIRF-SIM imaging of a HeLa cell expressing Lifeact-citrine (cyan) on top of a 20 µm thick silicone gel coated with FN and 40 nm fluorescent beads (magenta). Upper right – Equivalent image in WF obtained by averaging 9 raw frames acquired in TIRF-SIM mode. Lower – Snap shots of the HeLa cell over the course of 140 s while detaching from the gel. Scale bar is 10 µm. **b** Superimposed 2D TIRF-SIM (green) and WF (magenta) bead images comparing the bead resolution. Zoom-in shown below. Scale bar is 10 µm and 2 µm, respectively.

Having established the technical capabilities of 2D TIRF-SIM-TFM and a guide for the optimal PIV window size selection, we next explored its performance measuring small and rapid mechanical forces in cells. Aiming to highlight the biocompatibility of the technique and its spatial and temporal sensitivity improvement, we examined

mechanical force production in three different cell types, comparing the quality of the displacement field recovered using 2D TIRF-SIM-TFM and the standard WF-TFM at varying temporal acquisition rates. The three different biological systems selected were the cervical HeLa cancer cells line, the RBL cells line and the primary primary salmon keratocytes. The HeLa cells were used as a model for validating of the 2D TIRF-SIM-TFM technique, the RBL cells for testing the TFM sensitivity in the presence of small-scale force generation under receptor-ligand binding, and the model of cell migration in primary salmon keratocytes for rapid and small-scale force generation that have been shown to be involved in wound-healing [177, 178].

To allow a visual inspection correlation between the force generation and the actin structures in the basal plane of the cells, the HeLa and RBL cells were transduced to stably express Lifeact-citrin, while the salmon keratocytes were labelled with CellMask Green correlating force generation with cell membrane dynamics. Dual-colour sequential acquisition was implemented to image both the cell (Lifeact-citrine, 516 nm excitation, 529 nm emission; CellMask Green 522 nm excitation, 535 nm emission) and the fluorescent marker beads on top of the gel surface (580 nm excitation, 605 nm emission). The excitations lasers used were 488 nm for the cells and 561 nm for the beads (see Materials and methods).

We first started with the validation of the 2D TIRF-SIM-TFM technique measuring force during HeLa cell detachment from the gel substrate. HeLa cells were left to adhere overnight to a 10 kPa silicone gel, functionalised with a thin layer of fibronectin (FN) and fluorescent marker beads at a density of 12 beads per $\mu m^2$ (Fig. 4.9a,b). To maximise the advantage of the high-spatial resolution of TIRF-SIM, the fluorescent beads must have a diameter smaller than the spatial resolution of the technique, that is 110 nm. For this reason, the fluorescent beads chosen had a diameter of 40 nm, yet bright and stable fluorescent signal, enabling both high resolution force mapping with minimal

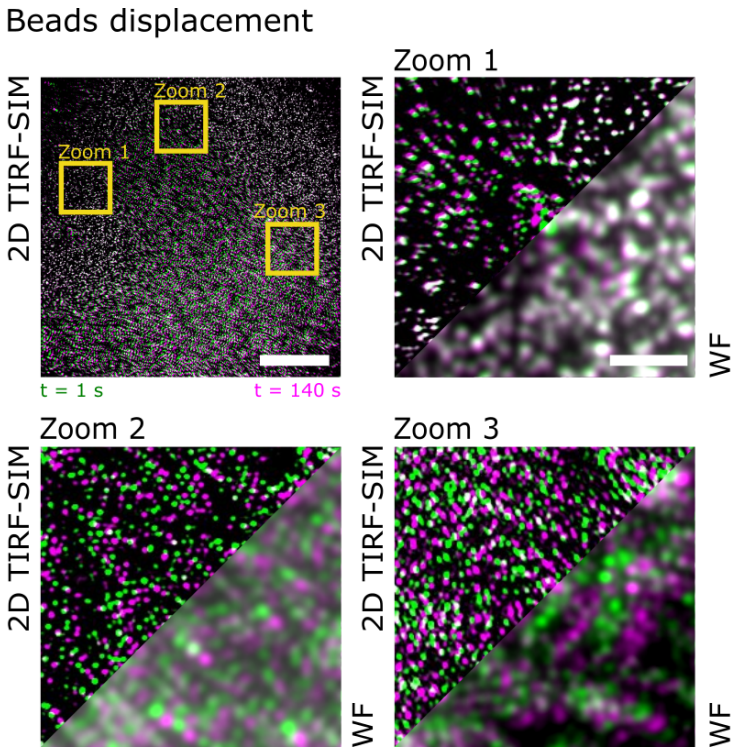



Fig. 4.10 Beads displacement during HeLa cell retraction with 2D TIRF-SIM and WF. **(a)** Bead positions at t = 1 sec (green) and t = 140 sec (magenta) superimposed to highlight the bead displacements. The zoom of three areas shows the differences between 2D TIRF-SIM and WF imaging. Scale bar is 10 μm and 2 μm, respectively.

photo-bleaching. We quantified lateral mechanical force production at the ventral contact of HeLa cells during cell-gel detachment after treatment with 0.05% trypsin–EDTA. A series of image frames over time were acquired at a moderate frame-rate of 0.25 frames per second (fps) over a total duration of 140 s, allowing the quantification of shear stress in the range of 0 - 1 kPa over the whole retraction process (Fig. 4.9a,b).

Aligned with previous measurements [151, 172, 184], we observed the relaxation of a shear stress generated by the cell on the gel across the FOV, as highlighted by overlaying the initial and final image frames acquired in both TIRF-SIM and WF modality (Fig. 4.10). The shear stress relaxation can be visually correlated with individual actin-labelled adhesions contacts as the HeLa cell detached from the surface. To test the spatial sensitivity of TFM with regards to the PIV window size choice, the gel displacement was recovered using three different PIV window sizes: 480 nm, 720 nm and 960 nm (see Fig. 4.11a). Consistent with the guide for optimal PIV window size choice, extracted from the computer-simulations with sparse bead density (see Fig. 4.6a,c), the PIV analysis confirmed that for a maximum displacement of 800 nm the optimal choice is 720 nm x 720 nm PIV window size (see Fig. 4.11a and Fig. 4.6c). Note, the larger 960 nm x 960 nm PIV window size gave visually comparable results to the one recovered with 720 nm PIV window, it induces more displacement averaging.

Instead, as predicted from the computer-simulations, the smaller 480 nm x 480 nm PIV window size could recover with higher precision small displacements but failed in recovering the large 800 nm displacement located at the cell edge (Fig. 4.11a). This was also confirmed by the visual comparison of the Life-act labelled cell structure with the shear stress fields Sx,y, which maximum value recovered is 900 Pa (Fig. 4.11b). From the zooms of the shear stress fields recovered using the three different PIV window sizes, it is possible to visually appreciate how the small PIV window allowed a more accurate recovery of small stress details while large PIV window induced evident smoothing of the

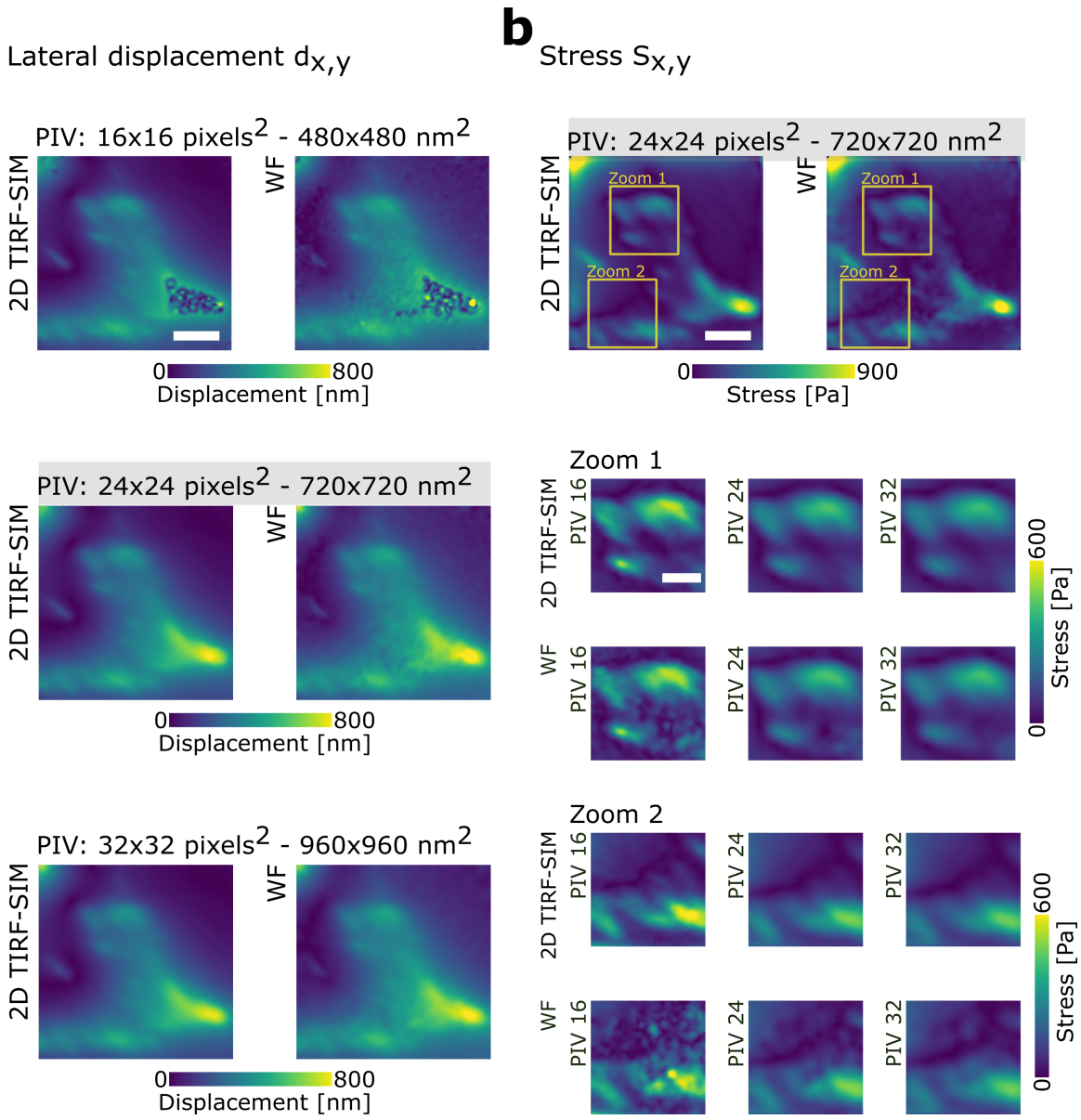



Fig. 4.11 **(a)** Lateral displacement magnitude of the gel generated by the HeLa cell before detaching from the gel, recovered with 2D TIRF-SIM-TFM and WF-TFM. The displacement magnitude is shown for PIV window sizes of 16, 24, and 32 px. The maximum estimated displacement is 800 nm. Based on the simulations outline in Figure 1, the optimal PIV window is chosen to be 24 px. Scale bar is 10 µm. **(b)** Lateral stress induced to the gel by the HeLa cell before detaching. Stress is calculated with the optimal PIV window size of 24 px. The lateral stress of two areas (zoom 1 and 2) with higher density of focal adhesions is recovered using all three PIV windows (16, 24, 32 px). Maximum stress recovered was 900 Pa. Scale bar is 10 µm and 5 µm, respectively.

stress field. Importantly, for all the three PIV cases, 2D TIRF-SIM-TFM provided better results in terms of signal-to-noise level for the stress fields, over WF-TFM (Fig. 4.11a,b and Fig. 4.7e,f).

### 4.5.6 2D TIRF-SIM-TFM of RBL cell activation

After the validation of the 2D TIRF-SIM-TFM technique investigating mechanical forces during HeLa cell detachment from the silicone gel, we wanted to explore the sensitivity of the novel technique resolving smaller force regimes. For that, we next examined mechanical force production in rapidly activating RBL cells, which shear stress Sx,y is the range of 0 - 40 Pa. To increase the spatial sensitivity of TFM, the bead density was increased to 15 beads per $\mu m^2$ (see Fig. 4.13a). RBL cells the Fc$\epsilon$ receptor-1 (Fc$\epsilon$RI) were let activate while interacting with a 10 kPa gel substrate functionalised with Fc$\epsilon$RI-specific antibody IgE.

RBL activation on the silicone gel, and the consequently actin cytoskeleton dynamics, was imaged using comparable parameters to the HeLa cell experiments, with a frame rate of 2.5 fps, as displayed by the temporal projection of the cell over a total of 200 sec acquisition period (Fig. 4.12a). To be sensitive to the small displacement generation, ranging from 0 - 30 nm, a higher bead density of 20 beads per $\mu m^2$ was used together with a 600 nm x 600 nm PIV window, as the optimal choice indicated by the computer-simulations (Fig. 4.6). We could observed the relaxation of displacement field generated by the RBL across the FOV over time thanks to, together with individual displacements features generated by freshly formed adhesion contacts at the central interface of the RBL cell (Fig. 4.12b). These findings were also reflected in the resulting shear stress field, with a maximum stress value of 40 Pa (Fig. 4.12c). Strikingly, the displacement and stress fields could be recovered only using 2D TIRF-SIM-TFM, while WF-TFM showed a total loss in recovering the force generations, displaying only background noise in the displacement and stress fields (see Fig. 4.12b,c and Fig. 4.7e,f). Next, to extend also the temporal sensitivity of TFM, we quantified mechanical force production during RBL activation at a high frame-rate of 2.5 fps over a total duration of 8 sec (Fig. 4.13a). The new imaging settings showed only in background noise and no detectable displacement

with both 2D TIRF-SIM-TFM and WF-TFM (Fig. 4.13b), suggesting that the acquisition frame-rate exceeded the biological time-scale of RBL force production upon activation (Fig. 4.13c).

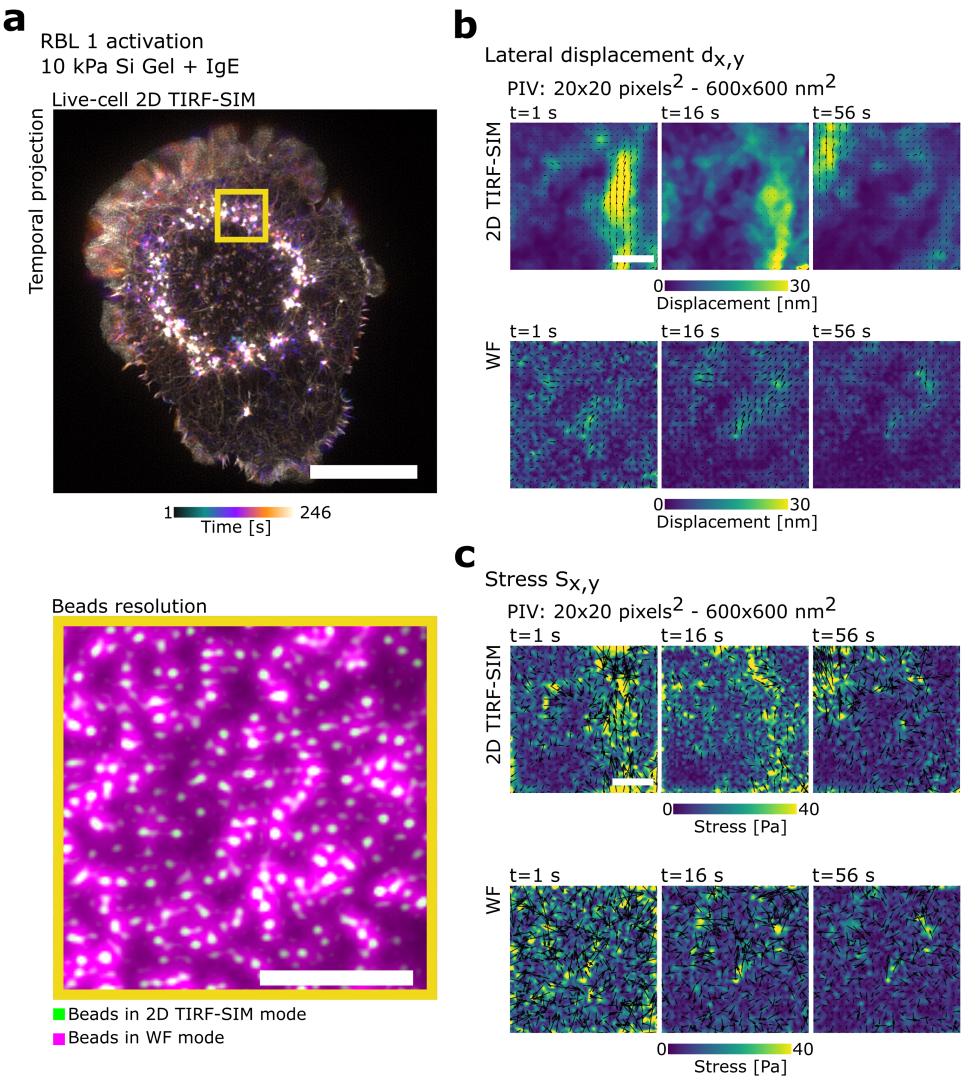



Fig. 4.12 RBL cell activation on 10 kPa silicone gel with slow acquisition. **(a)** Upper – Representative temporal projection of 2D TIRF-SIM imaging of RBL cell expressing Lifeact on top of the silicone gel coated with IgE and 40 nm fluorescent beads. Scale bar is 10 µm. Lower – Zoom-in of the bead distribution underlying the RBL cell imaged by TIRF-SIM (green) and WF (magenta). Scale bar is 5 µm. **(b)** Lateral displacements of the gel quantified using a 20 px PIV window size, with TIRF-SIM (top) and WF (bottom) imaging, over the time course of 70 s. Vector map overlayed. Scale bar is 10 µm. **(c)** The corresponding lateral stress with TIRF-SIM (top) and WF (bottom) imaging. Vector map overlayed. Scale bar is 10 µm.

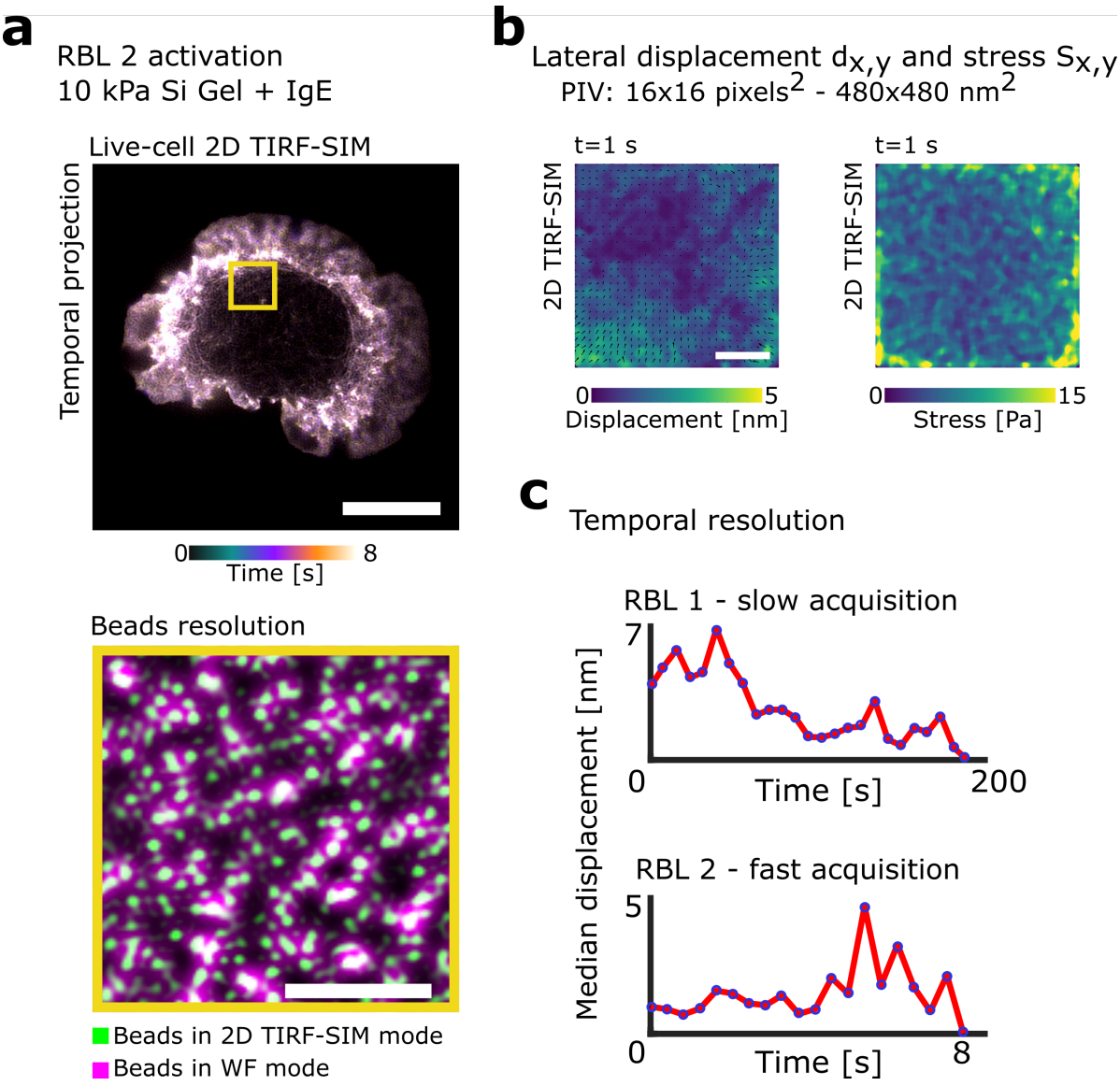



Fig. 4.13 RBL cell activation on 10 kPa silicone gel with fast acquisition. **(a)** Upper – Representative temporal projection of 2D TIRF-SIM imaging of RBL cell imaged using the maximum frame rate of 2.5 fps. Scale bar is 10 µm. Lower – Zoom-in of the bead distribution underlying the RBL cell imaged by TIRF-SIM (green) and WF (magenta). Scale bar is 5 µm. **(b)** Lateral displacement and stress fields showing the absence of force generation during rapid 2.5 fps TIRF-SIM imaging of RBL cell activation analysed with a PIV window size of 16 px. Scale bar is 10 µm. **(c)** Line plots showing the median displacement per frame for both intermediate (0.25 fps) and rapid (2.5 fps) TIRF-SIM acquisition during RBL cell activation.

### 4.5.7 2D TIRF-SIM-TFM of primary salmon keratocyte cell migration

Lastly, to highlight the temporal sensitivity of 2D TIRF-SIM-TFM we quantified mechanical force production of fast migration of primary salmon keratocytes while interacting with a 10 kPa silicone gel coated with red 40 nm fluorescent beads at a density of 15 beads per $\mu m^2$ (Fig. 4.14a). The model of primary salmon keratocytes is commonly used for cell migration studies during wound-healing processes [177, 178]. Those cells present a range of different morphologies that has to been shown to dictate their migration speed [178, 185]. Because we wanted to underline the increased temporal resolution of TFM using TIRF-SIM, we quantified mechanical force generation of the fast migrating single-cells salmon keratocytes (Fig. 4.14a). To capture the migration of single salmon keratocytes, salmon scales were allowed to adhere over 24 hrs to 10 kPa silicone gels. After 24 hrs, salmon keratocytes in the form of a cell sheet started to migrate from the scale to the gel, with single cells detaching over time from the cell sheet (see Materials and methods). High 2.5 fps frame-rate was used to image cell migration and force generation, over a total acquisition duration of 24 sec (Fig. 4.14a). Since this time the cells were primary cells, we decided to have a 5 sec interval after 30 dual-colours super-resolved frames, to reduce photo-toxicity.

We started by extracting the migration velocity of the salmon keratocytes, by plotting the cell profile along the orthogonal axis of the cell and tracking the displacement of leading-edge of the cell over time. The migration velocity resulted to be 100 nm/sec, as similarly observed in previous works [178, 185] (Fig. 4.14a) (see Materials and methods). Mechanical forces were recovered underneath the lateral cell extremities along the tangential axis, as was shown in previous work [104]. This could be visually observed by overlaying the relaxed gel state (acquired at the end of the cell migration) and the first frame of the gel, in both TIRF-SIM and WF modalities (Fig. 4.14c). Indeed, zooms 1

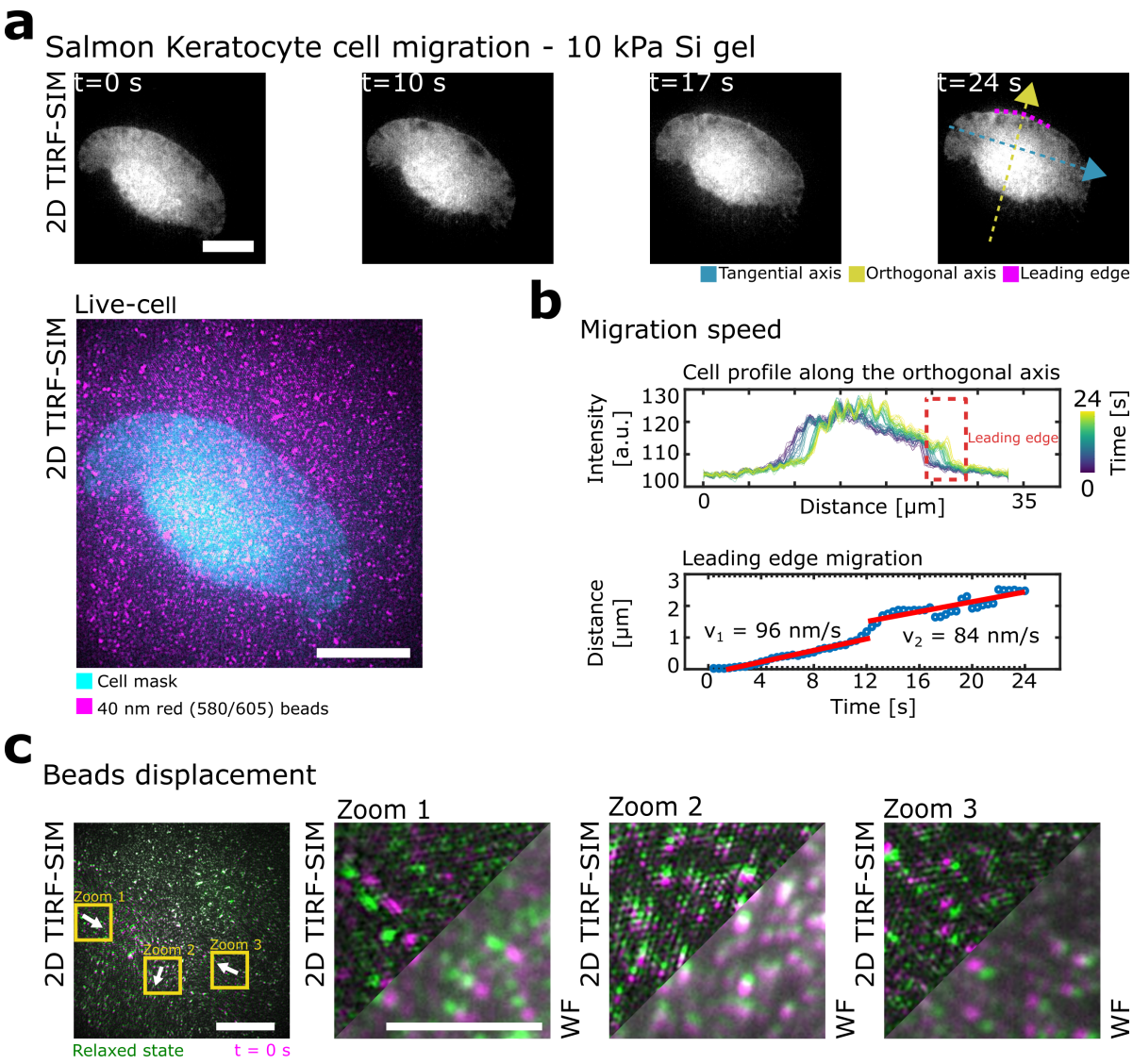



Fig. 4.14 Primary salmon keratocyte cell migration on a 10 kPa silicone gel. **(a)** Upper – Snap shots of a primary salmon keratocyte over the course of 24 s while migrating on top of a 20 µm thick silicone gel coated with 40 nm fluorescent beads. Cell leading-edge (magenta), the orthogonal axis (yellow) and the tangential axis (light-blue) both in respect to the leading-edge represented in the last snapshot at t = 24 s. Lower - 2D TIRF-SIM image of the live-cell salmon keratocyte labelled with green cell mask (here represented in cyan for better visualisation) on top of the silicone gel coated with 40 nm fluorescent beads (magenta). **(b)** Cell plot profile along the orthogonal axis over 24 s of cell migration. Dropping down in intensity of the line profiles due to the leading-edge of the cell (red box). Scatter plot of the leading-edge position and cell migration velocity estimated from the curve slop, over 24 s of migration. Scale bars 10 µm. **(c)** Bead positions at the relaxed state of the gel (green) and t = 0 sec (magenta) superimposed to highlight the bead displacements. Scale bar 10 µm. The zoom of three areas shows the differences between 2D TIRF-SIM and WF imaging and displacement magnitude heterogeneity. Scale bar 5 µm.

and 3 exhibit large fluorescent marker beads displacements in the lateral extremities of the cell, both pointing towards the cell body. Differently is the displacement observed in zoom 2, where fluorescent marker beads at the back of the cell have a smaller shift outwards from the cell body (Fig. 4.14c, white arrows). This observation clearly indicated the heterogeneity of the displacement range generated by the salmon keratocytes during migration. Therefore, we decided to recover the displacement and stress fields using a range of PIV window sizes going from 12 to 32 pixels (360 to 960 nm) (Fig. 4.15). Consistent with the computer-simulations analysis and the HeLa cell case, small PIV window enhances spatial information, but fails in estimating large displacement values. Since the maximum displacement observed was 800 nm, we decided to select the 32 pixels PIV window size to recover the overall gel displacement compared to the relaxed state (Fig. 4.16a). The maximum shear stress field recovered with these settings was 1500 Pa, value consistent with previous studies [171, 104] (Fig. 4.16b).

To asses whether there was a temporal evolution of force fluctuations over time, we analysed the derivative of the displacements field. Interestingly, the displacement derivative showed only noise background, suggesting that the displacement evolution between one frame the other was extremely small, with the only exception at frame 30, where the 30 sec interval was taken for minimising cell photo-toxicity therefore showing larger displacement values (Fig. 4.17). With this evidence, we then decided to look at the small change over time of the gel displacement registered between frames separated by an interval of 4 frames. This reduced the time resolution to 0.6 fps (see Materials and methods). Crucially, this second analysis revealed a vortex-like shape of small gel displacements underneath the lateral cell extremities, showing at the same time both contraction and relaxation. Most importantly, this outcome was only observed using the 2D TIRF-SIM-TFM technique, while WF-TFM showed only background noise (Fig. 4.18b, upper panel and lower panel for the corresponding zoomed areas). Finally, the

temporal projection and kymograph plots of the displacement field along the orthogonal and tangential axes were plotted to highlight the rapid bead displacement evolution generated by the cell migration. This fast evolution was captured only that to the fast 2.5 fps acquisition speed (Fig. 4.19).

### 4.5.8 Summary

In this section, I have described how the lateral spatial and temporal resolution of TFM can be extended combining TIRF-SIM microscopy with TFM. This has been shows via computer-simulations and live-cells imaging. In particular, by testing the capabilities of the novel 2D TIRF-SIM-TFM technique on the three settings of HeLa, RBL and primary salmon keratocyte cells, we could observe small-scale force production during activation of RBL cells and fast large- and small-scale force production during primary salmon keratocytes migration. For the HeLa cell biological sample, the large stress (Sx,y = 1 - 900 Pa, 1 - 900 pN/$\mu m^2$) recovered with both 2D TIRF-SIM-TFM and WF-TFM was of a comparable quality using a 24 px window size, while analysis with smaller PIV sizes revealed a better recovery of displacements generated by focal adhesions 2D TIRF-SIM-TFM. For the RBL cells, 20-fold smaller stresses compared to the HeLa cells (Sx,y = 1 - 20 Pa, 1 - 20 pN/$\mu m^2$) could be recovered only using 2D TIRF-SIM-TFM, with a bead density of 12 beads/$\mu m^2$ and a PIV window size of 20 px. Lastly, for the primary salmon keratocytes, while the large stress (1 - 1500 Pa, 1 - 1500 pN/$\mu m^2$) was recovered with comparable quality for both 2D TIRF-SIM-TFM and WF-TFM, only 2D TIRF-SIM-TFM allowed to recover small gel displacements contracting and relaxing with a vortex-like shape over time, highlighting the experimental power of the technique. Future advances should focus on combining super-resolution imaging with reference free methodology, such as nano-patterning techniques [158, 105]. Another method to increase the spatial sensitivity of 2D TIRF-SIM-TFM for force probing, would be to combine

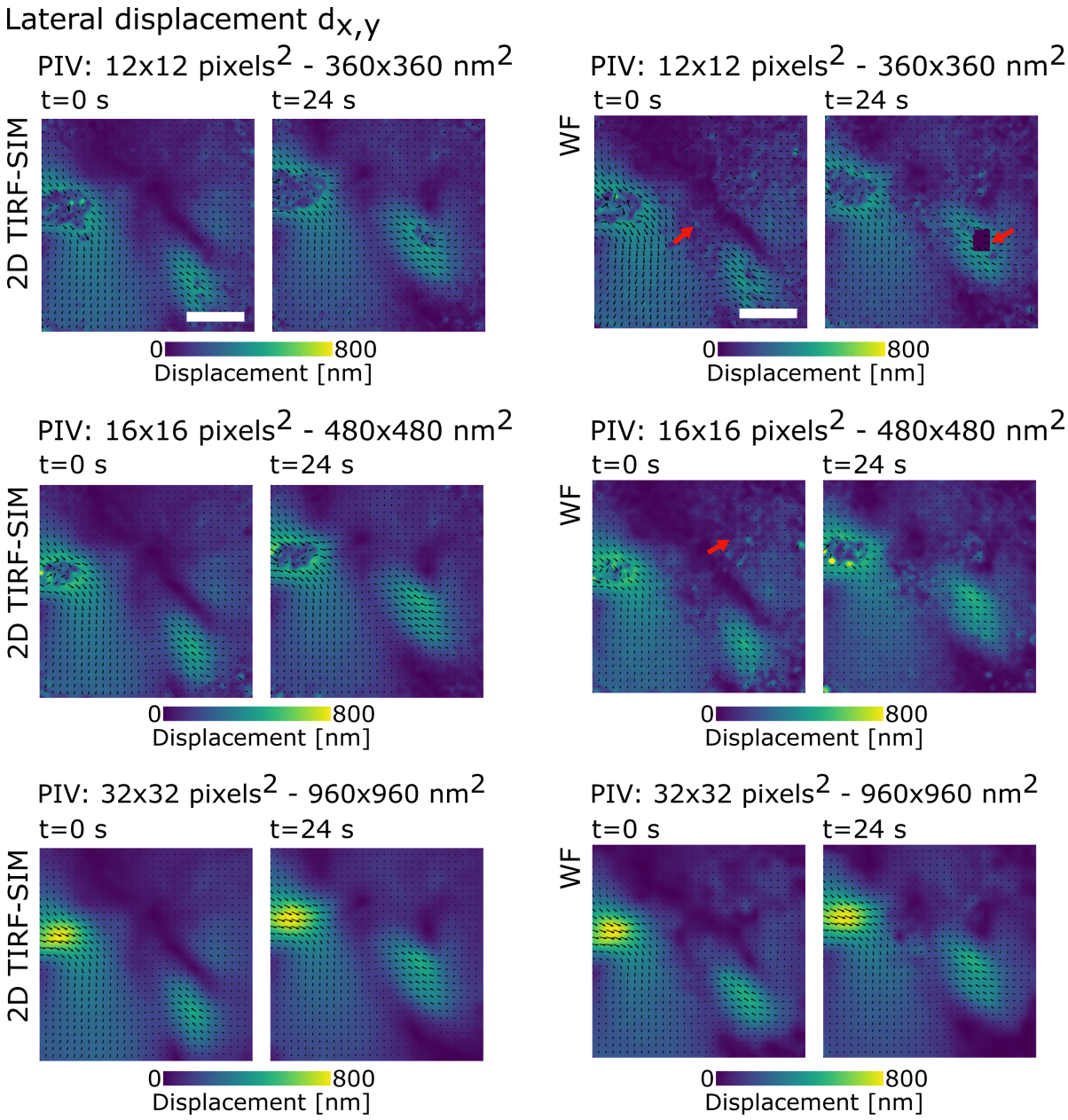



Fig. 4.15 Primary salmon keratocyte: lateral displacement at different PIV window sizes. Lateral displacement magnitude of the gel generated by the Salmon keratocyte cell on top of the gel at time 0 and 24 sec, recovered with 2D TIRF-SIM-TFM (left) and WF-TFM (right). The displacement magnitude is shown for PIV window sizes of 12, 16, and 32 px. The maximum estimated displacement was 800 nm. Optimal PIV window is chosen to be 32 px. Scale bar is 10 µm. Red arrows point to the noise.

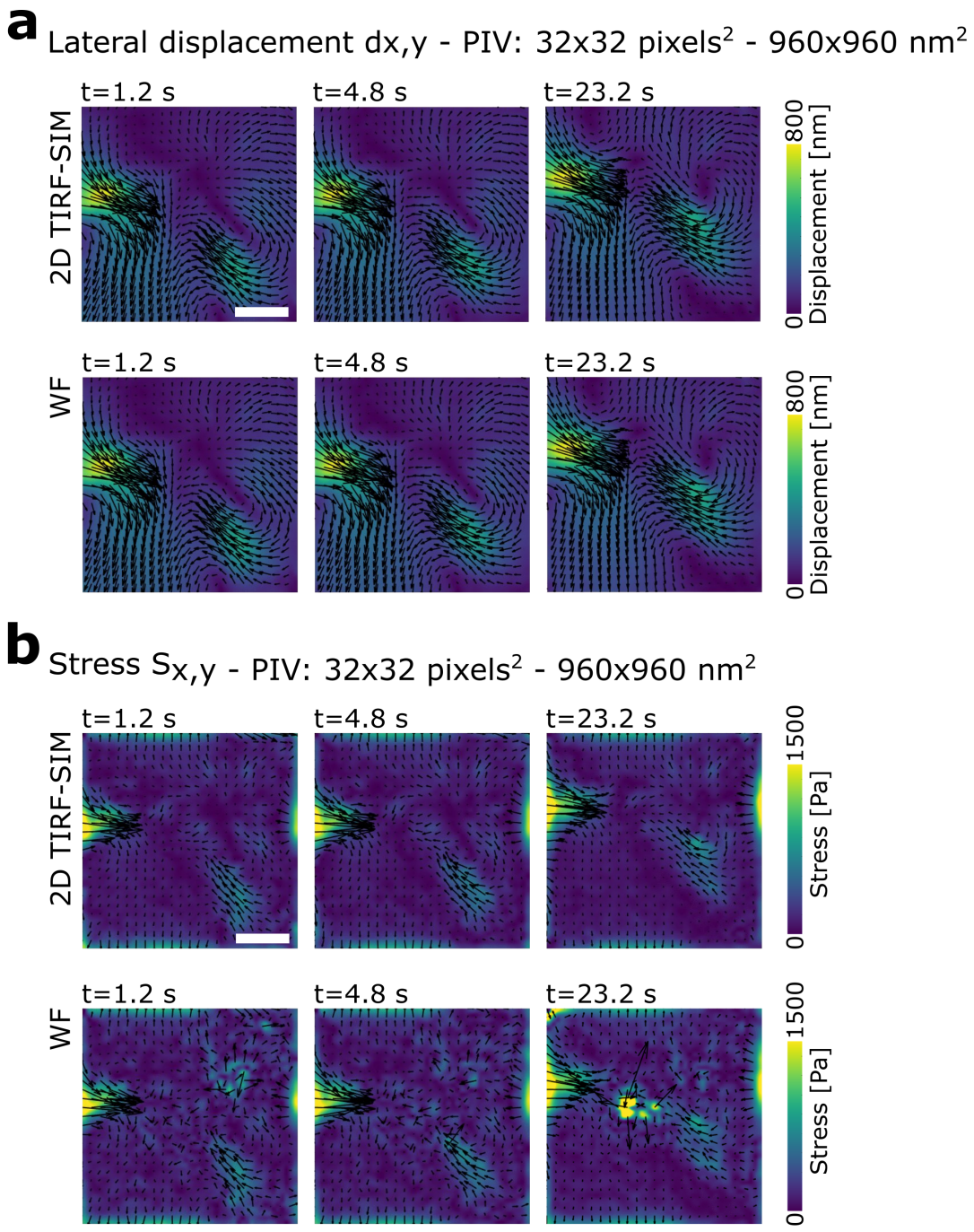



Fig. 4.16 Primary salmon keratocyte: lateral displacement and force magnitude. **(a)** Lateral displacement magnitude of the gel generated by the salmon keratocyte cell on top of the gel at time 1.2 sec, 4.8 sec and 32.2 sec, recovered with 2D TIRF-SIM-TFM and WF-TFM. The displacement is calculated using a PIV window size of 32 px. The maximum estimated displacement is 800 nm. The vector map is overlayed to the displacement field. Scale bar is 10 μm. **(b)** Lateral stress of the gel generated by the salmon keratocyte on top of the gel at time 1.2 sec, 4.8 sec and 32.2 sec, recovered with 2D TIRF-SIM-TFM and WF-TFM using a PIV window size of 32 px. The maximum stress recovered was 1500 Pa. Scale bar 10 μm.

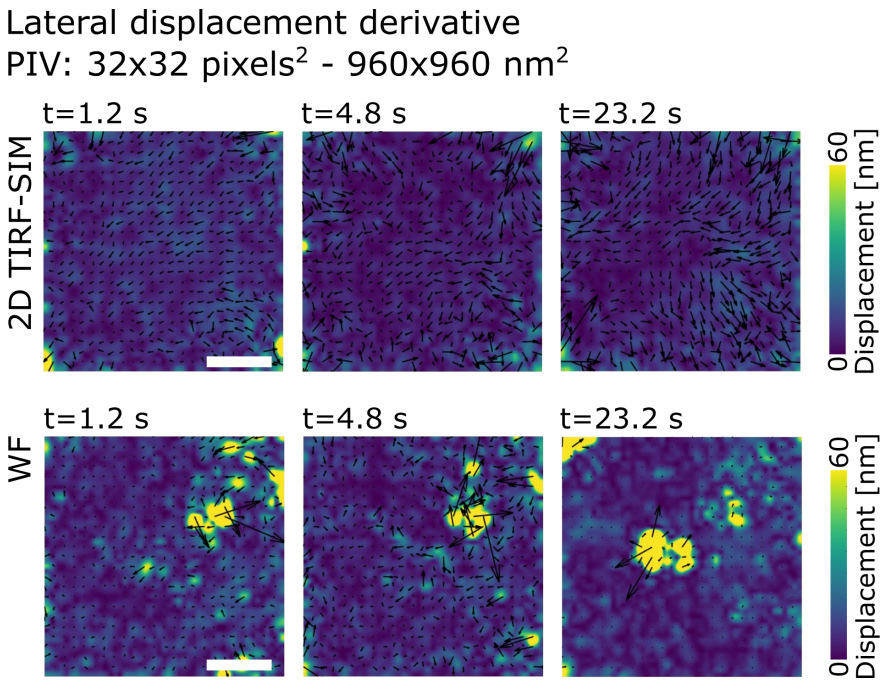



Fig. 4.17 Primary salmon keratocyte: lateral displacement derivative. Derivative of the displacement calculated using a PIV window size of 32 px showing the absence of small displacements detected, for both 2D TIRF-SIM-TFM and WF-TFM. The vector map is overlayed to the displacement field. Scale bar is 10 μm.

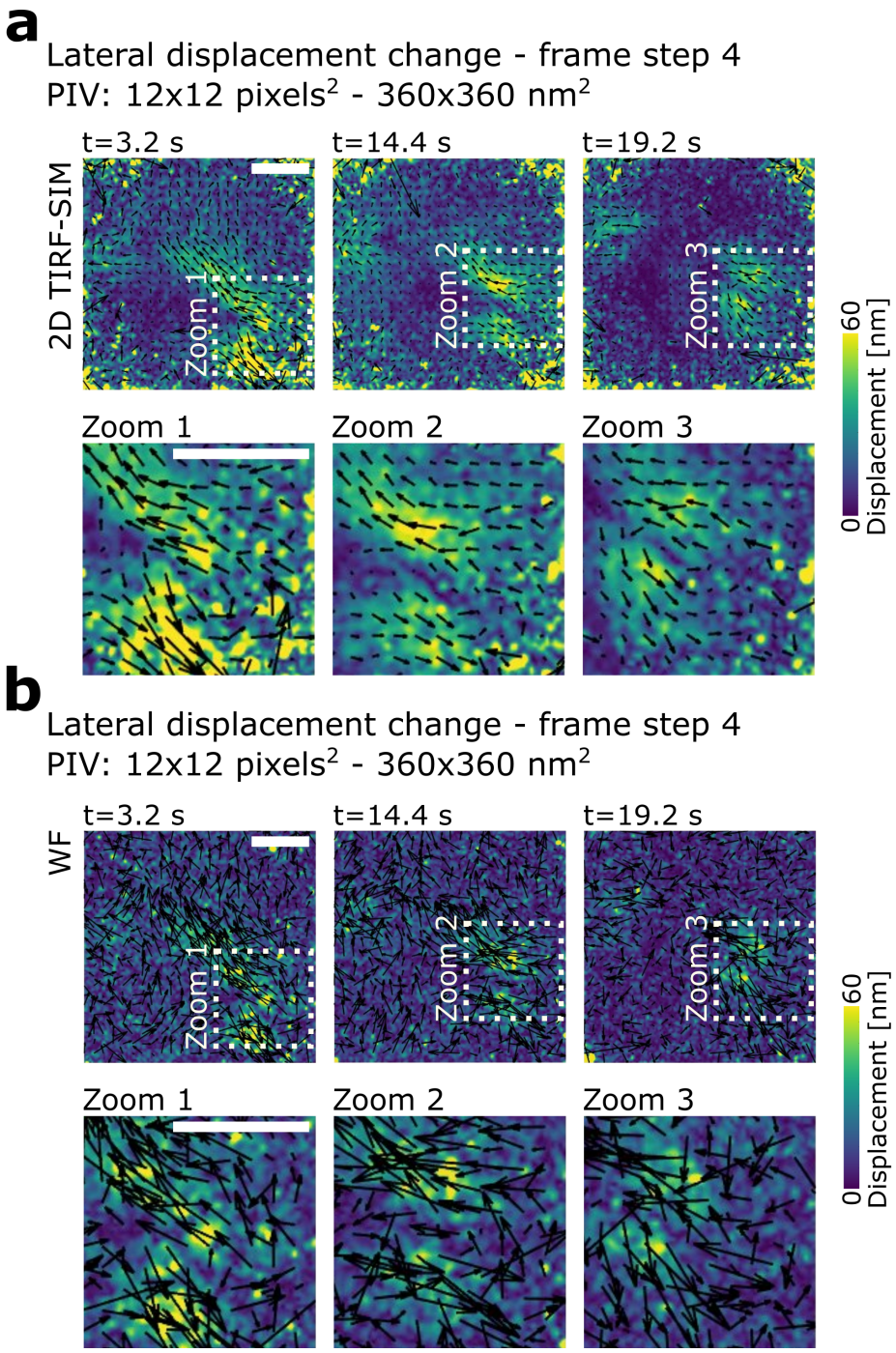



Fig. 4.18 Primary salmon keratocyte: small-scale changes in lateral displacement. **(a)** Upper - Lateral change of the displacement magnitude extracted using a PIV window size of 12 px and a step of 4 frames, for 2D TIRF-SIM-TFM. Lower – Zoom in of the gel structure under stress. Scale bars 10 μm. **(b)** Upper - Lateral change of the displacement magnitude extracted using a PIV window size of 12 px and a step of 4 frames, for WF-TFM. Lower – Zoom in of the gel structure under stress. Scale bars 10 μm.

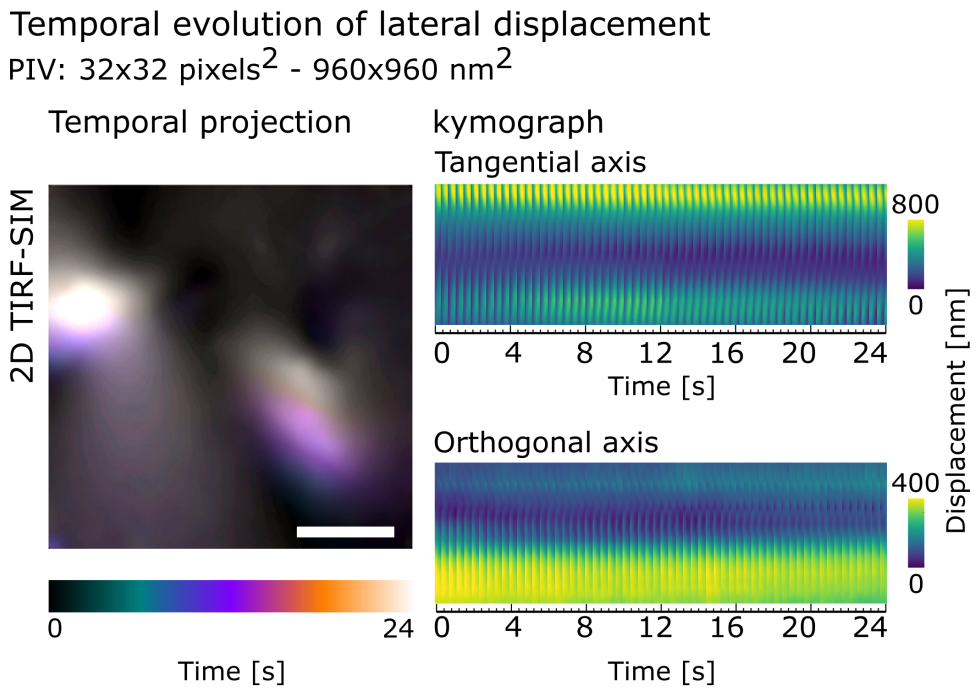



Fig. 4.19 Temporal evolution of the lateral displacement of salmon keratocyte during migration. Right - Temporal projection of the displacement field recovered with 2D TIRF-SIM-TFM over 24 sec. Scale bar 10 µm. Left - kymograph of the displacement field recovered with 2D TIRF-SIM-TFM along the tangential and orthogonal axes. Each minor tick in the time axis represents a single super-resolved frame acquired in 0.4 sec (2.5 fps).

multi-colours fluorescent marker beads with high density distribution, acquired using two different colour-channels [149].

Overall, thanks to the high spatio-temporal resolution of 2D TIRF-SIM-TFM methodology we could recover lateral small-length scale and fast-time scale force generation that were hidden with standard WF-TFM methodologies. However, 2D TIRF-SIM-TFM cannot capture forces in the axial direction, limiting the technique to shear stress.

## 4.6 3D SIM-TFM

The 2D TIRF-SIM-TFM methodology demonstrated a 2-fold improvement of the lateral spatial resolution and a 10-fold improvement of the temporal resolution, compared to conventional TFM modalities. However, the nature of the TIRF illumination restricts this imaging modality to a single 2D plane, therefore only a 2D stress map can be reconstructed. This is a major limitation of 2D TIRF-SIM-TFM whenever biological processes involving 3D forces have to be investigated. To this end, the SIM modality can be extended to a 3D mode with minor modifications creating a diffraction illumination pattern also in the axial direction to obtain 3D SIM-TFM [125] (Fig. 4.20). To switch from the TIRF-SIM modality to 3D SIM, an appropriate pattern needs to be uploaded to the SLM, an additional illumination beam needs to pass through the mask to produce a 3D pattern, and the objective needs to be changed to one which has a refractive index matching the imaging media. To obtain a single-colour super-resolved 3D SIM image, 15 raw images have to be acquired (3 angles and 5 phases) (Fig. 4.20). The spatial resolution of 3D SIM is 100 nm laterally and 250 nm axially (Table 4.1 and Fig. 4.21a). To be able to measure the full axial bead displacement within a couple of micrometers, a z-stack is required.

To highlight the capabilities of 3D SIM-TFM, we quantified 3D force generation of HeLa cells during adhesion. Importantly, because this time we needed to quantify the 3D bead displacements, SPT analysis was chosen over PIV.

### 4.6.1 3D SIM-TFM of adherent HeLa cell

The capabilities of 3D SIM-TFM were tested measuring the rapid force evolution during early adhesion of HeLa cells on a silicone gel, with a particular focus on the normal forces exerted by early adhesion contacts [106]. In contrast to many studies that focused only

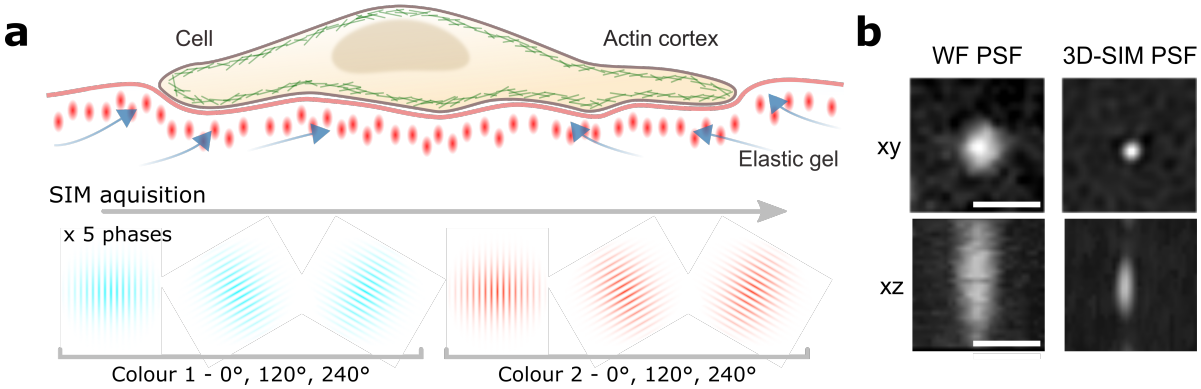



Fig. 4.20 **(a)** Experimental design of the 3D SIM-TFM methodology. **(b)** Representative bead images showing the 3D SIM PSF size improvement in both lateral and axial directions compared to WF. Scale bar is 0.5 µm. Image adapted from Coli-York *et al.* [125].

on lateral forces during early formation of adhesion sites [186, 74], recent studies indicate also the presence of vertical forces [106].

Even though the SIM set-up was not in TIRF mode, we decided to use the silicone gel to optimise the imaging conditions of the beads on top of the gel, by matching the refractive index of the gel with the refractive index of the glass coverslip. HeLa cells were let to adhere on a 10 kPa silicone gel and, after 10 min from their deposition, a 2 µm z-stack was recorded. To record gel displacement generated during HeLa cell adhesion, the top gel surface was functionalised with FN and coated with red 100 nm fluorescent marker beads. The fluorescent marker bead density chosen was such that at least 80% of beads could be tracked at 3D SIM resolution, compared to a less than 40% in WF modality, leading to a bead density of 1 bead per $\mu m^2$ (Fig. 4.21b) [125]. This severe reduction of the bead density, compared to the 15 - 20 beads per $\mu m^2$ used in 2D TIRF-SIM-TFM, is due to the necessity of using SPT to recover 3D mechanical force, instead of PIV. Three-dimensional bead displacements were extracted using the SPT algorithm from the Python library called Trackpy (https://soft-matter.github.io/trackpy/v0.3.2/index.html) [138]. Specifically, the x,y,z coordinates of the beads were extracted in each z-stack using the tracking algorithm, and consequently the coordinate of each bead was linked over time

to generate particle trajectories. Drift correction was applied to all the trajectories using a reference bead far away from the cell, where the gel displacement was defined as null. To record the 3D beads displacement generated by the HeLa cells, a 2 μm z-stack was recorded for a total duration of 200 sec. In particular, a two-colour stack was acquired to record simultaneously the cell and gel displacements. At each time point, the z-stack consisted of 420 frames (5 phases x 3 angles x 14 z-slices x 2 colours) acquired with an exposure time of 10 ms per raw frame, resulting to a total acquisition time of 10 sec per stack [125]. Figure 4.22 shows a representative example of HeLa cell adhering on top of a silicone gel. The experiments were repeated in at least 3 independent days and on at least 20 individual HeLa cells. As mentioned before, the 3D displacements generated by the HeLa cells were extracted using the SPT approach. Thanks to the 3D SIM technique we could observe shear stress (Sx and Sy) indicated by the contraction and relaxation of the gel over time (Fig. 4.22b) together with normal stress (Sz) obtained from the orthogonal displacement of the gel (Fig. 4.22c). An orthogonal displacement within 1 μm range was detected (Fig. 4.22c). From the displacement fields, the 3D stresses were quantified by our collaborators using Finite Element (FE) calculations with the last frame as reference. Figure 4.23 and figure 4.24 show the displacement and the stress fields evolution during HeLa cell adhesion. Both the shear and normal stress fields indicate a reduction over time, with a maximum value of 1.5 kPa and 0.2 kPa respectively (Fig. 4.24).

### 4.6.2 Summary

In this section, I have described how mechanical forces vertical to the elastic substrate can be captured using the combination of 3D SIM and TFM. With minor modifications applied to the 2D TIRF-SIM-TFM set-up, the novel 3D SIM-TFM methodology offers volumetric force probing with a compromise between high spatial resolution and intermediate temporal acquisition. In addition, thanks to the WF illumination, the phototoxicity is

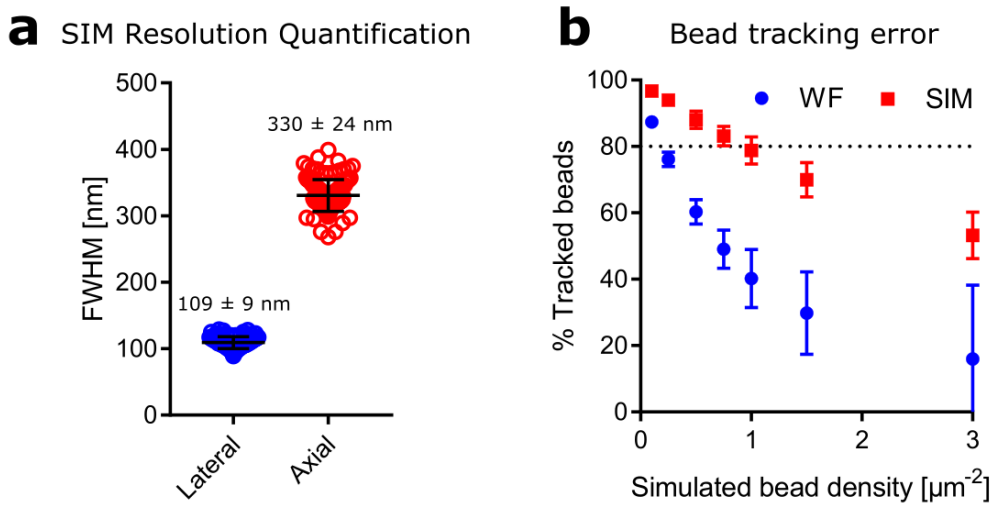



Fig. 4.21 **(a)** 3D SIM-TFM resolution quantification showing lateral and axial FWHM. **(b)** Estimation of fluorescent beads trackability as a function of simulated bead density, for both 3D SIM-SIM and WF-TFM. Image adapted from Coli-York *et al.* [125].

reduced. The major limitation that comes from 3D SIM-TFM is that in order to have the axial force component, it is necessary to acquire a z-stack. The scanning along the axial direction reduces of 10-fold the acquisition speed compared to 2D TIRF-SIM-TFM. Overall, despite in being slower compared to 2D TIRF-SIM-TFM, 3D SIM-TFM allows the visualisation of 3D mechanical forces with high spatial sensitivity and minimised photo-bleaching.

## 4.7 aTFM

### 4.7.1 Astigmatic TFM coupled with high resolution TIRF-SIM cellular imaging

As mentioned in the above section, 3D SIM-TFM can provide both shear and normal stress measurements, however it is restricted in its temporal resolution due to the axial scanning (Table 4.1). In the past few years, astigmatic imaging was introduced in single

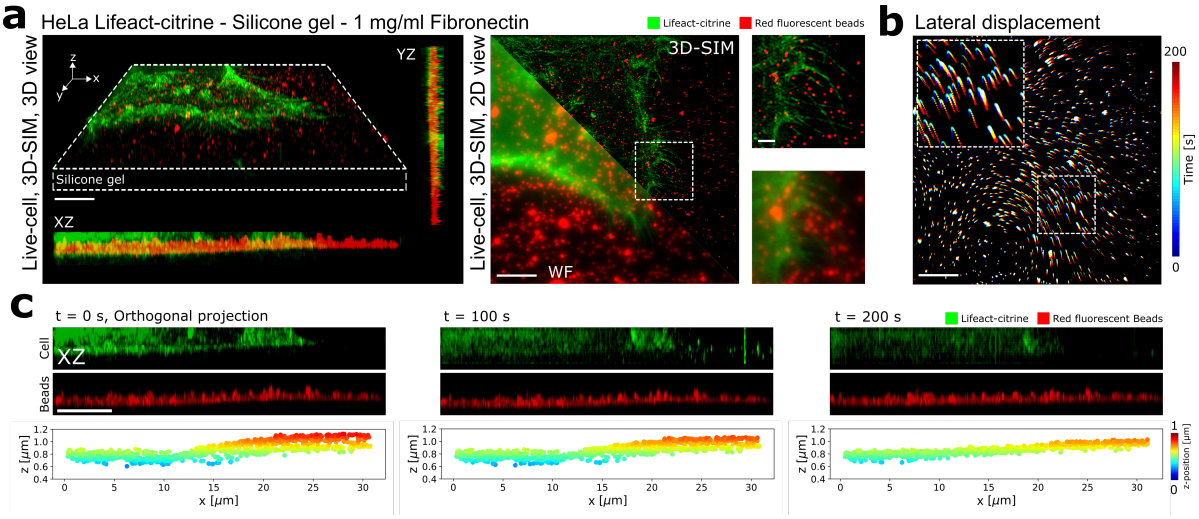



Fig. 4.22 **(a)** Left – 3D and orthogonal rendering of the 3D-SIM stack of an HeLa cell expressing Lifeact-citrine (green) attached to the elastic substrate loaded with fluorescent marker beads (red). Bead density equals to 1 bead per µm$^2$. Right - 2D image focused at the top surface of the silicone gel showing the improved resolution in both HeLa cell and bead images when acquired in 3D SIM compared to WF. Scale bars are 5 µm. Zoom in of the area within the dashed boxed shown adjacently. Scale bar is 1 µm. **(b)** Temporal projection of the lateral bead displacement imaged in 3D SIM, over the total acquisition time of 200 sec. Scale bar is 5 µm. **(c)** Orthogonal projection of the HeLa cell (green) and fluorescent marker beads (red) at time 0, 100 and 200 sec, showing the axial deformation of the elastic substrate within 1 µm range. Scale bar is 5 µm. single particle localisation of the fluorescent beads shown in the lower panel. Image adapted from Coli-York *et al.* [125].

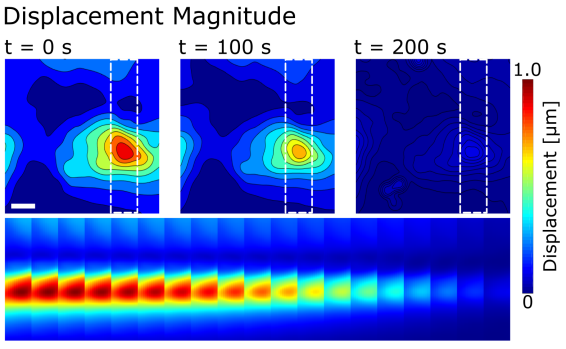



Fig. 4.23 Snap shots of the lateral displacement field over the total acquisition time of 200 sec. Scale bar is 5 µm. Image adapted from Coli-York *et al.* [125].

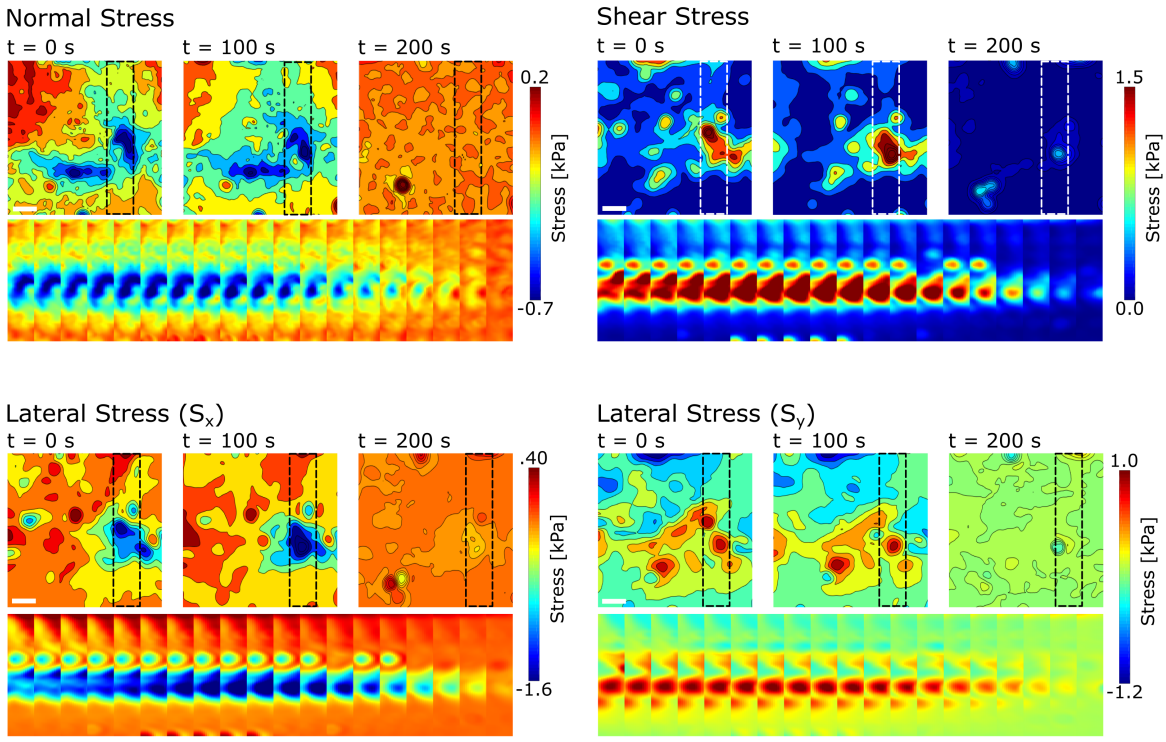



Fig. 4.24 Upper - Snap shots of the normal and shear stress fields over the total acquisition of 200 sec. Lower - lateral Sx and Sy stress fields over the total acquisition of 200 sec. Scale bar is 5 µm. Image adapted from Coli-York *et al.* [125].

molecule localisation microscopy to quantify the 3D position of an emitter relative to the focal plane [187]. By placing a cylindrical lens in front of the camera, the PSF of the emitters, such as fluorescent marker beads in our case, is reshaped according to the position of the beads with regards to the focal plane. Starting as a symmetrical shape when at the focal plane, the PSF of a single bead assumes an elongated shape in the horizontal or vertical direction when its position is above or below the focal plane, respectively. Importantly, the astigmatism effect is sensitive roughly within 1 µm range around the focal plane, capturing axial displacements in the order of ± 600 nm (Fig. 4.25). In addition, this effect can be captured from a standard WF technique, eliminating the need of scanning in z, and therefore introducing a tremendous improvement in the TFM temporal resolution.

To capture fast 3D mechanical forces, we next decided to combine astigmatism with TFM, introducing a new technique called aTFM [134]. The aTFM technique allows 3D sampling with only a single 2D frame acquisition, offering the same temporal resolution of 2D TIRF-SIM-TFM (Table 4.1). The benefit of high temporal resolution impacted also on the acquisition duration time, with more frames acquisition and reduced photo-bleaching effects. However, because aTFM is based on the PSF elongation of the beads to resolve their axial position, the bead density has to be reduced, and therefore the spatial force sampling is reduced. Usually astigmatic imaging is implemented with epi-illumination, a technique that maximises the overall illuminated axial volume above and below the focal plane. However, the combination of this technique with TFM results in a poor contrast of the cell structure on top of the gel surface. To overcome this limitation, we decided to couple astigmatism with TIRF microscopy for imaging the fluorescent beads and TIRF-SIM microscopy for imaging the cell during force generation. The use of TIRF-SIM microscopy minimises the fluorescent background of the cell structure coming from above the focal plane and at the same time increases the resolution of the cellular structures.

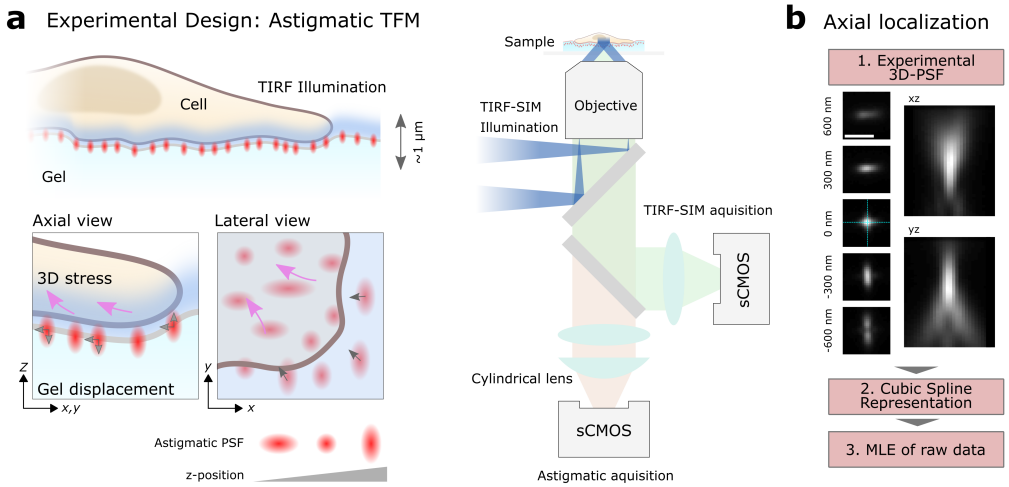



Fig. 4.25 **(a)** Schematic of the aTFM methodology. A single beam with TIRF illumination at the top surface of the gel excites both the cell and the fluorescent marker beads. The TIRF-SIM optical path with two sCMOS cameras in combination with the cylindrical lens permits TIRF-SIM imaging of cellular structures while astigmatic imaging of the marker beads allows extraction of axial positional information. **(b)** Pipeline for the 3D beads localisation in aTFM . First, thanks to the cylindrical lens, the 2D change of the PSF shape of each fluorescent marker bead along the axial direction is acquired. This process is repeated. Scale bar is 1 µm. Next, the PSF shape model is extracted using cubic splines. Lastly, the experimentally acquired PSF model is then compared to the PSF of the raw bead images, using MLE analysis, to extract the z position of the beads. Image adapted from Di *et al.* [134].

aTFM measurements were carried using the silicone gel and 1.49 NA objective. Note, TFM techniques that detect both the lateral and axial displacements having the cell deposited on top of the gel are defined as 2.5D TFM, while TFM techniques where the cell is totally embedded in the gel to measure forces fall into the category of 3D TFM. In the rest of this section, we will adopt the terminology 2.5D TFM to indicate lateral and axial displacements detected thanks to the interaction of a cell on top of an elastic substrate (and not embedded).

### 4.7.2 Calibration of aTFM sensitivity and dynamic range

We started by calibrating the axial position of the beads with respect to their PSF shape, using a silicone gel with sparse fluorescent marker beads. Using a z-piezo scanning, the silicone gel was stepped through the focal plane of the microscope acquiring a 2µm z-stack with 10 nm step size. At each z-position, the 9 raw frame images acquired in TIRF-SIM modality (3 angles and 3 phases) were added together to form a single WF image. Using well-established algorithms [137, 132] the evolution of the lateral PSF shape along the z axis with respect to the focal plane was extracted.

Having the experimentally defined PSF, it was possible to infer the 3D position of the fluorescent marker beads from the raw data acquired during live-cell measurements by performing a Maximum Likelihood Estimation (MLE) (Fig. 4.26). The localisation uncertainty of the MLE was extracted by calculating the ensemble standard deviation of the spatial location of a subset of beads at 100 time points compared to their initial position. The subset of beads was chosen in a way that the region was far from any force generation. We found that when the sub-region selected had only minimal background coming from fluorescence bleed-through from the cell channel, the localisation uncertainty was around 4 nm laterally and 7 nm vertically. The localisation uncertainty increased to 9 nm laterally and 22 nm vertically in the case of higher noise background (Fig. 4.26).

In terms of uncertainty associated to the recovered stress, this is translated into a lateral stress uncertainty of 20 Pa and a vertical stress uncertainty of around 50 Pa for a 10 kPa gel.

Once the system was calibrated, its capabilities were tested using two different cellular systems: the early adhesion of HeLa cells and the immune activation of RBL cells. We decided to use there two systems because they both show mechanical forces in the second time-scale, therefore difficult to be detected using a scanning technique. To allow a visual inspection, correlation between the force generation and the actin structures in the basal plane of the cells was performed. The HeLa and RBL cells were transduced to stably express Lifeact-citrin. Both the cell (Lifeact-citrine, 516 nm excitation, 529 nm emission) and the fluorescent marker beads (580 nm excitation, 605 nm emission) were excited with a 488 nm excitation laser to maximise the acquisition speed.

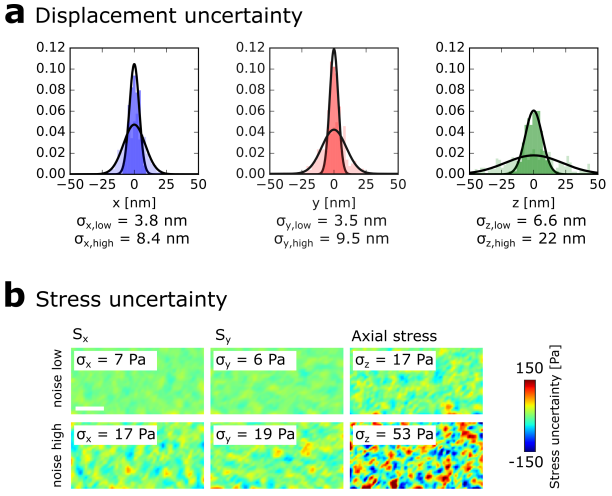



Fig. 4.26 **(a)** Displacement uncertainty estimation extracted using MLE analysis in the lateral x (blue histogram) and y (red histogram) directions, as well as for the axial (green histogram) direction. The displacement uncertainty was calculated from a gel area with and without fluorescent background signal coming from the cell channel. **(b)** Corresponding uncertainty estimation of the lateral (Sx, Sy) and axial (Sz) stresses in the case of a 10 kPa silicone gel with high and low image noise level. Scale bar is 5 µm. Image adapted from Di *et al.* [134].

### 4.7.3 aTFM of adherent HeLa cell

We started first with measuring 2.5D mechanical forces during the early adhesion of HeLa cell. Similar to the 3D SIM-TFM experiments, HeLa cells were let to adhere for 10 min on a 10 kPa silicone gel functionalised with FN and coated with randomly sparse 100 nm red fluorescent marker beads [125] (Fig. 4.27). Using two sCMOS cameras, we could image simultaneously the rapid HeLa cell contacts freshly formed during adhesion on the gel, and the consequent 2.5D bead displacements on top of the gel for a total duration of 100 sec (Fig. 4.28a). For each time point, 18 WF TIRF raw frames were acquired (3 angles, 3 phases, 2 colours channels) using a single excitation beam and a raw frame rate of 9 fps. After imaging, the raw frames were post-processed such that for the bead channel the 9 raw frames were added up to form a WF processed image, while for the cell channel the corresponding 9 raw frames were reconstructed to produce a super-resolved TIRF-SIM image of the cellular structures (Fig. 4.27).

For a more accurate analysis, overlapping beads and beads that could not be tracked during all the acquisition were removed, having at the end a total bead density of 0.3 beads per $\mu m^2$. Next, the *x,y,z* positions of the remaining beads were extracted and linked over time into trajectories. The data were further filtered and the displacement field was then extracted by comparing the bead displacement to the first frame (see Fig. 4.28b and Materials and methods). From the displacement field, we observed a lateral gel retraction towards the cell body, indicating cell contraction during adhesion, with a maximum magnitude of 750 nm. Interestingly, we also observed vertical gel displacement going upwards in the area underneath cell edge and downwards in the areas away from the cell periphery, with magnitude values ranging between -50 nm and 150 nm (Fig. 4.29). Similar results were observed in the work of Legant *et al.* [106] where they show a rotational moment at the periphery of adherent cells. From the displacement fields, both shear (Sx,Sy) and vertical (Sz) stress fields were extracted by

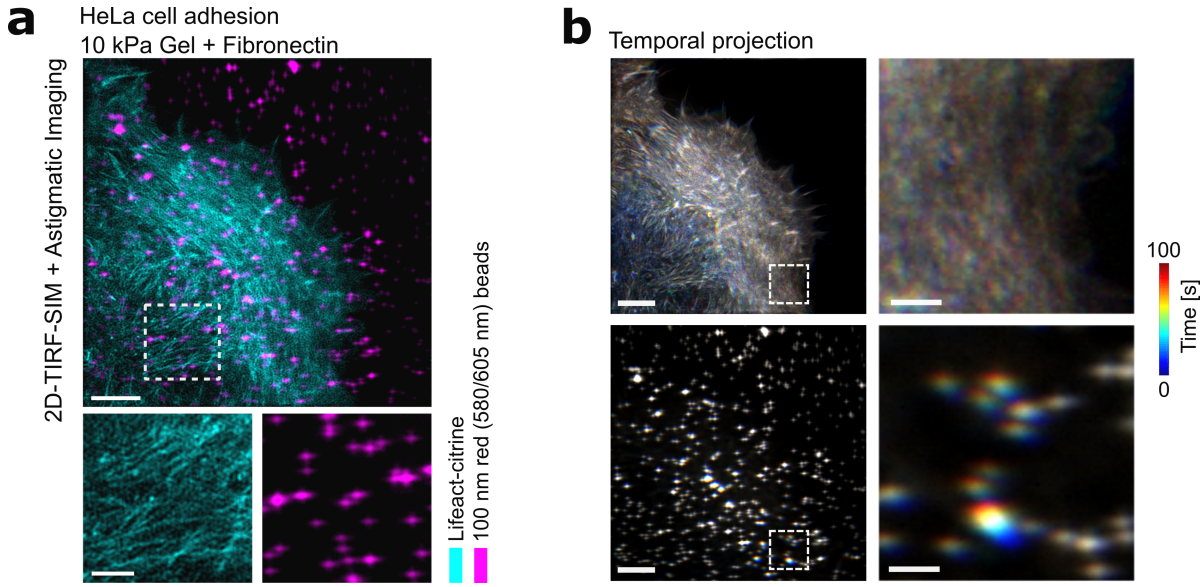



Fig. 4.27 **(a)** TIRF-SIM imaging of a HeLa cell expressing Lifeact-citrine (cyan) adhering to a 10 kPa elastic silicone gel coated with 100 nm fluorescent marker beads (magenta). Image acquired using the aTFM setup. Scale bar is 5 µm. **(b)** Colour coded temporal projections of both the TIRF-SIM cell and the astigmatic bead images over the total acquisition of 100 sec. Scale bar is 5 µm. Zoom in of dashed box has a scale bar of 1 µm. Image adapted from Di *et al.* [134].

our collaborators using FE analysis [134]. The results show a maximum shear stress of 1 kPa and a maximum vertical stress of 0.5 kPa over the total duration of the acquisition (Fig. 4.30). These results demonstrate the capability of aTFM in detecting small vertical displacements below 150 nm and an uncertainty of 22 nm, with a dual-colour frame rate of 1 fps.

### 4.7.4 aTFM of RBL cell activation

Next, we investigated the 2.5D mechanical forces of RBL cells during their activation. Immune cell activation depends on a dynamic cell-cell interaction during which both lateral and vertical forces have been registered in different studies [25, 188, 189]. These forces were shown to influence cell function when perturbing the binding rates between the ligand and the receptor [25, 69, 176]. As for the 2D TIRF-SIM-TFM experiments, RBL

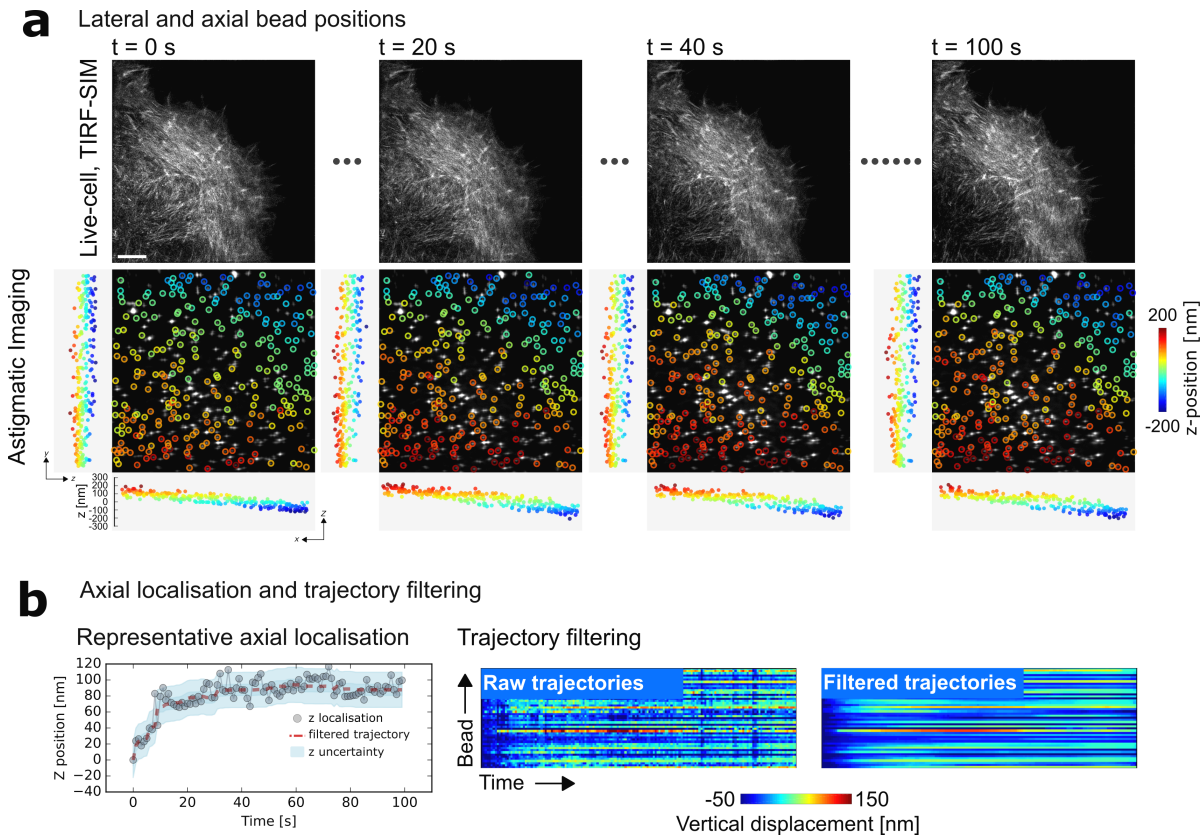



Fig. 4.28 **(a)** Upper - TIRF-SIM snap shots of the HeLa cell over the total acquisition of 100 sec. Lower – Astigmatic bead image overlaid with their lateral localisations (circle) and their color coded axial localisations. The lateral orthogonal projections of the bead positions are additionally plotted. Scale bar is 5 µm. (**b**) Left - Plot showing the axial localisation of a representative raw bead trajectory (grey dots) together with filtered trajectory (red) and localisation uncertainty (blue region). Centre and right - Unfiltered and median filtered trajectories. Image adapted from Di *et al.* [134].

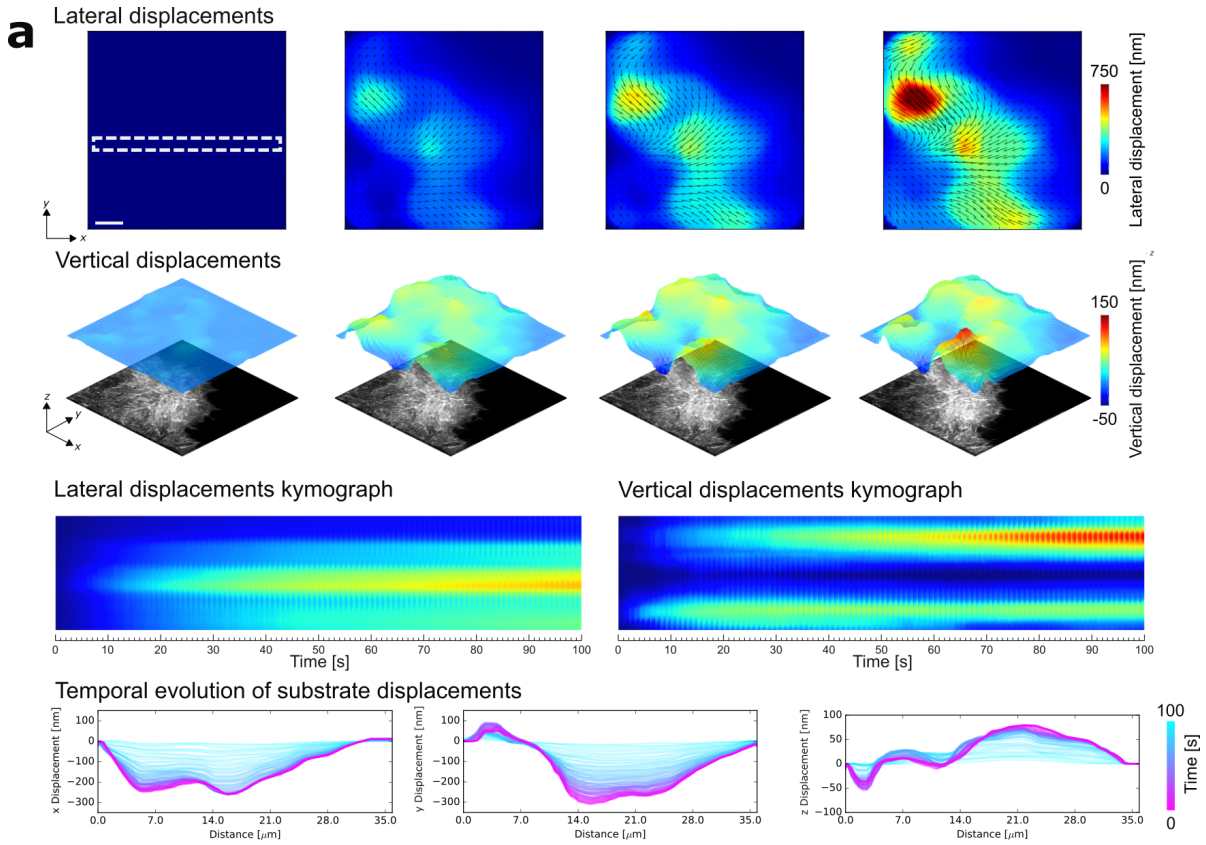



Fig. 4.29 **(a)** Upper - Snap shots of the magnitude of lateral displacements generated during HeLa cell adhesion and surface plots of the corresponding vertical displacement of the gel. The cell image is showed below to facilitate correspondence between the gel displacement and cellular structures. Total acquisition duration of 100 sec. Scale bar is 5 µm. Lower – Kymographs and line plots showing the temporal evolution of the lateral and vertical surface displacements over the total acquisition time of 100 sec. Image adapted from Di *et al.* [134].

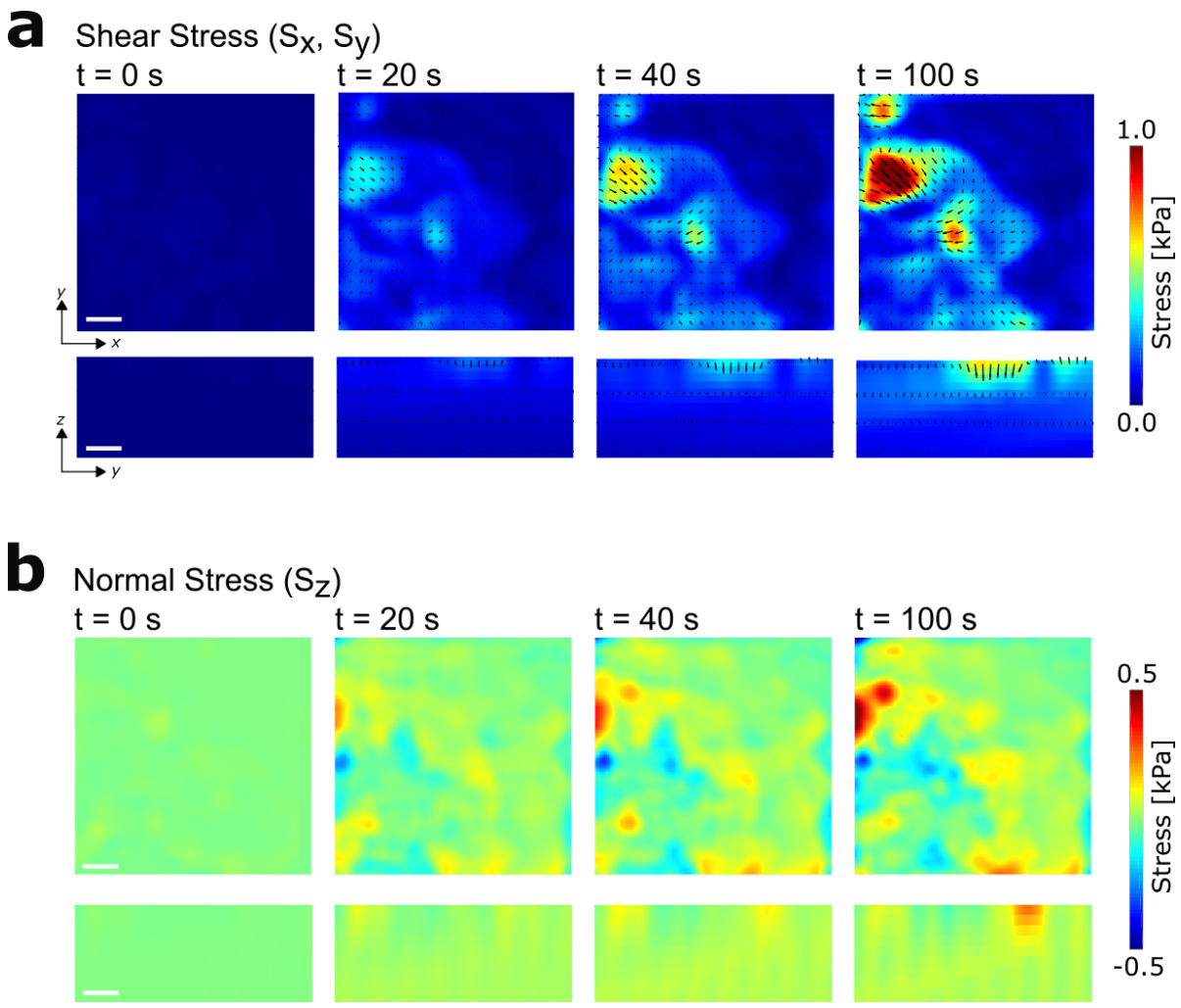



Fig. 4.30 **(a)** Upper - Snap shots of the shear stress field resulting from HeLa cell adhesion. Lower – gel cross section showing the distribution of shear stress through the bulk of the gel. Scale bar is 5 µm. **(b)** Upper - Snap shots of the normal stress field. Lower – gel cross section showing the distribution of normal stress through the bulk of the gel. Scale bar is 5 µm. Image adapted from Di *et al.* [134].

cells were modified to stably express the Fc$\epsilon$ receptor-1 (Fc$\epsilon$RI) and F-actin fluorescently labelled with Lifeact citrine. Their force generation was measured during activation on a 10 kPa silicone gel functionalised with the Fc$\epsilon$RI-specific antibody IgE and coated with red 100 nm fluorescent marker beads at a density of 0.3 beads per $\mu m^2$. As for the HeLa cells, only the 488 nm excitation laser was used to illuminate in TIRF-SIM mode the cell structures and in astigmatic WF mode the beads on top of the gel substrate. RBL activation was imaged for 100 sec with a dual-colour frame rate of 1 fps (Fig. 4.31a,b). A later radial spreading of the cell was observed over the entire acquisition with a maximum displacement value of 150 nm (Fig. 4.31c). Interestingly, the results showed small vertical displacements constantly formed by fresh adhesion sites at the ventral interface of the cell, together with a global cell contraction after cell spreading with a maximum displacement value of 150 nm (Fig. 4.31c). The vertical displacement could be visually correlated with the dynamic change of overall RBL F-actin architecture shown by the bright sub-diffraction actin patterns, suggesting mechanical change over time in the actin network [190, 17].

From the displacement field, the stress field was extracted using FE calculations. Figure 4.32 shows an increasing in the shear (Sx,Sy) stress during RBL cell activation and spreading, with a maximum magnitude of 0.25 kPa, and a maximum vertical stress (Sz) of 0.15 kPa. This result suggests that the shear mechanical force generated by RBL cells during their activation are on the same order of magnitude as the vertical mechanical force (Fig. 4.32).

### 4.7.5 Summary

In this section, I have described how to measure 3D mechanical force with high temporal resolution by combining TFM, astigmatic imaging and the super-resolution SIM microscopy. Placing a cylindrical lens in front of the camera, the PSF shape of the beads

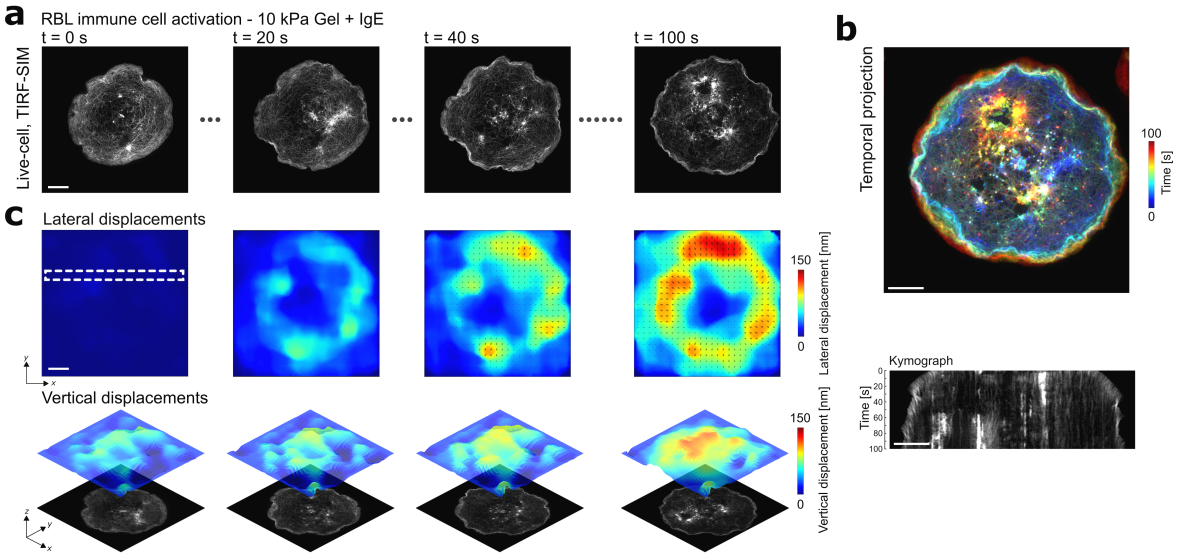



Fig. 4.31 RBL cell activation on a silicone gel with aTFM. **(a)** Snap shots of the RBL cell while activating on a 10 kPa gel. Scale bar is 5 µm. **(b)** Temporal projection of the RBL activation evolution during the total acquisition time of 100 sec. Scale bar is 5 µm. **(c)** Upper - Snap shots of the displacement field during the total acquisition time of 100 sec. Scale bar is 5 µm. Lower - cross section of the gel showing the vertical displacement of the cell during the total acquisition time of 100 sec. Cell profile plotted underneath to help with the visualisation. Image adapted from Di *et al.* [134].

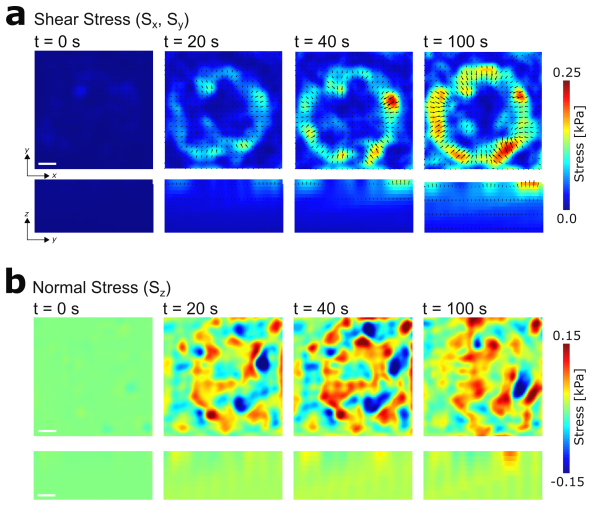



Fig. 4.32 **(a)** Upper - Snap shots of the RBL cell shear stress field during its activation. Lower - gel cross section showing the distribution of shear stress through the bulk of the gel. Scale bar is 5 µm. **(b)** Upper - Snap shots of the RBL cell vertical stress field during its activation. Lower - gel cross section showing the distribution of vertical stress through the bulk of the gel. Image adapted from Di *et al.* [134].

is modified according to their axial position with respect to the focal plane. From a single 2D image, the *x,y,z* positions of the beads were extracted, and small shear and normal forces in the order of 0.5 kPa were recovered with a frame rate of 1 fps, comparable to the acquisition speed achieved with 2D TIRF-SIM-TFM. Fast imaging speed was obtained by precluding the need of scanning in the axial direction, which minimises the photo-toxicity induced to the cell. In addition, the system calibration showed a lateral localisation uncertainty of 9 nm and a vertical uncertainty of 22 nm, consistent with 3D super-resolution localisation microscopy [187]. The technique was validated measuring the shear and normal force generation during early adhesion stage of HeLa cells and during immune activation of RBL cells. For the HeLa cells, the shear stress was an order of magnitude higher than the normal stress (Sz = 0.1 - 0.5 kPa, 100 – 500 pN/$\mu m^2$, Sx,y = 0.5 - 1 kPa, 500 – 1000 pN/$\mu m^2$). For the RBL cells, comparable shear and normal stresses were registered (Sz = 0.01 - 0.15, 10 – 150 pN/$\mu m^2$, Sx,y = 0.01 - 0.25 kPa, 10 – 250 pN/$\mu m^2$).

The localisation uncertainty could be further improved decoupling the excitation for the cell and beads channels, illuminating the sample with two laser beams at different wavelengths, however reducing the overall frame rate by a factor of two. Currently aTFM can measure forces in the axial direction within a dynamic range of 2 µm around the focal plane. To increase further this range, astigmatism imaging can be combined with piezo z-scanning, however compromising again the current acquisition speed. Other forms of optical deformations of the bead PSF can be adopted as well, such as double-helix or biplane imaging [191, 192]. Future advances targeting an improvement of the lateral spatial resolution in the presence of high bead density, while maintaining the axial information given by aTFM, would be based on image analysis algorithm to extract additional spatial information [103, 193].

# Chapter 5

# Establishing an automated single-cell high-throughput $Ca^{2+}$ platform

In this chapter, I present a novel methodology that we developed to quantify automatically and simultaneously immune cell activation traces with the potential to image 100,000 live cells with spatio-temporal information, using a combination of machine learning data analysis and light-sheet imaging. First, I give an overview of the concepts and theory behind CNN. Next, I discuss the current technologies for $Ca^{2+}$ signalling and activation markers reads-out with their advantages and disadvantages. To overcome these limitations, we developed a novel biophotonic optical platform consisting of a CNN based CalQTrace software and a large 4 mm $\times$ 3.5 mm FOV light-sheet hardware, to track $>$ 20,000 live T-cells in space and time with single-cell resolution, sort cells based on surface proteins expression, and automatically classify their $Ca^{2+}$ signalling traces. Using CalQTrace software, I show that $Ca^{2+}$ signalling can be correlated with the strength of T-cell activation, and consequently linked with force generation and surface proteins expression to investigate mechanobiology during T-cell activation.

- This study is the result of a collaborative work between the University of Oxford and The Arctic University of Norway. Several people contributed to this work. In particular:

  - I developed the CalQTrace software, and performed the biological experiments and data analysis. The cell spreading assay was a collaborative effort between myself, a master student Gabrielle Chappell I supervised during my PhD, and Dr. Narain Karedla.
  - Dr. Isabela Pedroza-Pacheco gave us the primary human T-cells.
  - Dr. Aurelien Barbotin developed the GUI for the software.
  - Dr. Kseniya Korobchevskaya, Dr. Azeem Ahmad and Veronika Pfannenstill designed and built the large FOV light-sheet microscope.
  - Dr. Kseniya Korobchevskaya, Veronika Pfannenstill and myself designed the PDMS chamber for imaging. The chamber was fabricated by J. Prentice and the Department of Oncology Workshop (Oxford, UK).

## 5.1 Machine learning based technology

Machine learning based technologies have become extremely powerful in the medical science field to process large datasets to recognise and classifies patterns, from text files to images. In the microscopy field, a new advanced form of machine learning called Deep Neural Network (DNN) is used to identify objects within images in a robust and user-independent way [194]. DNNs comprise of the same fundamental building blocks, even if built with a more complex structure, as ordinary Neural Networks with the property of distinguishing and recognising different inputs (e.g. images of cats and dogs). The structure takes inspiration from the real neural network, which consists of 'neurons'

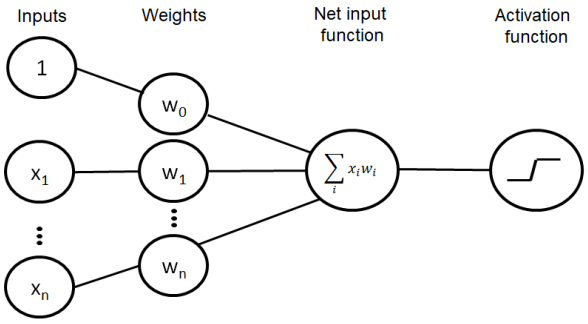



Fig. 5.1 Schematic representation of a perceptron: the simplest artificial neural network. Reading from left to right, n-inputs ($x_1$, ..., $x_n$) and the bias, always equals to 1, are multiplied by their respective weights (randomly initialized). All the products are then added together. The sum, then, is sent to an activation function that modulates the output that will travel the network.

that have learnable weights and biases. Artificial neural networks are made by weights, biases and activation functions, which allow the signal to go through the entire network. To give a general idea of how it works, Figure 5.1 shows the most simple artificial neural network, called a 'perceptron'.

The perceptron consists of inputs, a bias, a net input function and an activation function. The inputs ($x_1$, ..., $x_n$) and the bias (always equal to 1), are multiplied by weights ($w_1$, ..., $w_n$) before going into the neuron, hence we can consider the bias like a first input with a value of 1. The sum of all these products, called the net input function, is sent to an activation function. The net input function is defined as following:

$$y = b + \sum_i x_i w_i, \tag{5.1}$$

where y is the output, b is the bias, $x_i$ are the inputs and $w_i$ are the weights. The aim of the activation function is to define the type of output (signal) that has to pass through the network. Usually there are linear and non-linear activation functions. In more complex systems, neurons are typically organised in layers and the signal that is transmitted goes from the first layer (called input) to the last (called output) in a forward

way. These networks are called feed-forward networks. Feed-forward neural networks are by default supervised methods, that is, the correct output answer for each input is known *a priori*. Hence, it is possible to know if the network, at the end of the process, made a correct guess or not computing an error function [142].

### 5.1.1 Convolutional Neural Network

CNN are examples of feed-forward neural networks. CNN networks consist of multilayer perceptrons (MLP), with some fundamental additional characteristics, that through non-linear transformation classify different objects. The additional characteristics are: N-D volume of neurons (where N is the dimensionality of the input data) within a layer, which is connected to the previous one through a small region, a local connectivity that uses filters to produce a response from a spatially local input pattern, and shared weights among copies of the same filter [194]. About the last characteristic, each filter is replicated to cover all the input field, and each replica shares the same weights and bias forming the so called feature map [195]. For multi-layers networks, non-linear activation functions are used. The input space cannot, in fact, be directly linearly classified. Hence, first non-linear transformations have to be applied in order to obtain an output space in which the features can be linearly separated (see Fig. 5.2) [142]. In this work we will use a conventional supervised feed-forward CNN.

Conventional CNN algorithms are method that 'learn' how to classify inputs. Given a certain number of classes, and knowing *a priori* which curve belongs to which class, what a supervised CNN algorithm does is that it learns how to adjust its weights to let a certain curve pass through specific activation functions in order to classifying them. In particular, the CNN takes each of the pixel values within one curve, and considers it as a single input. Let us consider the case of a calcium intensity trace as a 1D array of pixels in time. The total number of inputs will be equals to the length of the calcium intensity curve.

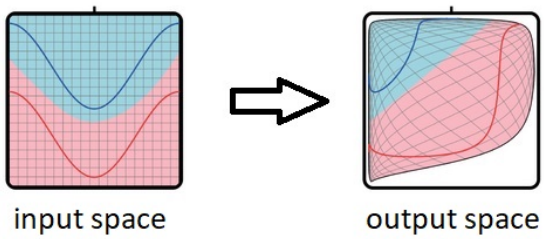



Fig. 5.2 Representation of a non-linear transformation. The figure shows two different regions (the red and the blue) non linearly separable. The result, after a non-linear transformation is that the regions can be linearly separated. Figure adapted from [142].

The sum of all the products between pixels and weights is then sent to several neurons (equivalent of perceptrons). The neurons will 'fire' or not depending on the particular activation function. This mechanism allows to filter unique characteristics that makes it possible to distinguish between different $Ca^{2+}$ intensity traces, such as single-peak, oscillatory and non-triggering [78]. If the outputs of the classification are wrong (we know *a priori* the result), it is possible to repeat the process with the next internal iteration, called an 'epoch'. During each epoch, the algorithm will adjust the weights (learning procedure) going back and forth through all the network, until the outputs will all be corrected. The weights, which are at the beginning randomly initialized, are adjusted such that they minimise the loss function (called also 'objective function'). The loss function is calculated between the predictions and the ground-truth classifications and is given by:

$$Loss = \frac{1}{2n}\Sigma(t_i(\mathbf{x}, \mathbf{w}) - y_i)^2 \tag{5.2}$$

where $n$ is the number of training data and $t(x,w)$ and $y$ are the predicted values of the CNN and the ground-truth classifications, respectively. The term 'ground truth' refers to the manually labelled data. The predictions are the classifications obtained by running the CNN with testing data. Overall, a CNN is always trained and evaluated

with two completely independent datasets: the training dataset and the test dataset. The accuracy of the CNN is obtained by comparing the ground truth classifications and the prediction classifications. From this point, we will refer to the 'prediction accuracies' as 'predictions'.

In addition to the training and testing, it is possible to perform an evaluation of a CNN algorithm. The evaluation can be included during the training part and consists in verifying if the parameters selected in the algorithm are most suitable for the classification of a certain type of data. This evaluation is made by using a fraction of the training data as 'validation data'. The validation data has the same role of the testing data but, usually, it is a smaller dataset to avoid a slowing down of the training CNN part. Two other important parameters to describe a CNN are epochs and 'batches'. As mentioned before, a CNN is ran for a certain number of epochs, where each epoch represents one forward pass and one backward pass through all the training examples. For each epoch, it is possible to divide the total number of training data in batches and go forward and backward in the network as many times as the number of batches, in order to train the CNN with all the training data. At then end of the whole process, the outputs will give the accuracy of the CNN with the training, validation and testing datasets and the loss functions calculated between validation and training data and testing and training data. In the end, the overall goal consists in training the CNN in order to obtain a loss function as close to zero as possible.

### 5.1.2 Learning rate optimisation

Several procedures that optimise the learning exist. One of the most popular procedure is the so called 'gradient descent'. The gradient descent is an algorithm that updates the weights by using a back propagation method in order to calculate the gradient of the loss function with respect to the weights and find the minimum of the function [194, 195].

This method is quite efficient and is commonly used, but has some disadvantages. In particular, the most problematic issue of gradient descent is that if the form of the loss function is a long shallow ravine leading to the optimum, with steep walls on the sides, the value of the optimized loss function, and therefore the weights, will oscillate across the ravine. [142]. Therefore, in the CNN algorithm here presented, a state-of-the-art optimizer of gradient descent called ADAM is used. The core principle behind the optimizer ADAM is in getting rid of this issue by choosing carefully the step-size used in the gradient descent method in order to reach the minimum of the loss function [145]. Commonly, the step-size depends on a parameter called 'learning rate'. In ADAM, the learning rate value is scaled by the ratio of others two parameters that are the first and second moment of the gradient (that is the mean and the variance, respectively). This ratio behaves like a Signal-to-Noise-Ratio (SNR). Below the step-size according to ADAM:

$$\Delta_t = \alpha \widehat{m}_t / \sqrt{\widehat{v}_t} \tag{5.3}$$

where $\alpha$ is the learning rate, and m and v are the first and second momentum respectively. A smaller SNR, for example, means that there is grater uncertainty about where to go next (that is we are in the presence of an optimum) and therefore the effective step-size will be closer to zero.

### 5.1.3 The overfitting problem

Lastly, a big issue with non-linear layers in CNN is overfitting. In particular, when a CNN is trained with limited amount of data, it can lead to a situation where the model tries to learn how to describe random errors or noise, instead of the main relationships among the inputs. In such a scenario, the validation loss function plays an important role in indicating if there is any overfitting: if the validation loss value increases while

the training accuracy decreases, there is probably overfitting. Several methods can help to prevent overfitting, such as dropping an optional layer, called the Dropout layer in the network.

## 5.2 Overview of $Ca^{2+}$ and activation markers quantification

The well-orchestrated sequence of events in space and time during T-cell activation is crucial for the immune system's response against an invading external organism, such as a virus, or cancers. The success of this process relies on environmental cues, the dynamic interaction between T cell and the local biophysical environment at various length- and time-scales, the binding of surface molecules, and the signalling events leading to effector function. During the activation of T cell upon interaction with the local biophysical environment, such as an APC, $Ca^{2+}$ flux is released within a few seconds from the ER [196, 46, 197], immediately followed by the actin cytoskeletal rearrangement and maintenance of the IS over minutes [29, 198]. After few hours, the expression of surface proteins, used as activation markers, enables the differentiation of effector T-cells [5, 199, 200].

Over the past years, quantification of $Ca^{2+}$ signalling and activation markers has been extensively performed and these characteristics have been used as readouts [39, 201–203, 77]. Because of its fast dynamics, taking place a few ms after the TCR-pMHC binding and lasting up to a few minutes to hours, $Ca^{2+}$ signalling is commonly used as an early activation marker [15, 204]. Recent work has been shown three main types of $Ca^{2+}$ signalling responses during T-cell activation: single-peak (single $Ca^{2+}$ burst), oscillatory (multiple $Ca^{2+}$ release cycles over time) and non-triggering (absence of $Ca^{2+}$ release) [121]. On the other hand, surface proteins, such as CD25, are commonly used to

report the level of T-cell activation and differentiation on a time-scale that spans over a few hours. [205].

## 5.3 Need for methodology development

As mentioned in the Background chapter, a variety of technologies are currently available for $Ca^{2+}$ signalling and activation markers quantification [112, 114, 115, 118, 119, 121, 78, 122, 123]. Within the context of mechanobiology, where the spatial information is considered a crucial component for T-cell activation studies, live-cell fluorescence imaging techniques for $Ca^{2+}$ measurements are considered superior over the FC based approaches [114, 115]. Indeed, fluorescence-based optical imaging tools have the advantage to provide both spatial and temporal information of T-cell activation during engagement with the external local biophysical environment, at single-cell resolution [206]. This cannot be achieved in an FC experiment, where only ensemble information of T-cell activation at distinct time points are acquired and no spatial knowledge is achievable [113].

Even though there are significant advantages of fluorescence microscopy methods over the FC approach, existing challenges restrict a robust and quantitative $Ca^{2+}$ signalling analysis. Contrary to FC, fluorescence microscopy does not offer multi-dimensional analysis with high statistical power. In a typical FC experiment, up to 20 different activation markers, labelled such that they can be discriminated spectrally, can be analysed over a large ($10^5$) cell population, increasing up to 100-fold the statistical power compared to the current microscopy techniques which have about a maximum of $10^3$ cells per FOV [207, 123, 124, 122]. In addition to the imaging modality, a major challenge lies in making the analysis of $Ca^{2+}$ signalling responses acquired with a fluorescence microscope robust and automated. [109, 79]. Previous work that made an effort to standardise the analyses of $Ca^{2+}$ signalling traces extracted within each T cell during activation, are based on the development of new software packages such as CalQuo and

CalQuo2 [121, 78, 208]. However, these softwares, based on Fourier-space analysis and high-dimensional parameter choice, necessitates high-level user expertise, making the process time consuming and not statistically robust due to the different users level and choices [121, 78]. On top of that, these software packages do not offer cell tracking, and activation markers and viability quantifications.

Recently, new advances in fluorescence microscopy and large sensor acquisition cameras, as well as automated data analysis, opened up to new technological developments with statistical power and high spatio-temporal sensitivity. In particular, the new light-sheet microscopy technology offers extended FOV imaging with a gentle amount of excitation laser power, preserving biological samples from phototoxicity [209–213]. In parallel, the most recent sCMOS camera models with large sensors and high pixel density are ideal for large FOV acquisition with high spatial and temporal resolution. Finally, using machine learning based methodologies and in particular, the development of CNN based algorithms, extensive progress has been made in realising software automation for data and image analysis and classification. Although using a CNN algorithm means the absence of user control over analytical approaches for data manipulation, with the well-known black box effect, and the need of training the model with multiple experimental conditions, it also offers many advantages: (i) reproducibility and robustness of data analysis; (ii) automatisation of data analysis with the consequent reduction of the total number of free parameters; (iii) rapid analysis for large amounts of data.

Overall, the combination of automated data analysis with an extended light-sheet microscopy offers a new potential methodology to overcome previous limitations in $Ca^{2+}$ signalling and activation markers measurements and classification. The high statistical power together with the spatio-temporal information and automated analysis can be an asset for studying the mechanobiology of T cells in the physical biophysical

environment, offering high sensitivity reads-out for complex and heterogeneous immune cell responses [214, 215].

In this work, we established CalQTrace, a machine learning based user-friendly software for $Ca^{2+}$ signalling, cell viability and activation markers measurements. Based on a supervised 1D CNN algorithm, CalQTrace can detect and track thousands of T cells in space and time during activation. It can exclude and sort sub-populations of cells, and classify with single-cell resolution $Ca^{2+}$ signalling responses into the three main categories of single-peak, oscillatory and non-triggering. To make it user-friendly, we implemented the software within a GUI. Combining CalQTrace with the high resolution CSD microscope, we show preliminary results that suggests a difference in $Ca^{2+}$ signalling responses in pre-activated ($CD25^{+}$) and resting ($CD25^{-}$) primary human $CD8^{+}$ T-cells. Intrigued by these results, we performed experiments using the 1G4 Jurkat T-cells model during their activation to investigate upon different antigen affinities to the 1G4 TCR. By analysing simultaneously $Ca^{2+}$ signalling responses and IS spreading, we show a correlation between the different types of $Ca^{2+}$ intensity trace and immune activation strength and stability. Finally, to extend the statistical power in the direction of FC standards, we developed a large 4 mm $\times$ 3.5 mm FOV light-sheet upright microscope. Coupling the large FOV light-sheet with CalQTrace, we present preliminary experiments where we could track in space and time and measure $Ca^{2+}$ signalling responses of $>$ 20,000 living T-cells during their activation, maintaining single-cell resolution.

The CalQTrace software together with the large FOV light-sheet microscope offers a new technology for quantifying the strength of T-cell activation upon interaction with the external biophysical environment, offering new insights into the mechanobiology field due to the ability to analyse both readouts of mechanics and signalling.

## 5.4 Development of CalQTrace software

### 5.4.1 Software pipeline

We first started with the development of the CalQTrace software. CalQTrace is a Python based user-independent software that detects and tracks simultaneously thousands of T cells in space and time and automatically classifies with single-cell resolution their $Ca^{2+}$ signalling traces into single-peak, oscillatory and non-triggering responses. On top of this, the platform can analyse multiple colour-channel images to then exclude and sort any sub-population through imaging-based methods. CalQTrace can be run by loading an 8-bit image stack of cells flashing $Ca^{2+}$, acquired at any fluorescence microscope (see Materials and methods). As an optional analysis, two single-frame datasets, each of them registered in a separate colour channel at the end of the $Ca^{2+}$ acquisition, can be loaded to exclude and sort sub-populations of T cells (see Fig. 5.3). As a preliminary validation of the CalQTrace capabilities, we decided to investigate $Ca^{2+}$ signalling of 72 hrs pre-activated $CD25^+$ and resting $CD25^-$ primary human $CD8^+$ T-cells when activated with the OKT3 antibody and the ICAM-1 adhesion protein (see Materials and methods). The data were acquired using the Zeiss CSD microscope, equipped with the Hamamatsu ORCA-Flash4.0 v2 sCMOS camera and a 4× air objective.

After being pre-activated in solution with Dynabeads for 72 hrs (see Materials and methods), primary human $CD8^+$ T-cells were labelled with three dyes: Fluo-4 for internal $Ca^{2+}$ staining, PI for marking dead cells, and anti-CD25-APC-R700 antibody for labelling $CD25^+$ cells. While both Fluo-4 and PI are intracellular markers, anti-CD25-APC-R700 is an external membrane marker (see Fig. 5.3). First, an image stack of 1,000 frames at 800 ms exposure time was acquired in the $Ca^{2+}$ channel, with a total time length of 13 min ($t_N$). At the end of the $Ca^{2+}$ acquisition, a single frame was acquired in both dead and $CD25^+$ channels. The data were then loaded into the CalQTrace software. A GUI

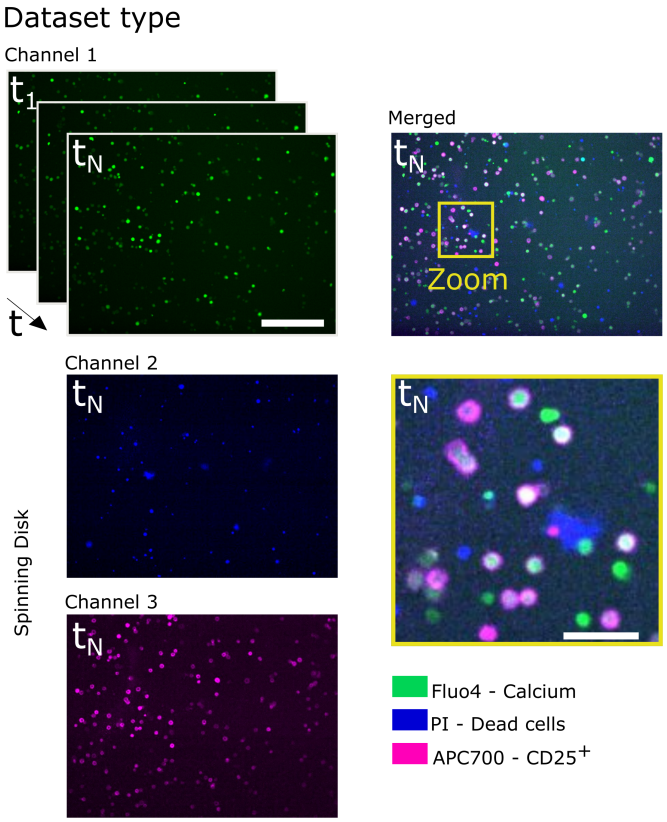



Fig. 5.3 Example of the dataset type analysed with the CalQTrace software. Left - Three-colour channel dataset. Channel 1 shows a sequence of 2D (x,y) frames of $Ca^{2+}$ labelled cells (green) acquired sequentially over time. Channel 2 and 3 are two separate single-frame images acquired at the end of the $Ca^{2+}$ acquisition, showing dead cells labelled with Propidium Iodide (blue) and $CD25^{+}$ cells labelled with the anti-CD25-APC-R700 antibody marker (magenta), respectively. Right - superimposition of all three channels together (using the last frame for the $Ca^{2+}$ channel), and zoomed view below (yellow box). Scale bars are 200 µm and 50 µm.

was built to make it user-friendly (see Fig. 5.4). The GUI consists of five tabs, each one running a specific software section, called 'cell detection', 'exclusion', 'separation', and 'intensity extraction and classification' (see Fig. 5.4). The exclusion and separations tabs are optional sections used for removing and or sorting a sub-population of cells, in this case dead cells and $CD25^{+}$ and $CD25^{-}$ cells respectively.

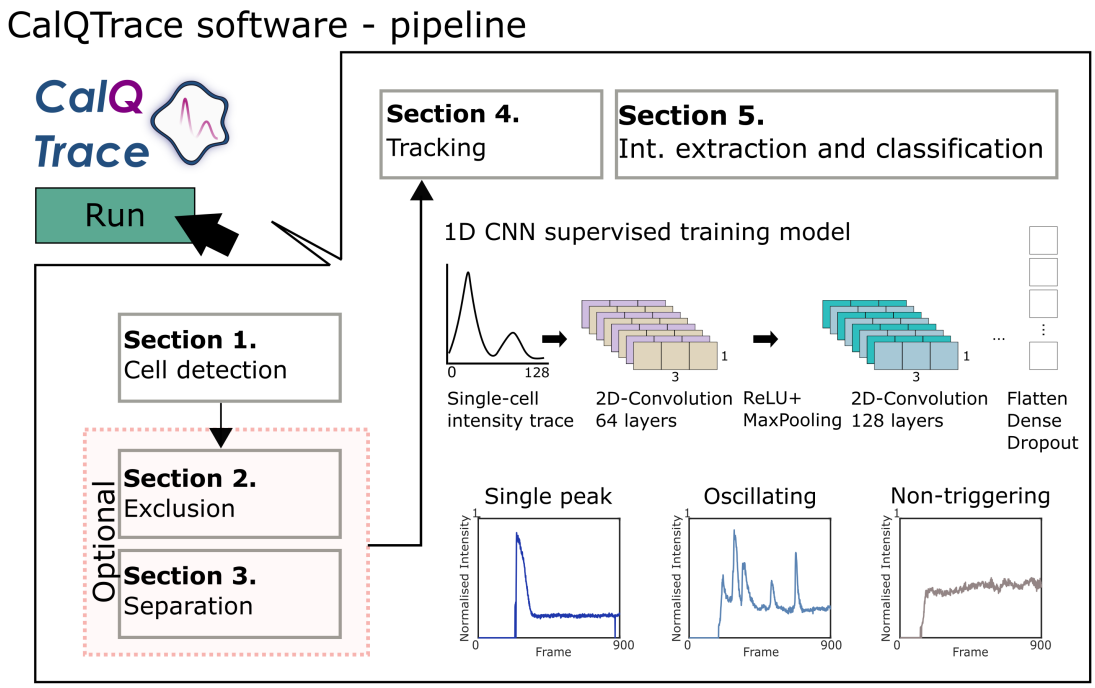



Fig. 5.4 Schematic of the CalQTrace software. CalQTrace is a user-friendly software integrated into a GUI. It consists of 5 sections for cell detection, exclusion and separation (optional), cell tracking and $Ca^{2+}$ intensity extraction and classification. The classification, based on a supervised 1D CNN model, to distinguishes $Ca^{2+}$ signalling intensity traces in single-peak, oscillatory and non-triggering responses.

**Cell detection** In the first section, the $Ca^{2+}$ channel was loaded (Fig. 5.5a). All cells, within the FOV of each image stack, are detected selecting two inputs, the minimum cell brightness and cell diameter (see Materials and methods). Each detected cell is marked

with a red circle positioned at its centre of mass (see Fig. 5.5a). The parameters can be fine tuned to find the optimal detection parameters.

**Cell exclusion and separation** In the second section called 'exclusion', dead cells are detected and excluded from the analysis using imaging co-localisation. After loading, the dead cells in the single frame was segmented (see Materials and methods). The segmented image was next used to determine cells that were dead in the last frame of $Ca^{2+}$ image stack so that they can be excluded from the analysis (see Fig. 5.5b, and Materials and methods). Live $Ca^{2+}$ cells were marked with a cyan circle, while dead cells were marked with a magenta x (see Fig. 5.5b). The third section is called 'separation'. A similar method used in the exclusion section is applied, but this time to separate $CD25^{+}$ from $CD25^{-}$ T-cells. Both exclusion and separation sections are optional one (see Fig. 5.5c and Materials and methods).

After being detected in space in each of the frames of the $Ca^{2+}$ stack, cell coordinates are linked in time to build trajectories (see Fig. 5.6a, and Materials and methods). Each colour line represents a single cell tracked in space and time. The tracking was performed using the Trackpy Python library [138] (see Materials and methods). Three parameters are required from the user for the tracking step: the minimum tracking length, search range and memory (see Materials and methods). In the final section, called 'Intensity extraction and classification', the $Ca^{2+}$ signalling intensity from each cell is extracted over time and classified with a custom-made deep learning model into the three major responses that are single-peak, oscillatory and non-triggering (see Fig. 5.6b and Fig. 5.4, and Materials and methods). We used a 1D CNN model for automated machine learning classification trained with the 1G4 Jurkat T-cells line and primary human PBMC T-cells, which had an overall prediction accuracy of $> 90\%$ (see Fig. 5.7 and Materials and methods). The tracking of each individual cell and its own $Ca^{2+}$ intensity trace can be displayed for inspection, to validate the overall analysis (see Fig. 5.6b).

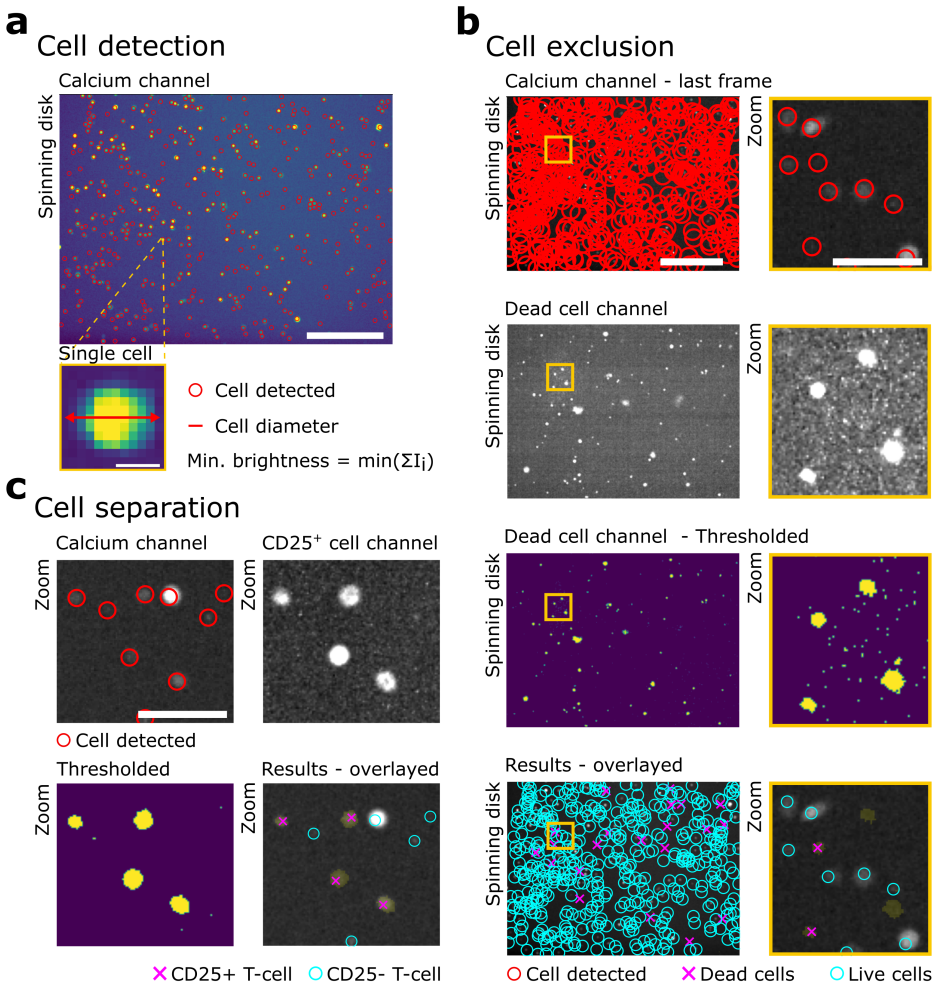



Fig. 5.5 CalQTrace software: cell detection and exclusion. (**a**) Cell detection. Single frame showing cell detection (red circle) and single-cell zoom-in. The cells are detected tuning the 'cell diameter' and 'minimum cell brightness' parameters. Scale bars are 200 µm and 8 µm respectively. (**b**) Cell exclusion. Top - Single frame from the $Ca^{2+}$ channel acquired at t = 13 min showing cell detection (red circle) and zoom-in. Middle top - Single frame from the dead cell channel acquired immediately after t = 13 min, and zoom-in. Middle lower - Dead cell frame binarised using thresholding. Lower - Single frame acquired at t = 13 min showing the result of dead cell exclusion (magenta x) from the $Ca^{2+}$ channel (cyan circle). Scale bars are 200 µm and 50 µm respectively. (**c**) Cell separation. Top left - Zoom-in of a single frame from the $Ca^{2+}$ channel acquired at t = 13 min showing cell detection (red circle). Top right - Zoom-in of a single frame from the $CD25^+$ channel acquired immediately after t = 13 min. Bottom left - Zoom-in of $CD25^+$ cell frame binarised using thresholding. Bottom right - Single frame acquired at t = 13 min showing the result of $CD25^+$ (magenta x) and $CD25^-$ (cyan circle) cell separation from $Ca^{2+}$ channel. Scale bar is 50 µm.

From the CalQTrace analysis we could observe a higher percentage of single-peak and oscillatory $Ca^{2+}$ responses within the pre-activated $CD25^+$ sub-population compared to the resting $CD25^-$ primary human $CD8^+$ T-cells. Specifically, among the $CD25^+$ primary human $CD8^+$ T-cells, 33% shown a single-peak $Ca^{2+}$ activation, 40% an oscillatory response and 27% non-triggering, as shown in the heatmaps diagrams (see Fig. 5.6c). Among the $CD25^-$ primary human $CD8^+$ T-cells, only 16% were single-peak responses, 12% oscillatory and the rest majority were non-triggering (see Fig. 5.6)c.

### 5.4.2 $Ca^{2+}$ response might predict T-cell activation strength

Previous works [78] has shown that percentage of the three main $Ca^{2+}$ categories change when T cells are activated with different antigen affinities. Specifically, they used genetically modified Jurkat T-cells expressing the 1G4 TCR which binds specifically to the NY-ESO-$1_{157-165}$ peptide. The 1G4 Jurkat T-cells were activated upon interaction with two variants of this peptide, named the 9V and 4D, whose affinity to the 1G4 TCR was high in the case of 9V and low in the case of 4D. For the 4D antigen mostly non triggering and oscillatory $Ca^{2+}$ traces were observed, while for the 9V antigen higher percentage of single-peaks were detected [78].

Equipped with the new automated CalQTrace software, we inquired the significance of the different $Ca^{2+}$ responses observed in the previous work and also in our preliminary experiment with the primary human $CD8^+$ T-cells. In particular, we interrogated whether there was a correlation between the different $Ca^{2+}$ signalling traces and the IS formation. To do so, we decided to reproduce the Lee *et al.* [78] experiments but this time adding the cell contact area information during activation. Similar to the Lee *et. al* work, Jurkat T-cells expressing the 1G4 TCR were stimulated using the 9V and 4D peptides, and the anti-CD3 antibody, defined as OKT3. Their affinity to the 1G4 TCR, defined as the strength of the interaction between the antigen and receptor, follows the following trend:

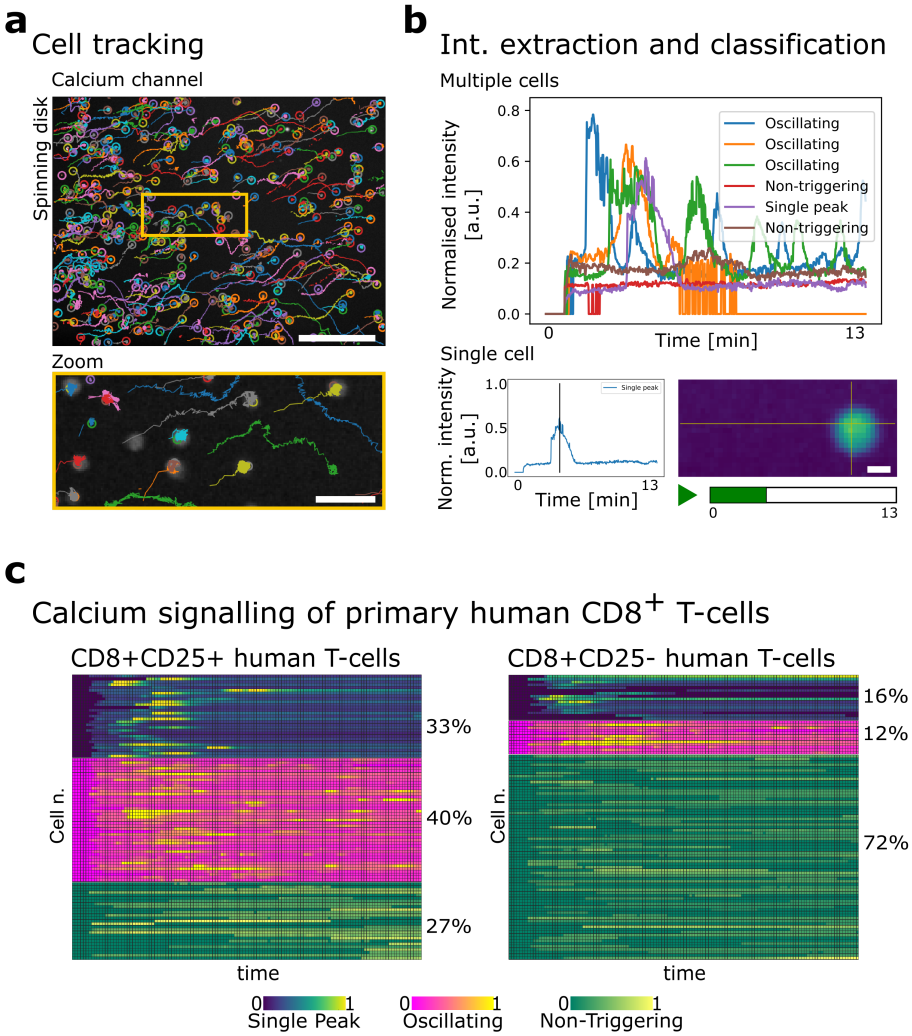



Fig. 5.6 CalQTrace software: cell tracking and $Ca^{2+}$ signalling traces classification. (**a**) Cell tracking. Single frame from the $Ca^{2+}$ channel acquired at t = 13 min showing the tracks in space and time of each of cells during the entire acquisition, zoom-in shown below. Scale bar are 200 µm and 50 µm. (**b**) Intensity extraction and classification. Top - Representative example of $Ca^{2+}$ intensities classified as single-peak, oscillatory and non-triggering using the supervised pre-trained 1D CNN machine learning algorithm. Bottom - Single cell intensity trace plot with its corresponding category outcome from the classification, and its tracked video history over all the acquisition. Scale bar is 8 µm. (**c**) $Ca^{2+}$ signalling of primary human $CD8^+$ T-cells. Heatmaps showing the percentage of the three main $Ca^{2+}$ categories in activated $CD25^+$ (left) and resting $CD25^-$ primary human $CD8^+$ T-cells. The cells were activated on a glass coverslip coated with the OKT3 antibody and biding molecule ICAM-1.

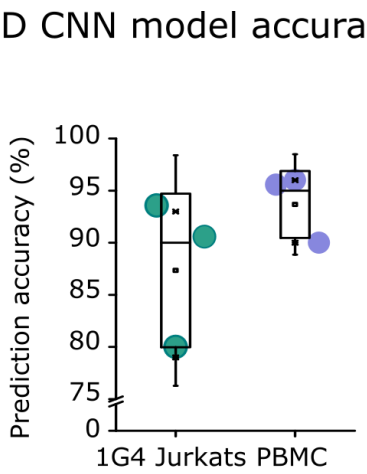



Fig. 5.7 CalQTrace: prediction accuracy. Prediction accuracy of the 1D CNN model implemented in CalQTrace for classifying $Ca^{2+}$ signalling intensity trace during T-cell activation. The prediction accuracy is tested for both the 1G4 Jurkat T-cells line and PBMC primary human T-cells.

9V peptide (highest affinity) > OKT3 > 4D peptide [78] (see Materials and methods for their $k_{off}$ rate). The spreading of the cell contact area over time, as well as its velocity, speed and stability, with respect to each of the $Ca^{2+}$ categories were then analysed adding to the CalQTrace software pipeline using a spreading algorithm plug-in (see Materials and methods).

To detect the contact area spreading of T-cells with high accuracy, while spreading on the functionalised glass coverslip surface, we decided to carry on the experiments at the Zeiss CSD microscope, equipped with the Hamamatsu ORCA-Flash4.0 v2 sCMOS camera and a 10× air objective to have a spatial resolution of 1 µm/pixel. As the average radius of Jurkat T-cells is around 7 µm [198], a single-cell would contain around 150 pixels, allowing to capture the increase of contact area with sufficient sensitivity. The choice of a 10× objective lead to a FOV of 0.8 mm × 0.6 mm, containing few hundreds cells in each experimental condition. For each experiment condition, a dual-colour image was acquired with a temporal resolution of 0.5 fps, for a total duration of 1,000 frames (see Fig. 5.8a and Materials and methods). Excitation of the $Ca^{2+}$ fluorescent channel (Fluo-4, 488 nm

excitation, 561 nm emission) and cell membrane spreading (CellMask Orange 545 nm excitation, 567 nm emission) was implemented using dual-colour sequential acquisition with 488 nm and 561 nm excitation laser lines (see Fig. 5.8a, and Materials and methods). 1G4 Jurkat T-cells were activated through deposition on glass coverslip, which topmost layer was uniformly coated with either a pMHC or antibody (see Fig. 5.8a, and Materials and methods). Three experimental replicates were acquired at different days for each condition.

$Ca^{2+}$ intensity profiles and cell membrane contact area were recorded over time, with single cell resolution (see Fig. 5.8a,b). From a visual inspection, we observed that single-peak responses were often followed by significant increase in contract area, while oscillatory responses leads to less pronounced contact area spreading (see Fig. 5.8b). We therefore built a robust quantitative cell spreading algorithm and we added to the pipeline of CalQTrace analysis. The custom-written cell spreading algorithm aims to extract the ratio, time, stability, and velocity of the cell spreading within each $Ca^{2+}$ category (see Fig. 5.8a and Materials and methods). $Ca^{2+}$classification results, analysed with CalQTrace, show similar outcomes compared to previous work from Lee *et al.* [78], with the highest percentage of single-peak responses for cells that landed on 9V, and more oscillatory and non-triggering responses among cells landed on 4D (see Fig. 5.9a). Within each of the $Ca^{2+}$ categories, the area spreading ratio, defined as the ratio between the maximum area value (m) and its initial value (i), was extracted (see Fig. 5.8a). While the negative control (Bovine Serum Albumins (BSA) coated glass coverslip) did not show spreading, for all the other conditions the 1G4 Jurkat T-cells that had a single-peak $Ca^{2+}$ response presented the largest values of contact area spreading ratio, with a maximum ratio around 1.3 (see Fig. 5.9c, and Materials and methods). In particular, the contact area spreading was significantly higher in cells with single-peak and oscillatory $Ca^{2+}$ responses, compared to cells with a non-triggering $Ca^{2+}$ response. The distribution

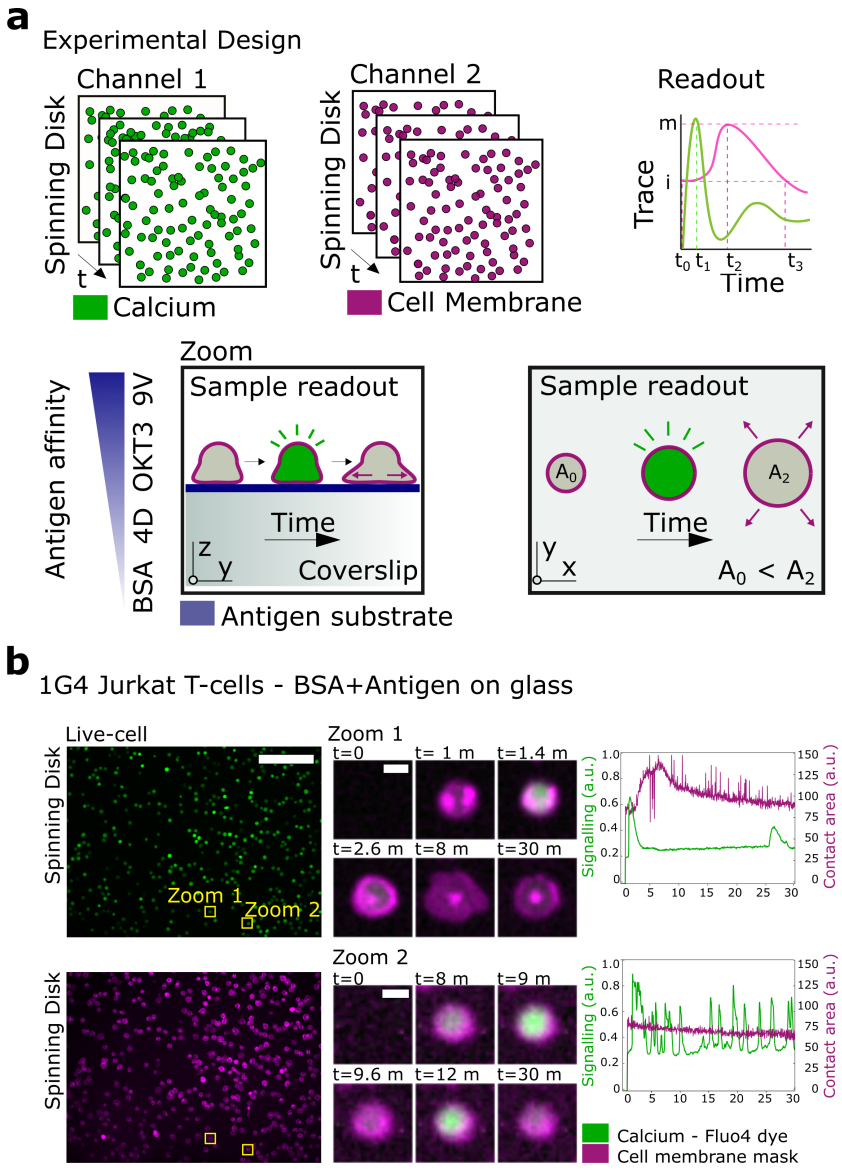



Fig. 5.8 1G4 Jurkat T-cells: $Ca^{2+}$ and spreading assay. (**a**) Schematic of the experiment design. Upper - Two-colour channel acquisition for $Ca^{2+}$ signalling (green) and cell membrane spreading (magenta). Lower - Schematic representation of T-cell activation on functionalised (BSA, OKT3, 4D and 9V) glass coverslips. $Ca^{2+}$ and cell spreading were recorded as a function of time. (**b**) 1G4 Jurkat T-cells activated on glass coverslips coated with BSA and activation molecules. The $Ca^{2+}$ signalling (green) and contact area spreading (magenta) are recorded during time using the spinning disk microscopy. Zoom 1 and 2 show a visual example of single-peak response and large contact area spreading and oscillatory response with less contact area spreading respectively. Their intensity profiles shown on the right. Scale bars are 200 µm and 10 µm.

of area spreading ratios was visualised with probability density function plots. Area spreading ratios across the three $Ca^{2+}$ categories showed a relatively normal distribution (see Fig. 5.9c). Oscillatory T-cells and single-peak T-cells had broader probability density compared to non-triggering cells, which corresponded to a lower number of T-cells exhibiting area spreading ratios of 1 - 1.2 (see Fig. 5.9c). Furthermore, the oscillatory and single-peak probability density functions were shifted further right towards greater contact area spreading ratios. This result was supported visually by the temporal projections of 1G4 Jurkat T-cell cross section along the cell diameter, with both colour channels overlapped (see Fig. 5.9b). The temporal projections were plotted separately using the ImageJ software [143]. T cells showing either an oscillatory or single-peak response exhibited contact area spreading, while T cells showing a non-triggering response did not (see Fig. 5.9b). In particular, contact area spreading during single-peak $Ca^{2+}$ response appeared larger than the one during oscillatory $Ca^{2+}$ response (zoom 1 and zoom 2, see Fig. 5.9b).

Next, we examine differences in contact area spreading from a temporal point of view. We started by comparing the temporal series of the $Ca^{2+}$ and spreading events. The heatmap of both $Ca^{2+}$ intensity and cell spreading shows that cell spreading follows the first $Ca^{2+}$ burst in chronological order (see Fig. 5.9d). We next investigated the cell spreading speed and velocity within a $Ca^{2+}$ category. We defined as 'spreading speed' the time interval between the first $Ca^{2+}$ peak and the maximum contact area value, and as 'velocity' the ratio between the absolute change in contact area and spreading speed. Regarding the spreading speed, while there was no significant difference among all the cells showing oscillatory $Ca^{2+}$ responses for all the three activation conditions (Tukey's HSD, $p < 0.05$), a faster spreading was observed in cells with a single-peak $Ca^{2+}$ response upon 9V activation, as compared to OKT3 and 4D (Tukey's HSD, $p < 0.05$ and $p < 0.001$, respectively) (see Fig. 5.10a). In contrast, the spreading velocity was registered

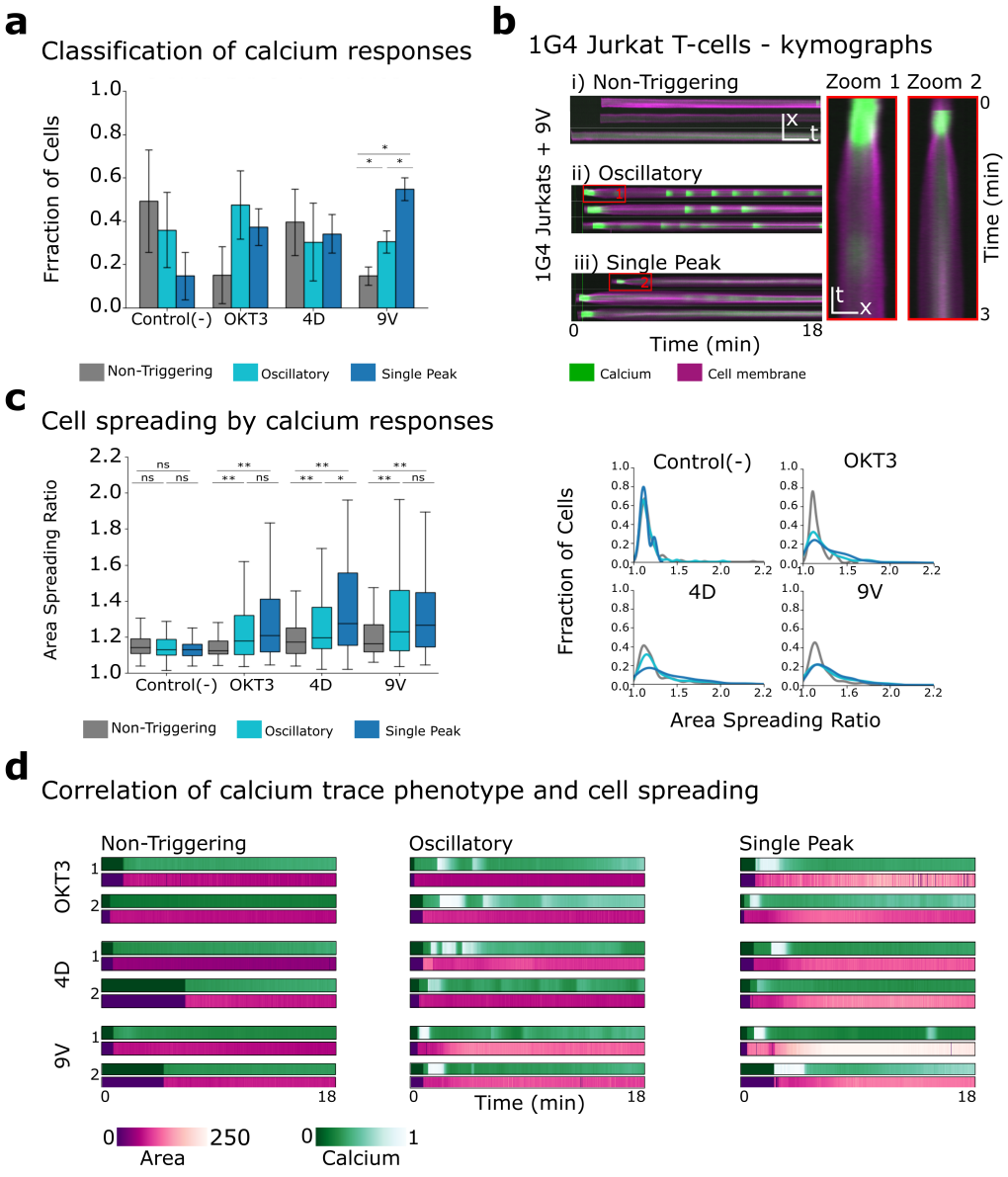



Fig. 5.9 1G4 Jurkat T-cells: $Ca^{2+}$ and spreading analysis. (**a**) Classification of the three main $Ca^{2+}$ responses during 1G4 Jurkat T-cells activation with the OKT3 antibody, and the 4D and 9V peptides. (**b**) Kymograph plots showing representative visual examples of the different $Ca^{2+}$ signalling responses (green) and the correspondent cell contact area spreading (magenta). For each $Ca^{2+}$ category three different cells are shown. (**c**) Left - Relative change in the contact area spreading defined as area spreading ration, with respect to the different $Ca^{2+}$ responses and activation conditions. Right - Probability density function of contact area spreading, with respect to the different $Ca^{2+}$ responses and activation conditions. (**d**) Heatmaps showing $Ca^{2+}$ signalling traces (green) ranging from 0 to 1, and contact area spreading (magenta) ranging from 0 to 250, over the course of 18 min.

to remain constant among all the conditions and categories (see Fig. 5.10b). Lastly, we quantified the stability of the contact area as the amount of time before the contraction of the cells starts, represented as $t_3$ - $t_2$ (see Fig. 5.8a). The stability was higher for cells having single-peak response compared to the oscillatory one (independent samples t-test, $p < 0.001$ and $p < 0.05$, respectively) (see Fig. 5.10c,d). This was true for activation with both the low affinity 4D peptide and the high affinity 9V peptide, however not all conditions shown high p-value significance (see Fig. 5.10c,d).

## 5.5 Development of a large-field-of-view light-sheet hardware

The preceding data showing $Ca^{2+}$ signalling and contact area spreading were measured using CSD microscopy with a 10× magnification objective. While the high resolution of CSD equipped with the 10× objective offers sufficient pixel density to quantify single-cell spreading with high accuracy, it compromises the statistical power due to its limited ability to measure upto a few hundreds cells per FOV.

To increase the statistical power towards FC standards, we next developed a large 4 mm × 3.5 mm FOV light-sheet microscope. The aim is to deliver an optical biophotonic platform with a large FOV at a suitable spatial resolution coupled with the CalQTrace software, to measure immune responses of $10^4$ - $10^5$ T-cells with single-cell resolution. The microscope comprises a broad 4 mm × 3.5 mm light-sheet that is coupled with a 4× objective and large camera sensor that measure simultaneously the activation of $10^4$ - $10^5$ T-cells with single-cell resolution and spatio-temporal information. The core of the hardware is a small upright fluorescence microscope (see Fig. 5.11a). An excitation laser with wavelength 488 nm, coupled to an optical fiber, exits a collimator and is focused into a 50× Olympus illumination objective (NA 0.5) through a cylindrical lens (Thorlabs,

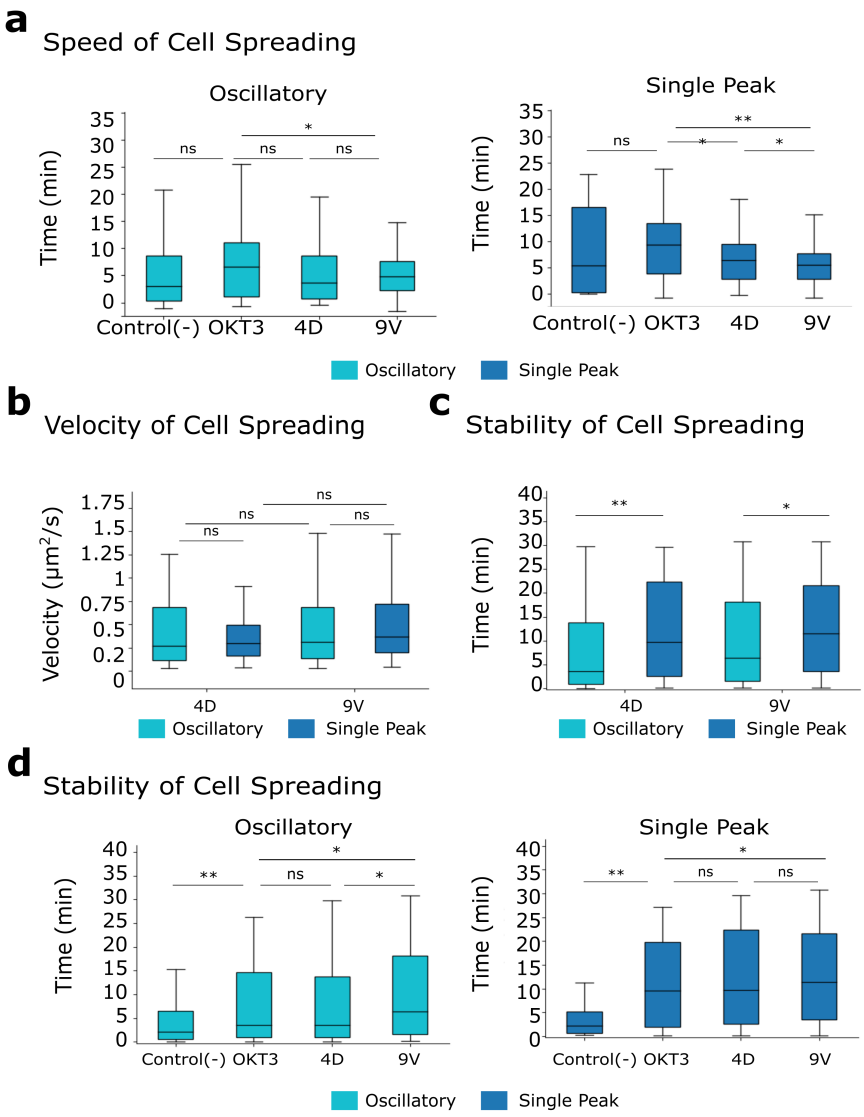



Fig. 5.10 1G4 Jurkat T-cells: spreading speed and stability. (**a**) Spreading speed of 1G4 Jurkat T-cells when activated with the OKT3 antibody and the 4D and 9V peptides. The spreading speed is shown relatively to the single-peak and oscillatory $Ca^{2+}$ responses. (**b**) Spreading velocity of 1G4 Jurkat T-cells when activated with the 4D and 9V peptides. The spreading velocity is shown relatively to the single-peak and oscillatory $Ca^{2+}$ responses. (**c-d**) Spreading stability of 1G4 Jurkat T-cells for the different activation conditions. (ns = $p > 0:05$, * = $p < 0:05$, ** = $p < 0:001$).

focal length: 4 mm). The light exiting the objective is 50 μm thick along the axial axis and extends laterally up to a lateral size of 4 mm at the sample position, effectively taking a shape of a light-sheet within the sample imaging area of 4 mm × 3.5 mm. The light-sheet illuminates the sample from the side. The sample consists of a PDMS chamber on a glass coverslip where the cells are deposited. A glass coverslip is added on top of the PDMS chamber to flatten the cell medium. The sample can be placed on top of a hot plate that maintains a temperature of 37 °C. The light emitted by the sample is next collected by an objective placed on top of it, in an up-right configuration. The collected light is focused on an Andor sCMOS camera (Andor, Zyla 5.5) with a large sensor (16 mm × 14 mm) and a pixel size of 6.5 μm (see Fig. 5.11a). The scope is equipped with 20×, 10×, and 4× magnification objectives. Using the 4× air 0.2 NA collection objective (spatial resolution of around 1.5 μm for a 0.5 μm excitation wavelength) and the Andor Zyla 5.5 camera leads to a FOV of 4 mm × 3.5 mm, and $10^4$ - $10^5$ T-cells can be imaged simultaneously with single-cell resolution at an effective pixel size of 1.6 μm. The scope is coupled with the Andor software for controlling time lapse acquisition. The exposure time can go up to ms, faster than any scanning techniques. A crucial advantage of a light-sheet microscopy is the low power used at the sample level of 1-2 mW. Furthermore, the thin light-sheet reduces the background of all the cells landing on the sample surface.

To obtain high quality imaging with the large FOV light-sheet, the choice of the imaging chamber is crucial. We designed a home-built PDMS chamber and fabricated in collaboration with J. Prentice and the Department of Oncology Workshop (Oxford, UK). The chamber was designed such that the area of the chamber matches the FOV with a favourable depth such that one minimizes the background fluorescence, while on the other hand providing the ability to deliver the cells inside with a standard pipette. To facilitate the chamber production, a mould with 8 chambers was fabricated (see Fig. 5.11b). Among them, 4 chambers had a wall thickness of 3 mm and the others a

thickness of 2 mm. All the 8 chambers had an internal area of 5 mm × 5 mm and a wall height of 1.9 mm. The material used for the chamber was PDMS gel, since its refractive index of 1.33 matched the refractive index of the medium, reducing any potential light scattering. To avoid the formation of bubbles inside the PDMS chamber, we introduced a vacuum step prior to gel polimerisation. Finally, the PDMS was polymerised inside the mould for 48 hrs, removed from the mould and placed on top of a dry glass coverslip. All coverslips functionalisation and washing steps were performed after PDMS chamber deposition. The cells were pipetted from the side of the chamber, through a small cut in the corner of the PDMS chamber, introduced before each experiment (see Fig. 5.11b).

Lastly, the large FOV light-sheet imaging was validated using two biological systems: the adherent HeLa cells and the immune 1G4 Jurkat T-cells. To test the homogeneity of the light-sheet illumination, HeLa cells were allowed to adhere overnight to a glass coverslips functionalised with fibronectin and imaged with three different collection objectives with 4×, 10× and 20× magnification (see Fig. 5.12a). We also run a preliminary experiment using the 1G4 Jurkat T-cells labelled with Fluo-4 (see Fig. 5.12b) during activation with a glass coverslips functionalised with the OKT3 antibody. A total number of around 20,000 T-cells within the FOV was extracted using the CalQTrace software.

## 5.6 Summary

In this chapter, I have described our new developed automated since-cell high-throughput $Ca^{2+}$ platform, consisted of a machine leaning based CalQTrace software and the large 4 mm × 3.5 mm FOV light-sheet microscope. The CalQTrace capabilities of tracking cells, $Ca^{2+}$ signalling classification, and cell exclusion and separation based on surface proteins expression, were validate with a preliminary experiment of 72 hrs pre-activated human $CD8^{+}$ T-cells. From this experiment, three main $Ca^{2+}$ signalling categories of single-peak, oscillatory and non-triggering were registered. Building upon the previous

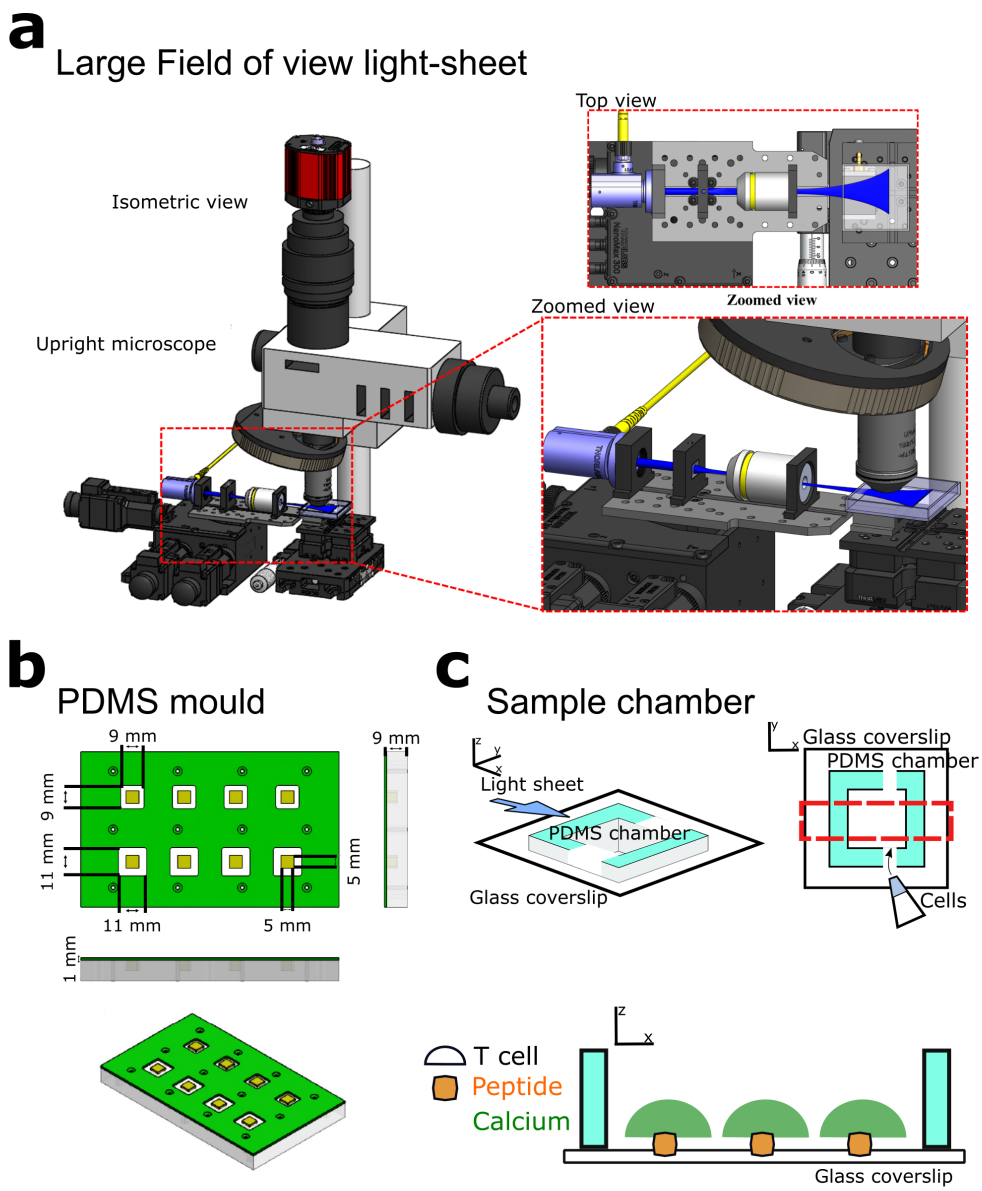



Fig. 5.11 Schematic of the large FOV light-sheet microscope and sample chamber. **a** Upright Olympus microscope equipped with the Andor Zyla 5.5 camera. Zoomed views showing the key optical elements. From left to right: optical fibre (yellow) is connected to a reflected collimator (blue). Next, a cylindrical lens to focus the light into a 50× Olympus illumination objective and exiting as a light-sheet (blue light). The emission light is collected from a 4× objective placed above the sample chamber. (**b**) Left - Schematic of the mould to produce the PDMS chambers. Right - Schematic of the PDMS chamber and sample preparation.

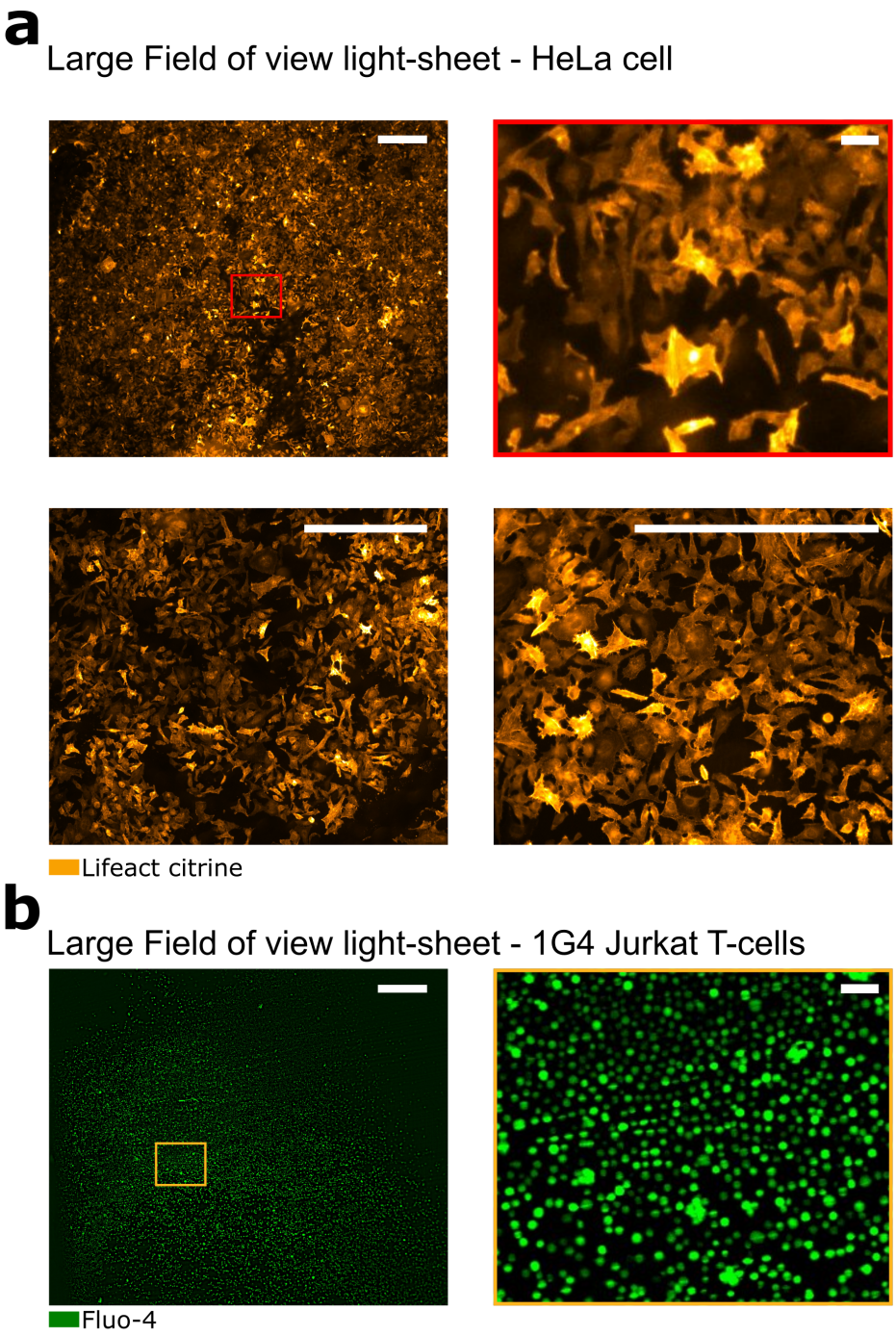



Fig. 5.12 Light-sheet microscope validation with HeLa cells and 1G4 Jurkat T-cells. (**a**) Upper - large FOV light-sheet equipped with a 4× objective imaging HeLa cells expressing Lifeact-citrine (orange) while adhering on the glass coverslips surface coated with FN and a zoomed-in. Scale bars are 500 µm and 50 µm. Lower - same with 10× and 20× objectives. Both scale bars are 500 µm. (**b**) Large FOV light-sheet equipped with a 4× objective imaging 1G4 Jurkat T-cells labelled with Fluo-4 (green). Cells were activated using a glass coverslips coated with the OKT3 antibody. Scale bars are 500 µm and 50 µm.

work of Lee *et. al* [78], we found a correlation between the types of $Ca^{2+}$ signalling and IS spreading during activation of 1G4 Jurkat T-cells upon activation with different antigen affinities to the 1G4 TCR. In agreement with the previous work, the fraction of single-peak responses correlated with antigen affinity (see Fig. 5.9a). 1G4 Jurkat T-cells activated with the 9V peptide shown higher fraction of single-peak responses compared to the one activated with the 4D peptide. Specifically for the 9V condition, statistical significance in the single-peak response was observed compared to the other responses, while comparable fraction was observed for the 9V condition in all the three classes (see Fig. 5.9a). Similar to Lee *et al.* [78], equivalent fraction of single-peak responses was observed when using the OKT3 antibody, although its affinity its known to be higher than the 4D one. Using CalQTrace with a home-built plug-in for cell spreading assay, we observed statistical significance in the contact area spreading when cells were showing single-peak or oscillatory $Ca^{2+}$ signalling. This was not the case for cells showing a non-triggering response, whose contact area spreading was almost null (see Fig. 5.9c). No statistical significance was found in the contact area spreading when comparing single-peak and oscillatory responses, however single-peak responses showed higher spreading stability compared to oscillatory, in both the 4D and 9V conditions (see Fig. 5.10c,d). In addition, visual inspection of $Ca^{2+}$ and contact area spreading via heatmaps showed that $Ca^{2+}$ burst in the single-peak response happens before the cell starts spreading (see Fig. 5.9b,d). Overall, these experiments suggest that $Ca^{2+}$ responses might be indicative of the T-cell activation strength, given that the spreading and stability of the IS is crucial for a full T-cell activation and function [200, 216]. Analysis about the dynamics of the spreading revealed that the speed of cell spreading was higher in the OKT3 condition for both oscillatory and single-peak responses (see Fig. 5.10a). We examined also the spreading velocity but no significant differences in velocity were found among all the conditions (see Fig. 5.10b). This was surprising because previous work from the lab

correlated peptide $k_{off}$ rate with actin velocity [25]. One explanation could be that in this presented work we labelled the 1G4 Jurkat cell membrane, rather than the actin cytoskeleton. Another reason could be that our method to extract the velocity based on the cell spreading might not be sensitive enough for velocity extrapolation.

Given the heterogeneity of $Ca^{2+}$ responses during T-cell activation, we next extended the statistical power building a large 4 mm × 3.5 mm FOV light-sheet microscope (see Fig. 5.11a). To allow high quality imaging with illumination light coming from the side, we designed and built a mould for fabricating PDMS chambers, whose refractive index of 1.33 matches the cell medium one (see Fig. 5.11b). To capture all cells in the sample, the chamber dimensions were built accordingly to the camera FOV. Validation of the light-sheet microscope, using the HeLa cells and 1G4 Jurkat T-cells biological systems, confirmed a uniform illumination, using 20×, 10× and 4× magnification objectives. Using CalQTrace on the 1G4 Jurkat T-cells data, more than 20,000 T-cells were counted in the FOV. However, we noticed that illumination artefacts with a stripe-like shape were detected in the FOV, affecting the single-cell illumination during $Ca^{2+}$ release (see zoom in Fig. 5.12). This is a quite common issue encountered in light-sheet microscopy [217, 218]. Future work would be to overcome to this limitation, with as a possibility being in introducing a line diffuser [219]. Coupling the light-sheet with a 2× collection objective would increase even further the FOV size and allow imaging of $>$ 100,000 immune cell simultaneously. To repeat the $Ca^{2+}$ - spreading assay with higher statistical power, multi-color excitation beams and a software to control the acquisition would be an asset. Finally, to build upon our hypothesis that $Ca^{2+}$ signalling might predict the strength of T-cell activation, experiments where actin polymerisation is blocked and $Ca^{2+}$ signalling and expression of surface proteins (e.g. CD25) measured will be crucial.

# Chapter 6

# Discussion

The findings and results in this thesis were discussed in detail individually in chapters 4 and 5. In this chapter, I will present an overall summary of the thesis and suggest directions for future work.

## 6.1 Summary of the thesis

In this thesis, I presented different methodologies that I developed to quantify nanometre length and sub-second time scales force production, $Ca^{2+}$ signalling and activation marker expression for investigating immune cell mechanobiology.

In the first part of the thesis, I presented three new methods for measuring mechanical forces with high spatio-temporal sensitivity during cell interaction with the external biophysical environment. Combining TFM with TIRF-SIM and employing the high-refractive index (nr = 1.49) silicone gel, the new developed 2D TIRF-SIM-TFM technique showed a $>$ 2-fold improvement in the spatial resolution and a $>$ 10-fold improvement in the temporal resolution compared to previous TFM modalities [180]. The increased spatial resolution allowed the use of smaller PIV window sizes, with a consequent increased in the sensitivity, precision and accuracy of force recovery. At the same time, the increased

temporal resolution allowed to acquire live-cell force generation with a maximum of 2.5 fps. Using computer simulations, I first demonstrated the experimental power of the new technique with respect to the standard WF-TFM. Quantitative analysis of the simulations resulted in a guide for designing TFM experiments and data processing, by finding the optimal fiducial marker bead density and PIV window size as a function of cell displacement, for both 2D TIRF-SIM-TFM and WF-TFM techniques. In the case of high bead density and small PIV window sizes, 2D TIRF-SIM-TFM showed maximal benefits compared to WF-TFM for recovering small displacements. The technique, validated using three different biological samples, namely HeLa cells, RBL cells and primary salmon keratocytes, revealed nanometre length and sub-second time scales mechanical force that could not be measured with previous TFM techniques.

To extend our probing to mechanical force generated along the axial direction, we next combined TFM with 3D SIM [125]. The 3D SIM-TFM technique offers the same 100 nm lateral spatial resolution obtained with 2D TIRF-SIM-TFM with now an additional axial resolution of 250 nm to capture the movement of beads along the direction perpendicular to the gel surface. Regarding the temporal resolution, 3D SIM-TFM offers 3D force sampling with a speed 1.5 times slower than 2D TIRF-SIM-TFM, because it requires scanning in the axial direction, but much faster compared to any standard raster scanning based microscopy techniques, such as confocal or STED, because of its WF 2D illumination. The capabilities of 3D SIM-TFM have been demonstrated by imaging the rapid force generation during early adhesion of HeLa cells on the silicone gel.

As a final step, we lift of the limitations in 3D SIM-TFM by combining TFM with astigmatic imaging, improving significantly the temporal resolution for simultaneous lateral and vertical force measurements [134]. The aTFM technique offered 2.5D force acquisition with temporal resolution comparable to 2D TIRF-SIM-TFM, due to its ability to extract both lateral and vertical gel displacement informations within one single

2D image. In order to realize this technique, we first showed a way to calibrate and obtain the axial position information by measuring the aberrated PSF in the presence of a cylindrical lens using fluorescence marker beads. The calibration gave a fitting localisation uncertainty of around 9 nm laterally and 22 nm axially. Next, the aTFM technique was validated by acquiring lateral and vertical force generation during early adhesion stages of HeLa cells and during the immune activation of RBL cells.

Overall, motivated by the lack of sensitivity for mechanical force measurements, we combined TFM with TIRF, SIM and astigmatism, improving the spatial and temporal performance in either 2D or 3D of mechanical force quantification, with low illumination power and minimised phototoxicity. We achieved a nanometre length and sub-second time scales sensitivity for lateral and axial force measurement. These three techniques, easily implemented on a single optical set-up, offer a powerful platform which in the future will allow to quantify force generation during immune cell function at unprecedented sensitivity and bio-compatibility [220].

In the second part of the thesis, I presented a new methodology that we developed to measure and classify $Ca^{2+}$ signalling of $>$ 20,000 T cells during their immune activation. To this end, I first presented CalQTrace, a software based on a 1D CNN algorithm, that can detect and track live-cells in space and time, separate them in sub-populations with respect to their activation marker expressions, and classify their $Ca^{2+}$ signalling into the three main responses observed that are single-peak, oscillatory and non-triggering. The detailed description of the software pipeline and the GUI used for making it user-friendly can be found in section 5.4. Trained with two cell types, the 1G4 Jurkat T-cells and the primary human PBMC T-cells, CalQTrace offered an automated classification prediction accuracy of $>$ 90%. During software validation with 72 hrs pre-activated $CD25^{+}$ and resting $CD25^{-}$ primary human $CD8^{+}$ T-cells, we observed that the $CD25^{+}$ T-cells primarily exhibited single-peak and oscillatory responses, while the majority of

resting $CD25^-$ exhibited a non-triggering response. To further analyse the three $Ca^{2+}$ signalling responses, we extended the work of Lee *et al.* [78], imaging $Ca^{2+}$ signalling and IS spreading simultaneously during activation of 1G4 Jurkat T-cells exposed to different peptide affinities. This analysis suggested that while single-peaks are often associated with a large and stable IS spreading, this is not the case for oscillatory and non-triggering responses. Additionally, we observed that single-peak responses with large IS spreading were encountered in 1G4 Jurkat T-cells when being activated with the high affinity 9V peptide. Finally, to increase the statistical power of the $Ca^{2+}$ imaging, we developed a new large 4 mm $\times$ 3.5 mm FOV light-sheet microscope that, combined with a 4$\times$ collection objective and a large sensor Andor sCMOS camera can image simultaneously $>$ 20,000 T cells within the FOV. In addition, we designed and fabricated a PDMS chamber that fits the FOV and allows lateral sample illumination by the light-sheet. The light-sheet microscope was validated imaging HeLa cells on a glass coverslips coated with FN and 1G4 Jurkat T-cells during activation with a glass coverslips functionalised with the OKT3 antibody.

Overall, we developed a user-independent and user-friendly software that provides multi-parameter readouts, and a large FOV light-sheet microscope that offers statistics comparable to FC. Their combination represents a powerful platform to link early signalling events to long-term functional response of T cells.

## 6.2 Future work

The work of this thesis presents numerous future directions. The aim of the thesis was to establish new sensitive quantitative biophysical methods to investigate the significance of mechanobiology in immune cell activation. Our objective was to build methods for mechanical force measurements, $Ca^{2+}$ signalling and surface protein expression readouts with high spatio-temporal sensitivity, robust quantification, and high statistical power.

To validate the newly developed TFM methodologies, we used HeLa cells, RBL and salmon keratocytes, as well-characterised models to investigate small and rapid force measurements. Future work will focus on applying these new live-cell super-resolution TFM methodologies to investigate the role of mechanobiolgy during activation of primary (e.g. human or mouse) T-cells. Recent work from Colin-York *et al.* [25] has shown that T cells adapt their actin dynamics to the antigen affinity, yet it is not known if they can adapt their actin dynamics and force production when interacting with elastic substrates of different stiffness to sustain their activation. Previous work has shown that the external substrate rigidity has a significant impact on T-cell proliferation after activation [75]. It has also been shown, through quantification of IL-2 segregation and cell spreading, that primary T-cells display a biphasic activation behaviour during interaction with substrate of different rigidities [221, 222]. Building upon these works, we can use the 2D TIRF-SIM-TFM technique to explore the lateral mechanical force generated by the cell on substrates with different rigidities with high spatial resolution. In addition, of particular interest will be to examine their lateral and vertical force production correlating 2D TIRF-SIM-TFM with aTFM during T-cell activation on different elastic gel rigidities that are functionalised with antigens of different affinity to the receptor. While the first would give some insights into the force applied during TCR cluster motion at the IS, the second would reveal the force necessary for a stable TCR-pMHC binding with peptides displaying low and high affinities on top of soft and stiff surfaces, giving new insights into cell functioning, differentiation, proliferation and metabolism [223, 58, 75, 224].

In addition to the force readout, future work will focus on investigating their $Ca^{2+}$ responses using the single-cell high-throughput platform that we developed. Overall, these experiments will build upon the current research about mechanobiology and mechanoadaptation of T cells to the physical environment [225, 58, 226, 227, 41].

To move from immortalised Jurkat T-cells to primary cells [198], it will be necessary to find a model equivalent to the 1G4 Jurkat cell line. This will give us control over the specific TCR-antigen activation. One possibility would be using the OT-1 mouse $CD8^+$ T-cell model system activated with the high-affinity SIINFEKL (N4) and low-affinity SIITFEKL (T4) OVA analogue peptides, although as for any transgenic organism they might be highly immuno-compromised [228–231].

Regarding the automated single-cell high-throughput $Ca^{2+}$ platform, future work will aim for extending the statistical power implementing a 2× 0.1 NA collection objective and a larger PDMS chamber to image simultaneously as many as 100,000 immune cells. To go towards more physiological conditions, it would be critical also to perform cell-to-cell assays looking at T-cell activation when interacting with a real APC, instead of mimicking this interaction with glass or gel substrate [232–235]. To achieve this, the CalQTrace software and the microscope require an extension such that multiple-cell types can be imaged, detected and tracked in a spatio-temporal manner. Implementing an algorithm to detect cell-to-cell contact events and describing cell-population clustering together with their spatial arrangement will be a powerful tool [236, 237]. Furthermore, the light-sheet scope together with the CalQTrace can be extended for imaging immune cell activation during their dynamical interactions within a tissue slice and organoids [238]. In this case, three dimensional imaging and data analysis involving spatial statistics will yield a wealth of information. In particular, the spatial arrangement of the various cell types around a pathogenic cell or an APC will enhance the understanding of immune system in health and disease [239–241].

Finally, all the techniques and methodologies developed in this thesis share a common future direction as a combination for 'coincidence' analysis to measure multiple readouts simultaneously [242, 91, 1, 243]. Indeed until now, two separate samples were required, one for mechanical force measurements, and the other for $Ca^{2+}$ signalling and expression

of surface marker readouts. Our aim in the future is to build a high-throughput platform that integrates the TFM methodology on the large FOV light-sheet microscope, to investigate mechanobiology of > 100,000 immune cells measuring at the same time force generation, $Ca^{2+}$ signalling and surface marker expression with the required spatio-temporal information.

## 6.3 DPhil Publications

* - equally contributing authors

7. **Barbieri, Liliana***; Colin-York, Huw*; Korochevskaya, Kseniya*; Li, Di; Karedla, Karedla; Schneider, Falk; Dustin, Michael; Li, Dong; Fritzsche, Marco; Two-dimensional TIRF - Structual Illumination Microscopy - Traction Force Microscopy (2D-TIRF-SIM-TFM), Nature Communications, 2021

6. Li, Di*; Colin-York, Huw*; **Barbieri, Liliana***; Guo, Yuting; Korochevskaya, Kseniya; Li, Dong; Fritzsche, Marco; Three-dimensional Astigmatic TIRF Traction Force Microscopy (3Da-TFM), Nature Communications, 2021

5. Korochevskaya, Kseniya; Colin-York, Huw; **Barbieri, Liliana**; Fritzsche, Marco; Extended mechanical force measurements using structured illumination microscopy, Philosophical Transactions A, 2021

4. Colin-York, Huw; Kumari, Sudha; **Barbieri, Liliana**; Cords, Lena; Fritzsche, Marco; Distinct actin cytoskeleton behaviour in primary and immortalised T-cells, Journal of cell science, 2020

3. Skamrahl, Mark; Colin-York, Huw; **Barbieri, Liliana**; Fritzsche, Marco; Simultaneous Quantification of the Interplay Between Molecular Turnover and Cell Mechanics by AFM–FRAP, Small, 2019

2. Colin-York, Huw; Javanmardi, Yousef; **Barbieri, Liliana**; Li, Di; Korobchevskaya, Kseniya; Guo, Yuting; Hall, Chloe; Taylor, Aaron; Khuon, Satya; Sheridan, Graham K; Spatiotemporally super-resolved volumetric traction force microscopy, Nano letters, 2019

1. Colin-York, H; **Barbieri, Liliana**; and Fritzsche, Marco; Mechanical forces guide the biophysics of immune cells, Microscopy, 2018

# References


[1] Fritzsche, M. *What Is the Right Mechanical Readout for Understanding the Mechanobiology of the Immune Response?* Frontiers in Cell and Developmental Biology, 9:612539, 2021.

[2] Schwarz, U. S. *Mechanobiology by the numbers: A close relationship between biology and physics*, 2017.

[3] Peter Parham. *The Immune System*. Garland Science: New York, 4th edition, 2014.

[4] Charles A Janeway, J., et al. *The components of the immune system*. Garland Science, 2001.

[5] Pennock, N. D., et al. *T cell responses: Naïve to memory and everything in between*. American Journal of Physiology - Advances in Physiology Education, 37(4):273–283, 2013.

[6] Punt, J. *Adaptive Immunity: T Cells and Cytokines*. In *Cancer Immunotherapy: Immune Suppression and Tumor Growth: Second Edition*, pages 41–53. Elsevier Inc., 2013.

[7] Fracchia, K. M., et al. *Modulation of T Cell Metabolism and Function through Calcium Signaling*. Frontiers in Immunology, 4, 2013.

[8] Murphy, K. M. *Janeway's Immunobiology*. Garoland Science, 8th edition, 2021.

[9] Weiss, A. and Littman, D. R. *Signal transduction by lymphocyte antigen receptors*, 1994.

[10] van der Merwe, P. A. and Dushek, O. *Mechanisms for T cell receptor triggering*. Nature Reviews Immunology, 11(1):47–55, 2011.

[11] Smith-Garvin, J. E., et al. *T Cell Activation*. Annual Review of Immunology, 27(1):591–619, 2009.

[12] Burkhardt, J. K., et al. *The Actin Cytoskeleton in T Cell Activation*. Annual Review of Immunology, 26(1):233–259, 2008.

[13] Poulin, B., et al. *Intramolecular interaction between phosphorylated tyrosine-783 and the C-terminal Src homology 2 domain activates phospholipase C-$\gamma$1*. Proceedings of the National Academy of Sciences of the United States of America, 102(12):4276–4281, 2005.

[14] Treves, S., et al. *Calcium and inositolphosphates in the activation of T cell-mediated cytotoxicity.* Journal of Experimental Medicine, 166(1):33–42, 1987.

[15] Luik, R. M., et al. *The elementary unit of store-operated Ca2+ entry: Local activation of CRAC channels by STIM1 at ER-plasma membrane junctions.* Journal of Cell Biology, 174(6):815–825, 2006.

[16] Kumari, S., et al. *T cell antigen receptor activation and actin cytoskeleton remodeling.* Biochimica et Biophysica Acta - Biomembranes, 1838(2):546–556, 2014.

[17] Fritzsche, M., et al. *Self-organizing actin patterns shape membrane architecture but not cell mechanics.* Nature Communications, 8:17–19, 2017.

[18] Fritzsche, M., et al. *Analysis of turnover dynamics of the submembranous actin cortex.* Molecular Biology of the Cell, 24(6):757–767, 2013.

[19] Fritzsche, M., et al. *Actin kinetics shapes cortical network structure and mechanics.* Science Advances, 2(4):1–13, 2016.

[20] Ochs, H. D. and Thrasher, A. J. *The Wiskott-Aldrich syndrome*, 2006.

[21] Varma, R., et al. *T Cell Receptor-Proximal Signals Are Sustained in Peripheral Microclusters and Terminated in the Central Supramolecular Activation Cluster.* Immunity, 25(1):117–127, 2006.

[22] DeMond, A. L., et al. *T cell receptor microcluster transport through molecular mazes reveals mechanism of translocation.* Biophysical Journal, 94(8):3286–3292, 2008.

[23] Yokosuka, T., et al. *Newly generated T cell receptor microclusters initiate and sustain T cell activation by recruitment of Zap70 and SLP-76.* Nature Immunology, 6(12):1253–1262, 2005.

[24] Wülfing, C. and Davis, M. M. *A receptor/cytoskeletal movement triggered by costimulation during T cell activation.* Science, 282(5397):2266–2269, 1998.

[25] Colin-York, H., et al. *Cytoskeletal Control of Antigen-Dependent T Cell Activation.* Cell Reports, 26(12):3369–3379.e5, 2019.

[26] Monks, C. R., et al. *Three-dimensional segregation of supramolecular activation clusters in T cells.* Nature, 395(6697):82–86, 1998.

[27] Choudhuri, K., et al. *Polarized release of T-cell-receptor-enriched microvesicles at the immunological synapse.* Nature, 507(7490):118–123, 2014.

[28] Freiberg, B. A., et al. *Staging and resetting T cell activation in SMACs.* Nature Immunology, 3(10):911–917, 2002.

[29] Fritzsche, M., et al. *Cytoskeletal actin dynamics shape a ramifying actin network underpinning immunological synapse formation.* Science Advances, 3(6), 2017.

[30] Zumdieck, A., et al. *Stress Generation and Filament Turnover during Actin Ring Constriction.* PLoS ONE, 2(8):e696, 2007.

[31] Elzinga, M., et al. *Complete amino acid sequence of actin of rabbit skeletal muscle.* Proceedings of the National Academy of Sciences of the United States of America, 70(9):2687–2691, 1973.

[32] Holmes, K. C., et al. *Atomic model of the actin filament.* Nature, 347(6288):44–49, 1990.

[33] Pollard, T. D. *Rate constants for the reactions of ATP- and ADP-actin with the ends of actin filaments.* Journal of Cell Biology, 103(6):2747–2754, 1986.

[34] Blancholn, L., et al. *Direct observation of dendritic actin filament networks nucleated by Arp2/3 complex and WASP/Scar proteins.* Nature, 404(6781):1007–1011, 2000.

[35] Bovellan, M., et al. *Cellular control of cortical actin nucleation.* Current Biology, 24(14):1628–1635, 2014.

[36] Cai, E., et al. *Visualizing dynamic microvillar search and stabilization during ligand detection by T cells.* Science, 356(6338), 2017.

[37] Yi, J. C. and Samelson, L. E. *Microvilli set the stage for T-cell activation*, 2016.

[38] Babich, A., et al. *F-actin polymerization and retrograde flow drive sustained PLC$\gamma$1 signaling during T cell activation.* Journal of Cell Biology, 197(6):775–787, 2012.

[39] Trebak, M. and Kinet, J. P. *Calcium signalling in T cells*, 2019.

[40] Feske, S., et al. *Immunodeficiency due to mutations in ORAI1 and STIM1*, 2010.

[41] Joseph, N., et al. *The calcium feedback loop and T cell activation: How cytoskeleton networks control intracellular calcium flux*, 2014.

[42] Quintana, A., et al. *T cell activation requires mitochondrial translocation to the immunological synapse.* Proceedings of the National Academy of Sciences of the United States of America, 104(36):14418–14423, 2007.

[43] Quintana, A. and Hoth, M. *Mitochondrial dynamics and their impact on T cell function.* Cell Calcium, 52(1):57–63, 2012.

[44] Valitutti, S., et al. *Sustained signaling leading to t cell activation results from prolonged t cell receptor occupancy. role of t cell actin cytoskeleton.* Journal of Experimental Medicine, 181(2):577–584, 1995.

[45] Hartzell, C. A., et al. *Calcium influx through CRAC channels controls actin organization and dynamics at the immune synapse.* eLife, 5(2016JULY):1–28, 2016.

[46] Lewis, R. S. *Calcium Signaling Mechanisms in T Lymphocytes.* Annual Review of Immunology, 19(1):497–521, 2001.

[47] Wülfing, C., et al. *Kinetics and extent of T cell activation as measured with the calcium signal.* Journal of Experimental Medicine, 185(10):1815–1825, 1997.

[48] Irvine, D. J., et al. *Direct observation of ligand recognition by T cells.* Nature, 419(6909):845–849, 2002.

[49] Kalia, V. and Sarkar, S. *Regulation of Effector and Memory CD8 T Cell Differentiation by IL-2-A Balancing Act*, 2018.

[50] Faustman, D. L. and Davis, M. *TNF receptor 2 and disease: Autoimmunity and regenerative medicine*. Frontiers in Immunology, 4(DEC):478, 2013.

[51] Aggarwal, B. B., et al. *Historical perspectives on tumor necrosis factor and its superfamily: 25 years later, a golden journey*, 2012.

[52] Castro, F., et al. *Interferon-gamma at the crossroads of tumor immune surveillance or evasion*, 2018.

[53] Charles A Janeway, J., et al. *T cell-mediated cytotoxicity*. Garland Science, 2001.

[54] Shipkova, M. and Wieland, E. *Surface markers of lymphocyte activation and markers of cell proliferation*, 2012.

[55] Reddy, M., et al. *Comparative analysis of lymphocyte activation marker expression and cytokine secretion profile in stimulated human peripheral blood mononuclear cell cultures: An in vitro model to monitor cellular immune function*. Journal of Immunological Methods, 293(1-2):127–142, 2004.

[56] Pauken, K. E. and Wherry, E. J. *Overcoming T cell exhaustion in infection and cancer*, 2015.

[57] Webb, J. R., et al. *PD-L1 expression is associated with tumor-infiltrating T cells and favorable prognosis in high-grade serous ovarian cancer*. Gynecologic Oncology, 141(2):293–302, 2016.

[58] Harrison, D. L., et al. *T-cell mechanobiology: Force sensation, potentiation, and translation*, 2019.

[59] Fritz-Laylin, L. K., et al. *Actin-Based protrusions of migrating neutrophils are intrinsically lamellar and facilitate direction changes*. eLife, 6, 2017.

[60] Liu, B., et al. *Accumulation of dynamic catch bonds between TCR and agonist peptide-MHC triggers T cell signaling*. Cell, 157(2):357–368, 2014.

[61] Chen, W., et al. *Monitoring receptor-ligand interactions between surfaces by thermal fluctuations*. Biophysical Journal, 94(2):694–701, 2008.

[62] Babich, A. and Burkhardt, J. K. *Coordinate control of cytoskeletal remodeling and calcium mobilization during T-cell activation*. Immunological Reviews, 256(1):80–94, 2013.

[63] Comrie, W. A. and Burkhardt, J. K. *Action and traction: Cytoskeletal control of receptor triggering at the immunological synapse*. Frontiers in Immunology, 7(MAR):1–25, 2016.

[64] Bubb, M. R., et al. *Jasplakinolide, a cytotoxic natural product, induces actin polymerization and competitively inhibits the binding of phalloidin to F-actin*. Journal of Biological Chemistry, 269(21):14869–14871, 1994.

[65] Casella, J. F., et al. *Cytochalasin D inhibits actin polymerization and induces depolymerization of actin filaments formed during platelet shape change.* Nature, 293(5830):302–305, 1981.

[66] Comrie, W. A., et al. *F-actin flow drives affinity maturation and spatial organization of LFA-1 at the immunological synapse.* Journal of Cell Biology, 208(4):475–491, 2015.

[67] Hu, K. H. and Butte, M. J. *T cell activation requires force generation.* Journal of Cell Biology, 213(5):535–542, 2016.

[68] Dustin, M. L. and Kam, L. C. *Tapping out a mechanical code for T cell triggering.* Journal of Cell Biology, 213(5):501–503, 2016.

[69] Huse, M. *Mechanical forces in the immune system.* Nature Reviews Immunology, 17(11):679–690, 2017.

[70] Rothenberg, E. V. *The chromatin landscape and transcription factors in T cell programming*, 2014.

[71] Miroshnikova, Y. A., et al. *Emerging roles of mechanical forces in chromatin regulation.* Journal of cell science, 2017.

[72] Aramesh, M., et al. *Engineering T-cell activation for immunotherapy by mechanical forces*, 2019.

[73] Judokusumo, E., et al. *Mechanosensing in T lymphocyte activation.* Biophysical Journal, 102(2):L5–L7, 2012.

[74] Schwarz, U. S. and Gardel, M. L. *United we stand – integrating the actin cytoskeleton and cell–matrix adhesions in cellular mechanotransduction.* Journal of Cell Science, 125(13):3051–3060, 2012.

[75] Connor, R. S. O., et al. *Substrate rigidity regulates human T cell activation and proliferation.* The Journal of . . . , 189(3):1330–1339, 2012.

[76] Bufi, N., et al. *Human primary immune cells exhibit distinct mechanical properties that are modified by inflammation.* Biophysical Journal, 108(9):2181–2190, 2015.

[77] Arrol, H. P., et al. *Intracellular calcium signalling patterns reflect the differentiation status of human T cells.* Clinical and Experimental Immunology, 153(1):86–95, 2008.

[78] Lee, A. M., et al. *CalQuo2: Automated Fourier-space, population-level quantification of global intracellular calcium responses.* Scientific Reports, 7(1):1–11, 2017.

[79] Christo, S. N., et al. *Scrutinizing calcium flux oscillations in T lymphocytes to deduce the strength of stimulus.* Scientific Reports, 5, 2015.

[80] Smoligovets, A. A., et al. *Characterization of dynamic actin associations with T-cell receptor microclusters in primary T cells.* Journal of Cell Science, 125(3):735–742, 2012.

[81] Bendfeldt, H., et al. *IL-2 Expression in Activated Human Memory FOXP3+ Cells Critically Depends on the Cellular Levels of FOXP3 as Well as of Four Transcription Factors of T Cell Activation*. Frontiers in Immunology, 3(AUG):264, 2012.

[82] Ahn, E., et al. *Role of PD-1 during effector CD8 T cell differentiation*. Proceedings of the National Academy of Sciences of the United States of America, 115(18):4749–4754, 2018.

[83] De La Zerda, A., et al. *Review: Bioengineering strategies to probe T cell mechanobiology*, 2018.

[84] Schneider, F., et al. *Quantitative Bio-Imaging Tools to Dissect the Interplay of Membrane and Cytoskeletal Actin Dynamics in Immune Cells*, 2021.

[85] Blakely, B. L., et al. *A DNA-based molecular probe for optically reporting cellular traction forces*. Nature Methods, 11(12):1229–1232, 2014.

[86] Grashoff, C., et al. *Measuring mechanical tension across vinculin reveals regulation of focal adhesion dynamics*. Nature, 466(7303):263–266, 2010.

[87] Liu, Y., et al. *Tension sensing nanoparticles for mechano-imaging at the living/nonliving interface*. Journal of the American Chemical Society, 135(14):5320–5323, 2013.

[88] Stabley, D. R., et al. *Visualizing mechanical tension across membrane receptors with a fluorescent sensor*. Nature Methods, 9(1):64–67, 2012.

[89] Morimatsu, M., et al. *Visualizing the Interior Architecture of Focal Adhesions with High-Resolution Traction Maps*. Nano Letters, 15(4):2220–2228, 2015.

[90] Gayrard, C. and Borghi, N. *FRET-based Molecular Tension Microscopy*, 2016.

[91] Skamrahl, M., et al. *Simultaneous Quantification of the Interplay Between Molecular Turnover and Cell Mechanics by AFM–FRAP*. Small, 15(40):1902202, 2019.

[92] Hosseini, B. H., et al. *Immune synapse formation determines interaction forces between T cells and antigen-presenting cells measured by atomic force microscopy*. Proceedings of the National Academy of Sciences of the United States of America, 106(42):17852–17857, 2009.

[93] Moeendarbary, E. and Harris, A. R. *Cell mechanics: principles, practices, and prospects*. Wiley Interdisciplinary Reviews: Systems Biology and Medicine, 6(5):371–388, 2014.

[94] Whited, A. M. and Park, P. S. *Atomic force microscopy: A multifaceted tool to study membrane proteins and their interactions with ligands*, 2014.

[95] Capitanio, M. and Pavone, F. S. *Interrogating biology with force: Single molecule high-resolution measurements with optical tweezers*, 2013.

[96] Neuman, K. C. and Nagy, A. *Single-molecule force spectroscopy: Optical tweezers, magnetic tweezers and atomic force microscopy*, 2008.

[97] Arbore, C., et al. *Probing force in living cells with optical tweezers: from single-molecule mechanics to cell mechanotransduction*, 2019.

[98] Kim, S. T., et al. *The $\alpha\beta$ T cell receptor is an anisotropic mechanosensor.* Journal of Biological Chemistry, 284(45):31028–31037, 2009.

[99] Polacheck, W. J. and Chen, C. S. *Measuring cell-generated forces: a guide to the available tools.* Nature Methods, 13(5):415–423, 2016.

[100] Tan, J. L., et al. *Cells lying on a bed of microneedles: An approach to isolate mechanical force.* Proceedings of the National Academy of Sciences, 100(4):1484–1489, 2003.

[101] Jin, W., et al. *T cell activation and immune synapse organization respond to the microscale mechanics of structured surfaces.* Proceedings of the National Academy of Sciences of the United States of America, 116(40):19835–19840, 2019.

[102] Colin-York, H., et al. *Super-Resolved Traction Force Microscopy (STFM).* Nano Letters, 16(4):2633–2638, 2016.

[103] Stubb, A., et al. *Fluctuation-Based Super-Resolution Traction Force Microscopy.* Nano Letters, 20(4):2230–2245, 2020.

[104] Messi, Z., et al. *Traction Forces Control Cell-Edge Dynamics and Mediate Distance Sensitivity during Cell Polarization.* Current Biology, 30(9):1762–1769.e5, 2020.

[105] Polio, S. R., et al. *A micropatterning and image processing approach to simplify measurement of cellular traction forces.* Acta Biomaterialia, 8(1):82–88, 2012.

[106] Legant, W. R., et al. *Multidimensional traction force microscopy reveals out-of-plane rotational moments about focal adhesions.* Proceedings of the National Academy of Sciences of the United States of America, 110(3):881–886, 2013.

[107] Dembo, M. and Wang, Y. L. *Stresses at the cell-to-substrate interface during locomotion of fibroblasts.* Biophysical Journal, 76(4):2307–2316, 1999.

[108] Franck, C., et al. *Three-dimensional traction force microscopy: A new tool for quantifying cell-matrix interactions.* PLoS ONE, 6(3):17833, 2011.

[109] Kudla, J., et al. *Advances and current challenges in calcium signaling*, 2018.

[110] Kyratsous, N. I., et al. *Visualizing context-dependent calcium signaling in encephalitogenic T cells in vivo by two-photon microscopy.* Proceedings of the National Academy of Sciences of the United States of America, 114(31):E6381–E6389, 2017.

[111] Friedmann, K. S., et al. *Calcium signal dynamics in T lymphocytes: Comparing in vivo and in vitro measurements*, 2019.

[112] Vines, A., et al. *A flow-cytometric method for continuous measurement of intracellular Ca2+ concentration.* Cytometry Part A, 77A(11):1091–1097, 2010.

[113] Burchiel, S. W., et al. *Analysis of free intracellular calcium by flow cytometry: Multiparameter and pharmacologic applications.* Methods, 21(3):221–230, 2000.

[114] Han, Y., et al. *Review: Imaging technologies for flow cytometry*, 2016.

[115] Walsh, A. J., et al. *Classification of T-cell activation via autofluorescence lifetime imaging*. Nature Biomedical Engineering, 5(1):77–88, 2021.

[116] Bird, G. S., et al. *Methods for studying store-operated calcium entry*. Methods, 46(3):204–212, 2008.

[117] Grynkiewicz G, Poenie M, T. R. *A new generation of Ca2+ indicators with greatly improved fluorescence properties*. J Biol Chem, 260:3440–50, 1985.

[118] Le Borgne, M., et al. *Real-Time Analysis of Calcium Signals during the Early Phase of T Cell Activation Using a Genetically Encoded Calcium Biosensor*. The Journal of Immunology, 196(4):1471–1479, 2016.

[119] Mues, M., et al. *Real-time in vivo analysis of T cell activation in the central nervous system using a genetically encoded calcium indicator*. Nature Medicine, 19(6):778–783, 2013.

[120] Thestrup, T., et al. *Optimized ratiometric calcium sensors for functional in vivo imaging of neurons and T lymphocytes*. Nature Methods, 11(2):175–182, 2014.

[121] Fritzsche, M., et al. *CalQuo: Automated, simultaneous single-cell and population-level quantification of global intracellular Ca2+ responses*. Scientific Reports, 5(1):16487, 2015.

[122] Cossarizza, A., et al. *Guidelines for the use of flow cytometry and cell sorting in immunological studies*. European Journal of Immunology, 47(10):1584–1797, 2017.

[123] Delmonte, O. M., et al. *Methods of allergy and immunology Flow cytometry: Surface markers and beyond*. Journal of Allergy and Clinical Immunology, 143:528–537, 2019.

[124] O'Donnell, E. A., et al. *Multiparameter Flow Cytometry: Advances in High Resolution Analysis*. Immune Network, 13(2):43, 2013.

[125] Colin-York, H., et al. *Spatiotemporally Super-Resolved Volumetric Traction Force Microscopy*. Nano Letters, 19(7):4427–4434, 2019.

[126] Dalmo, R. A. *Atlantic salmon (Salmo salar L.) epidermal Malpighian cells-motile cells clearing away latex beads in vitro*. Technical report, 1998.

[127] Aleksic, M., et al. *Dependence of T Cell Antigen Recognition on T Cell Receptor-Peptide MHC Confinement Time*. Immunity, 32(2):163–174, 2010.

[128] Chen, Y. T., et al. *A testicular antigen aberrantly expressed in human cancers detected by autologous antibody screening*. Proceedings of the National Academy of Sciences of the United States of America, 94(5):1914–1918, 1997.

[129] Esfandiary, A. and Ghafouri-Fard, S. *New York esophageal squamous cell carcinoma-1 and cancer immunotherapy*, 2015.

[130] Chen, J. L., et al. *Structural and kinetic basis for heightened immunogenicity of T cell vaccines.* Journal of Experimental Medicine, 201(8):1243–1255, 2005.

[131] Bethune, M. T., et al. *Isolation and characterization of NY-ESO-1-specific T cell receptors restricted on various MHC molecules.* Proceedings of the National Academy of Sciences of the United States of America, 115(45):E10702–E10711, 2018.

[132] Li, D., et al. *Extended-resolution structured illumination imaging of endocytic and cytoskeletal dynamics.* Science, 349(6251), 2015.

[133] Gustafsson, M. G., et al. *Three-dimensional resolution doubling in wide-field fluorescence microscopy by structured illumination.* Biophysical Journal, 94(12):4957–4970, 2008.

[134] Li, D., et al. *Astigmatic traction force microscopy (aTFM).* Nature Communications, 12(1):2168, 2021.

[135] Gutierrez, E., et al. *High refractive index silicone gels for simultaneous total internal reflection fluorescence and traction force microscopy of adherent cells*, 2011.

[136] Shnayderman, A., et al. *An SVD-based grayscale image quality measure for local and global assessment.* IEEE Transactions on Image Processing, 15(2):422–429, 2006.

[137] Li, Y., et al. *Real-time 3D single-molecule localization using experimental point spread functions.* Nature Methods, 15(5):367–369, 2018.

[138] Allan, D., et al. *soft-matter/trackpy: Trackpy v0.4.2*, 2019.

[139] Hunter, J. D. *Matplotlib: A 2D graphics environment.* Computing in Science and Engineering, 9(3):90–95, 2007.

[140] Crocker, J. C. and Grier, D. G. *Methods of digital video microscopy for colloidal studies.* Journal of Colloid and Interface Science, 179(1):298–310, 1996.

[141] LeCun, Y., et al. *Gradient-based learning applied to document recognition.* Proceedings of the IEEE, 86(11):2278–2323, 1998.

[142] Lecun, Y., et al. *Deep learning.* Nature, 521(7553):436–444, 2015.

[143] Schindelin, J., et al. *Fiji: An open-source platform for biological-image analysis*, 2012.

[144] Van Der Walt, S., et al. *Scikit-image: Image processing in python.* PeerJ, 2014(1):e453, 2014.

[145] Kingma, D. P. and Ba, J. L. *Adam: A method for stochastic optimization.* In *3rd International Conference on Learning Representations, ICLR 2015 - Conference Track Proceedings.* International Conference on Learning Representations, ICLR, 2015.

[146] Kjer-Nielsen, L., et al. *Crystal structure of the human T cell receptor CD3$\epsilon\gamma$ heterodimer complexed to the therapeutic mAb OKT3.* Proceedings of the National Academy of Sciences of the United States of America, 101(20):7675–7680, 2004.

[147] Virtanen, P., et al. *SciPy 1.0: fundamental algorithms for scientific computing in Python.* Nature Methods, 17(3):261–272, 2020.

[148] Harris, A. K., et al. *Silicone rubber substrata: A new wrinkle in the study of cell locomotion.* Science, 208(4440):177–179, 1980.

[149] Sabass, B., et al. *High resolution traction force microscopy based on experimental and computational advances.* Biophysical Journal, 94(1):207–220, 2008.

[150] Roca-Cusachs, P., et al. *Quantifying forces in cell biology.* Nature Cell Biology, 19(7):742–751, 2017.

[151] Colin-York, H., et al. *Dissection of mechanical force in living cells by super-resolved traction force microscopy.* Nature Protocols, 12(4):783–796, 2017.

[152] Oakes, P. W., et al. *Tension is required but not sufficient for focal adhesion maturation without a stress fiber template.* Journal of Cell Biology, 196(3):363–374, 2012.

[153] Discher, D. E., et al. *Tissue cells feel and respond to the stiffness of their substrate*, 2005.

[154] Flanagan, L. A., et al. *Neurite branching on deformable substrates.* Neuroreport, 13(18):2411, 2002.

[155] Schwarz, U. S. and Soiné, J. R. *Traction force microscopy on soft elastic substrates: A guide to recent computational advances*, 2015.

[156] Kandow, C. E., et al. *Polyacrylamide Hydrogels for Cell Mechanics: Steps Toward Optimization and Alternative Uses*, 2007.

[157] Ferrari, A. *Recent technological advancements in traction force microscopy*, 2019.

[158] Bergert, M., et al. *Confocal reference free traction force microscopy.* Nature Communications, 7(1):1–10, 2016.

[159] Banda, O. A., et al. *Reference-Free Traction Force Microscopy Platform Fabricated via Two-Photon Laser Scanning Lithography Enables Facile Measurement of Cell-Generated Forces.* ACS Applied Materials and Interfaces, 11(20):18233–18241, 2019.

[160] Plotnikov, S. V., et al. *High-Resolution Traction Force Microscopy.* In *Methods in Cell Biology*, volume 123, pages 367–394. Academic Press Inc., 2014.

[161] Butler, J. P., et al. *Traction fields, moments, and strain energy that cells exert on their surroundings.* AJP: Cell Physiology, 282(3):C595–C605, 2002.

[162] Lifshitz, L. D. L. L. P. P. A. M. K. E. *Theory of Elasticity - 3rd Edition.* Elsevier, 1986.

[163] Heinz Engl, Martin Hanke, A. N. *Regularization of inverse problems.* Springer, 1996.

[164] Schwarz, U. S., et al. *Calculation of forces at focal adhesions from elastic substrate data: The effect of localized force and the need for regularization.* Biophysical Journal, 83(3):1380–1394, 2002.

[165] Sune-Aunon, A., et al. *L1-regularized reconstruction for traction force microscopy.* In *Proceedings - International Symposium on Biomedical Imaging*, volume 2016-June, pages 140–144. IEEE Computer Society, 2016.

[166] Han, S. J., et al. *Traction microscopy to identify force modulation in subresolution adhesions.* Nature Methods, 12(7):653–656, 2015.

[167] Hansen, P. C. *The L-curve and its use in the numerical treatment of inverse problems*, 2000.

[168] Raffel, M., et al. *Particle Image Velocimetry A Practical Guide.* Springer, 1998.

[169] Martiel, J. L., et al. *Measurement of cell traction forces with ImageJ.* Methods in Cell Biology, 125:269–287, 2015.

[170] Chang, N. M. and Kuang-An. *Introduction to MPIV*, 2003.

[171] Hiroyasu, S., et al. *A hemidesmosomal protein regulates actin dynamics and traction forces in motile keratinocytes.* The FASEB Journal, 30(6):2298–2310, 2016.

[172] Panagiotakopoulou, M., et al. *Cell cycle–dependent force transmission in cancer cells.* Molecular Biology of the Cell, 29(21):2528–2539, 2018.

[173] Korobchevskaya, K., et al. *Exploring the Potential of Airyscan Microscopy for Live Cell Imaging.* Photonics, 4(3):41, 2017.

[174] Lothar Schermelleh, Alexia Ferrand, Thomas Huser, Christian Eggeling, Markus Sauer, O. B. &. G. P. C. D. *Super-resolution microscopy demystified.* Nature Cell Biology, 21:72–84, 2019.

[175] Schermelleh, L., et al. *A guide to super-resolution fluorescence microscopy.* Journal of Cell Biology, 190(2):165–175, 2010.

[176] Basu, R., et al. *Cytotoxic T Cells Use Mechanical Force to Potentiate Target Cell Killing.* Cell, 165(1):100–110, 2016.

[177] Lene Rydal Sveen, Gerrit Timmerhaus, Aleksei Krasnov, Harald Takle, S. H. &. E. Y. *Wound healing in post-smolt Atlantic salmon (Salmo salar L.).* Scientific Reports, pages 1–16, 2019.

[178] Chika Okimura, Atsushi Taniguchi, S. N. &. Y. I. *Rotation of stress fibers as a single wheel in migrating fish keratocytes.* Scientific Reports, pages 1–10, 2018.

[179] Paszek, M. J., et al. *Integrin clustering is driven by mechanical resistance from the glycocalyx and the substrate.* PLoS Computational Biology, 5(12), 2009.

[180] Barbieri, L., et al. *Two-dimensional TIRF-SIM–traction force microscopy (2D TIRF-SIM-TFM).* Nature Communications, 12(1):2169, 2021.

[181] Axelrod, D. *Cell-substrate contacts illuminated by total internal reflection fluorescence.* Journal of Cell Biology, 89(1):141–145, 1981.

[182] Ambrose, E. J. *A surface contact microscope for the study of cell movements [32]*, 1956.

[183] Gustafsson, M. G. L. *Nonlinear structured-illumination microscopy: Wide-field fluorescence imaging with theoretically unlimited resolution.* Proceedings of the National Academy of Sciences, 102(37):13081–13086, 2005.

[184] Liu, K., et al. *Improved-Throughput Traction Microscopy Based on Fluorescence Micropattern for Manual Microscopy.* PLoS ONE, 8(8):e70122, 2013.

[185] Jurado, C., et al. *Slipping or gripping? Fluorescent speckle microscopy in fish keratocytes reveals two different mechanisms for generating a retrograde flow of actin.* Molecular Biology of the Cell, 16(2):507–518, 2005.

[186] Plotnikov, S. V., et al. *Force fluctuations within focal adhesions mediate ECM-rigidity sensing to guide directed cell migration.* Cell, 151(7):1513–1527, 2012.

[187] Huang, B., et al. *Three-dimensional super-resolution imaging by stochastic optical reconstruction microscopy.* Science, 319(5864):810–813, 2008.

[188] King Lam Hui, Lakshmi Balagopalan, Lawrence E. Samelson and Upadhyaya, A. *Cytoskeletal forces during signaling activation in Jurkat T-cells.* Molecular Biology of the Cell, 26, 2015.

[189] Aramesh, M., et al. *Functionalized Bead Assay to Measure Three-dimensional Traction Forces during T-cell Activation.* Nano Letters, 2020.

[190] Colin-York, H., et al. *Cytoskeletal actin patterns shape mast cell activation.* Communications Biology, 2(1):1–12, 2019.

[191] Pavani, S. R. P., et al. *Three-dimensional, single-molecule fluorescence imaging beyond the diffraction limit by using a double-helix point spread function.* Proceedings of the National Academy of Sciences of the United States of America, 106(9):2995–2999, 2009.

[192] Juette, M. F., et al. *Three-dimensional sub-100 nm resolution fluorescence microscopy of thick samples.* Nature Methods, 5(6):527–529, 2008.

[193] Purohit, A., et al. *Spatio-temporal correlation super-resolution optical fluctuation imaging.* EPL, 125(2):20005, 2019.

[194] Maier, A., et al. *A gentle introduction to deep learning in medical image processing*, 2019.

[195] Subasi, A. *Machine learning techniques.* In *Practical Machine Learning for Data Analysis Using Python*, pages 91–202. Elsevier, 2020.

[196] Manz, B. N., et al. *T-cell triggering thresholds are modulated by the number of antigen within individual T-cell receptor clusters.* Proceedings of the National Academy of Sciences of the United States of America, 108(22):9089–9094, 2011.

[197] Clapham, D. E. *Calcium Signaling*, 2007.

[198] Colin-York, H., et al. *Distinct actin cytoskeleton behaviour in primary and immortalised T-cells.* Journal of cell science, 133(5), 2019.

[199] Kaech, S. M., et al. *Effector and memory T-cell differentiation: Implications for vaccine development*, 2002.

[200] Grakoui, A., et al. *The immunological synapse: A molecular machine controlling T cell activation.* Science, 285(5425):221–227, 1999.

[201] Oh-hora, M. and Rao, A. *Calcium signaling in lymphocytes*, 2008.

[202] Boulware, M. J. and Marchant, J. S. *Timing in Cellular Ca2+ Signaling*, 2008.

[203] Thomas, A. P., et al. *Spatial and temporal aspects of cellular calcium signaling.* The FASEB Journal, 10(13):1505–1517, 1996.

[204] Oh-hora, M., et al. *Dual functions for the endoplasmic reticulum calcium sensors STIM1 and STIM2 in T cell activation and tolerance.* Nature Immunology, 9(4):432–443, 2008.

[205] Malek, T. R. and Castro, I. *Interleukin-2 Receptor Signaling: At the Interface between Tolerance and Immunity*, 2010.

[206] Follain, G., et al. *Seeing is believing - multi-scale spatio-temporal imaging towards in vivo cell biology*, 2017.

[207] Kummrow, A., et al. *Quantitative assessment of cell viability based on flow cytometry and microscopy.* Cytometry Part A, 83 A(2):197–204, 2013.

[208] Xia, F., et al. *TCR and CD28 Concomitant Stimulation Elicits a Distinctive Calcium Response in Naive T Cells.* Frontiers in Immunology, 9:2864, 2018.

[209] Fiolka, R. *Resolution upgrades for light-sheet microscopy*, 2019.

[210] Power, R. M. and Huisken, J. *A guide to light-sheet fluorescence microscopy for multiscale imaging*, 2017.

[211] Gao, L. *Extend the field of view of selective plan illumination microscopy by tiling the excitation light sheet.* Optics Express, 23(5):6102, 2015.

[212] Driscoll, M. K., et al. *Robust and automated detection of subcellular morphological motifs in 3D microscopy images.* Nature Methods, 16(10):1037–1044, 2019.

[213] Voleti, V., et al. *Real-time volumetric microscopy of in vivo dynamics and large-scale samples with SCAPE 2.0.* Nature Methods, 16(10):1054–1062, 2019.

[214] Diekmann, R., et al. *Chip-based wide field-of-view nanoscopy.* Nature Photonics, 11(5):322–328, 2017.

[215] Coucheron, D. A., et al. *Chip-based nanoscopy: towards integration and high-throughput imaging.* In Verma, P. and Egner, A., editors, *Nanoimaging and Nanospectroscopy V*, volume 10350, page 31. SPIE, 2017.

[216] Dustin, M. L. *T-cell activation through immunological synapses and kinapses*, 2008.

[217] Liu, Y., et al. *Stripe artifact reduction for digital scanned structured illumination light sheet microscopy.* Optics Letters, 44(10):2510, 2019.

[218] Liang, X., et al. *Stripe artifact elimination based on nonsubsampled contourlet transform for light sheet fluorescence microscopy.* Journal of Biomedical Optics, 21(10):106005, 2016.

[219] Taylor, M. A., et al. *Diffuse light-sheet microscopy for stripe-free calcium imaging of neural populations.* Journal of Biophotonics, 11(12), 2018.

[220] Korobchevskaya, K., et al. *Extended mechanical force measurements using structured illumination microscopy.* Philosophical Transactions of the Royal Society A: Mathematical, Physical and Engineering Sciences, 379(2199):rsta.2020.0151, 2021.

[221] Yuan, D. J., et al. *Biphasic response of T cell activation to substrate stiffness.* Biomaterials, 273:120797, 2021.

[222] Wahl, A., et al. *Biphasic mechanosensitivity of T cell receptor-mediated spreading of lymphocytes.* Proceedings of the National Academy of Sciences of the United States of America, 116(13):5908–5913, 2019.

[223] Chakraborty, M., et al. *Mechanical Stiffness Controls Dendritic Cell Metabolism and Function.* Cell Reports, 34(2):108609, 2021.

[224] Cox, T. R. and Erler, J. T. *Remodeling and homeostasis of the extracellular matrix: Implications for fibrotic diseases and cancer*, 2011.

[225] Pageon, S. V., et al. *Mechanoimmunology: Molecular-scale forces govern immune cell functions*, 2018.

[226] Swartz, M. A. and Lund, A. W. *Lymphatic and interstitial flow in the tumour microenvironment: Linking mechanobiology with immunity*, 2012.

[227] Lippert, A., et al. *Robust T-cell signaling triggered on soft polydimethylsiloxane-supported lipid-bilayers.* bioRxiv, page 2020.06.05.134684, 2020.

[228] Monnot, G. C., et al. *miR-155 Overexpression in OT-1 CD8+ T Cells Improves Anti-Tumor Activity against Low-Affinity Tumor Antigen.* Molecular Therapy - Oncolytics, 16:111–123, 2020.

[229] Martínez-Usatorre, A., et al. *PD-1 Blockade Unleashes Effector Potential of Both High- and Low-Affinity Tumor-Infiltrating T Cells.* The Journal of Immunology, 201(2):792–803, 2018.

[230] Corridoni, D., et al. *NOD2 and TLR2 Signal via TBK1 and PI31 to Direct Cross-Presentation and CD8 T Cell Responses.* Frontiers in Immunology, 10(APR):958, 2019.

[231] Johnson, L. A., et al. *Dendritic cells enter lymph vessels by hyaluronan-mediated docking to the endothelial receptor LYVE-1.* Nature Immunology, 18(7):762–770, 2017.

[232] Castellino, F., et al. *Chemokines enhance immunity by guiding naive CD8+ T cells to sites of CD4+ T cell-dendritic cell interaction.* Nature, 440(7086):890–895, 2006.

[233] Schaefer, B. C., et al. *Observation of antigen-dependent CD8+ T-cell/dendritic cell interactions in vivo.* Cellular Immunology, 214(2):110–122, 2001.

[234] Stoll, S., et al. *Dynamic imaging of T cell-dendritic cell interactions in lymph nodes.* Science, 296(5574):1873–1876, 2002.

[235] Montes, M., et al. *Calcium responses elicited in human T cells and dendritic cells by cell–cell interaction and soluble ligands.* International Immunology, 11(4):561–568, 1999.

[236] Kiskowski, M. A., et al. *On the use of Ripley's K-function and its derivatives to analyze domain size.* Biophysical Journal, 97(4):1095–1103, 2009.

[237] Hansson, K., et al. *RipleyGUI: software for analyzing spatial patterns in 3D cell distributions.* Frontiers in Neuroinformatics, 7:5, 2013.

[238] Cahalan, M. D., et al. *Two-photon tissue imaging: Seeing the immune system in a fresh light*, 2002.

[239] Vickovic, S., et al. *Three-dimensional spatial transcriptomics uncovers cell type dynamics in the rheumatoid arthritis synovium*, 2020.

[240] Hunter, M. V., et al. *Spastial transcriptomics reveals the architecture of the tumor/microenvironment interface*, 2020.

[241] Liu, T. L., et al. *Observing the cell in its native state: Imaging subcellular dynamics in multicellular organisms.* Science, 360(6386):1392, 2018.

[242] Nelsen, E., et al. *Combined Atomic Force Microscope and Volumetric Light Sheet System for Correlative Force and Fluorescence Mechanobiology Studies.* Scientific Reports, 10(1):1–12, 2020.

[243] Moreno-Flores, S. *Hallmarks of Life in Single Cell Contact Mechanics: Outstanding Challenges and Perspectives.* Frontiers in Mechanical Engineering, 6:58, 2020.